Development of 13.5-meter-tall Vibration Isolation　System for the Main Mirrors in KAGRA

奥富　弘基

博士（理学）

総合研究大学院大学

物理科学研究科

天文科学専攻

平成３０（２０１８）年度

Development of 13.5-meter-tall Vibration Isolation System for the Main Mirrors in KAGRA

Koki Okutomi

June 19, 2019

Abstract

The direct detection of gravitational waves by Advanced Laser Interferometer Gravitational wave Observatory (LIGO) has triggered the birth of a new window in astronomy. The number of events detected with sufficient confidence amounts to ten for binary black hole mergers and one for a binary neutron star merger. As for the binary neutron star merger GW170817, starting with the early alert of gravitational wave detection by LIGO and Virgo, follow-up observations of the source with multiband electromagnetic telescopes were performed, and they yielded novel information about astrophysics and cosmology. Now, we are quite sure that gravitational wave observations will play an important role in revealing a hidden side of the universe in the future.

KAGRA is a 3-km interferometric gravitational wave telescope that was constructed in Japan. The KAGRA interferometer has two features that distinguish it from the current 2nd-generation advanced detectors: it is located at an underground site with lower seismic disturbance and it uses cryogenic sapphire mirrors in order to reduce thermal noise. As the KAGRA is located far from both LIGO and Virgo, the participation of KAGRA in the global observatory network can offer benefits of not only accurate false positive rejection but also better source localization, better sky coverage, and more precise parameter estimation. Presently, KAGRA is in the process of completing full configuration of the interferometer toward the joint observation with the LIGO and Virgo detectors scheduled in 2019.

Vibration isolation systems are the main instruments for suppressing mirror fluctuations introduced by continuous and random seismic motion. Even in a quiet underground environment, as gravitational wave observation with the KAGRA interferometer requires spectral displacement fluctuation of the mirror to be less than $10^{-19}\,\mathrm{m/Hz^{1/2}}$ in its observational band above 10 Hz, one needs to attenuate the vibration transmission from the ground to the mirror by 8–10 orders of magnitude. This level of seismic attenuation can be achieved by suspending the mirror at the bottom of a multi-stage pendulum called a suspension system, which provides vibration filtering at high frequencies above its mechanical resonances. The suspension system also serves as an interface of the interferometer control. The position and attitude of the mirror can be monitored and controlled with local sensors and actuators mounted on the suspension stages so that the optical cavities in the interferometer are kept in the resonant condition. Although the suspension system will enhance the amplitude of the mirror fluctua-

tion at the mechanical resonant frequencies outside of the observation band ($< 1\,\mathrm{Hz}$), it can also be suppressed by active feedback control with the electric instruments.

The study in this thesis develops a vibration isolation system called type-A suspension for the main mirrors (test masses) in KAGRA. The Type-A suspension is a large pendulum with a total of nine stages and is 13.5-meter tall. It consists of two primary compositions, i.e., the tower part representing the top five stages at room temperatures and the cryogenic payload representing the bottom four stages at cryogenic temperatures ($\sim 20\,\mathrm{K}$). This study focuses on the tower part as the vibration isolation performance of the entire suspension system is determined by the installation and adjustments of the low-frequency oscillators such as inverted pendulums and geometric anti-springs (GASs) implemented at the top five stages.

The performance tests demonstrate that the installed type-A tower system basically has dynamic characteristics that satisfy the requirements. The frequency responses of the type-A tower are measured and compared to the predictions of the nominal model. Although there is some amount of deviation, the obtained frequency responses can be regarded as acceptable for achieving the required vibration isolation performances except for the vertical direction. As for the vertical direction, the dynamics of the type-A tower shows discrepancies between the measurement results and the model predictions, particularly the mode shapes of its higher order resonances. It is suspected that the higher order oscillatory behavior has a stronger dependence on the divergence of the mechanical parameters from the nominal values. However, as the higher order modes have a smaller impact on the root mean square (RMS) residual motion and that the measured mode frequencies are roughly distributed as expected, the discrepancies in the vertical mode dynamics seem to be within the permissible range. This tolerance is also plausible from the measured displacement spectrum at the dummy payload, which is suspended, instead of the actual cryogenic payload. One problem still remains: is the effect of couplings from non-straightforwardly-controllable degrees of freedom such as a tilt of the middle GAS filter stages. The impact of the couplings on the test mass or the interferometer should be confirmed after integration with the cryogenic payload.

In two kinds of damping control implemented in performance tests, torsion mode damping is first engaged at the bottom stage of the type-A tower. As a major fraction of the height of the type-A suspension is accounted for a series of single suspension wires, the system behaves like a torsion pendulum with extremely low stiffness and torsional modes with long durations, which creates challenges in stabilizing the alignment of the mirror. The type-A tower address this issue by providing a function of active damping control at the tower's bottom stage. The torsion mode damping test proves that the long exponential decay time of the resonances can be successfully reduced to less than 1 min by the active feedback control. In addition, the in-loop sensor indicates that the RMS residual angular fluctuation in torsion is suppressed sufficiently to a level of acquiring an arm cavity lock. Therefore, it is concluded that the

type-A tower has satisfactory torsion mode damping.

This study also presents an advanced control scheme called modal damping. Modal damping processes feedback signals in a decoupled modal basis instead of a conventional Cartesian basis, allowing us to simplify the servo design optimization and to access efficient actuation for a coupled oscillatory system. The control test demonstrates feasibility of modal damping for the coupled vertical modes of the type-A suspension. By deriving a conversion law between the Cartesian basis and the modal basis from the mathematical model, coupled signals of the vertical modes can be decomposed intothose of each orthogonal eigenmode. Moreover, the modal damping results show that the eigenmodes can be damped independently of other modes. Although the availability of modal controllers is validated only for the vertical modes in this test, one can expect to apply this technique to other stages having less-powerful actuators such as the cryogenic payload.

After the sequence of tower tests, the installed type-A tower was integrated with the cryogenic payload and incorporated into the global system of the KAGRA interferometer. This thesis includes measurement of the vibration isolation ratio from the ground to the test mass. During the first cryogenic test operation of the simplified 3-km Michelson interferometer, we measured the vibration transmissivity from the top stage to the error signals of the inteferometer output. By combining the measured result with a model prediction of the transmissibity from the ground to the top stage derived from the tuned mathematical model, the total vibration isolation ratio of the type-A suspension was estimated as 9×10^{-22} for the pure longitudinal contribution at 10 Hz. Although the estimated result and nominal model prediction have mismatches, the seismic attenuation performance of the real system seems to be reasonable enough to achieve the design sensitivity of KAGRA.

Acknowledgement（謝辞）

Contents

Chapter 1

Introduction

1.1 Nature of gravitational waves

1.1.1 Derivation in linearized general relativity

The concept of gravitational wave first appeared in Einstein's letter as an wave solution of the linearized equation of the gravitational field [1, 2]. In other words, gravitational waves are a variation of spacetime whose structure is determined as a metric tensor $g_{\mu\nu}$. The structure of spacetime is expressed as the world interval $\mathrm{d}s$ between two neighboring points via the following equation:

$$\mathrm{d}s^2 = g_{\mu\nu}\,\mathrm{d}x^\mu\mathrm{d}x^\nu\,. \tag{1.1}$$

The symbols with Greek index $\mathrm{d}x^\mu$ ($\mu = 0,\ 1,\ 2,\ 3$) denote the difference between two separated points in a four-dimensional coordinate system $(x^0,\ x^1,\ x^2,\ x^3) \equiv (ct,\ x,\ y,\ z)$ [1]. A flat spacetime without any gravity is called a Minkowski spacetime. Its structure is described with the metric $\eta = \mathrm{diag}(-1,\ 1,\ 1,\ 1)$.

The existence of mass or energy forms curved structure in the spacetime. The Einstein equation associates the curved spacetime with the distribution of the mass and energy,

$$R_{\mu\nu} - \frac{1}{2}g_{\mu\nu}R = \frac{8\pi G}{c^4}T_{\mu\nu}\,. \tag{1.2}$$

Here, $R_{\mu\nu}$ and R on the left hand side are respectively the Ricci tensor and the Ricci scalar, which are associated with the curvature of spacetime through the Riemann tensor $R^\lambda_{\mu\rho\nu}$ as

---

[1] On the other hand, the symbols with Roman indices such as $\mathrm{d}x^i$ denote the difference between the spacial components $i = 1,\ 2,\ 3$ of two points.

follows[2].

$$R^{\lambda}_{\mu\rho\nu} = \partial_{\rho}\Gamma^{\lambda}_{\mu\nu} - \partial_{\nu}\Gamma^{\lambda}_{\mu\rho} + \Gamma^{\lambda}_{\alpha\rho}\Gamma^{\alpha}_{\mu\nu} - \Gamma^{\lambda}_{\alpha\nu}\Gamma^{\alpha}_{\mu\rho} \tag{1.3}$$

$$R_{\mu\nu} \equiv R^{\alpha}_{\mu\alpha\nu} \tag{1.4}$$

$$R \equiv R_{\mu\mu} \tag{1.5}$$

On the right hand side of eq. (1.2), $T_{\mu\nu}$ is the energy-momentum tensor, G is Newton's gravitational constant, and c is the speed of light. Therefore, Einstein equation indicates that the mass-energy distribution on the right hand side creates the curvature of spacetime described on the left hand side in 1.2.

The derivation of the gravitational wave is achieved in the weak-field approximation where tiny perturbation exists in the flat spacetime. In terms of the metric, it can be expressed as the sum of the linear perturbation $h_{\mu\nu}$ and the Minkowski metric,

$$g_{\mu\nu} = \eta_{\mu\nu} + h_{\mu\nu}\,. \tag{1.6}$$

Imposing conditions of a vacuum, $T_{\mu\nu} = 0$, and the Lorentz gauge,

$$\frac{\partial h^{\mu}_{\nu}}{\partial x_{\mu}} = 0\,, \tag{1.7}$$

and disregarding the higher order terms $\mathcal{O}(h^2_{\mu\nu})$, substitution of eq. (1.6) into the Einstein equation eq. (1.2) yields a wave equation

$$\left(-\frac{1}{c^2}\frac{\partial^2}{\partial t^2} + \frac{\partial^2}{\partial x_i^2}\right)h_{\mu\nu} = 0\,. \tag{1.8}$$

This equation indicates that the perturbation $h_{\mu\nu}$ propagates through the spacetime at the speed of light as a wave.

When we choose a spatial coordinate such that a gravitational wave travels along the z- or x^3-direciton, the plain wave solution can be derived as the following expression:

$$h_{\mu\nu} = A_{\mu\nu}\exp\left[i\omega\left(t - \frac{z}{c}\right)\right]$$

$$A_{\mu\nu} = \begin{pmatrix} 0 & 0 & 0 & 0 \\ 0 & h_+ & h_\times & 0 \\ 0 & h_\times & -h_+ & 0 \\ 0 & 0 & 0 & 0 \end{pmatrix} \tag{1.9}$$

Here ω is the angular frequency, h_+ and $h_\times$ are the independent constants denoting the amplitude of the gravitational wave. This reveals the transverse and polarized natures of gravitational waves. The two polarizations known as the plus mode and the cross mode are symmetric through a 45-degree rotation, as shown in fig. 1.1.

---

[2] Following Einstein's summation convention, we shall take the summation of all the degrees of freedom about the Greek indices that appear both in superscripts and subscripts.
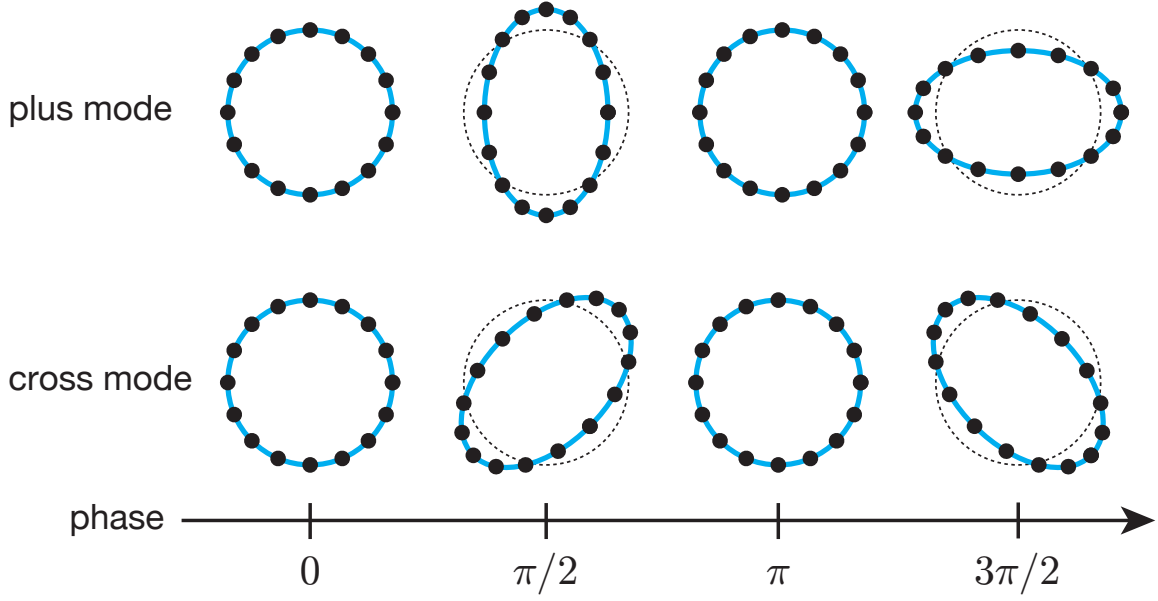
Fig. 1.1. Two polarizations of gravitational waves; +-mode and ×-mode. Each mode produces different deformation shapes in the free-falling point masses with circular configuration.

1.1.2 Observable effect of gravitational waves

Consider the situation whereby two free-falling point masses are positioned separately along the x- or x^1-axis with a distance of ϵ. The effect of gravitational waves passing along the z-axis (described in eq. (1.9)) appears when writing the proper distance of the particles. If the particles are initially at rest, the proper distance δl is written as,

$$\delta l \equiv \int |\mathrm{d}s^2|^{1/2} = \int |g_{\mu\nu}\mathrm{d}x^\mu r dx^\nu|^{1/2}$$
$$= \int_0^\epsilon |g_{11}|^{1/2}\,\mathrm{d}x^1$$
$$\simeq |g_{11}|^{1/2} \simeq \left(1 + \frac{1}{2}h_{11}\right)\epsilon\,. \tag{1.10}$$

From eq. (1.10), it turns out that gravitational waves change the proper distance of the free-falling masses. This is a physical quantity observable for our laser interferometric telescopes. The absolute change in distance is proportional to both the initial separation ϵ and the amplitude h_{11}.

There are two polarizations in gravitational waves as shown in eq. (1.9). To understand interaction of the two modes with masses, consider a thought experiment in which the test masses are placed in a circular configuration at $x^i = (\epsilon\cos\theta, \epsilon\sin\theta, 0)$. The proper distance

of the masses under the influence of gravitational waves is described as

$$\begin{pmatrix} \delta l^x \\ \delta l^y \end{pmatrix} = \begin{pmatrix} \epsilon^x \\ \epsilon^y \end{pmatrix} + \frac{1}{2} e^{i\omega(t-z/c)} \begin{pmatrix} h_+ & h_\times \\ h_\times & -h_+ \end{pmatrix} \begin{pmatrix} \epsilon^x \\ \epsilon^y \end{pmatrix} \tag{1.11}$$

$$= \begin{pmatrix} \epsilon^x \\ \epsilon^y \end{pmatrix} + \frac{1}{2} e^{i\omega(t-z/c)} \begin{pmatrix} \epsilon^x \\ -\epsilon^y \end{pmatrix} h_+ + \frac{1}{2} e^{i\omega(t-z/c)} \begin{pmatrix} \epsilon^x \\ \epsilon^y \end{pmatrix} h_\times \,. \tag{1.12}$$

The second term indicates the variation in the proper distance caused by the plus mode, while the third term indicates that by the cross mode. Figure 1.1 illustrates the interaction of the two modes of the gravitational waves with the free-falling masses. The plus mode distorts the circular arrangement into a "plus" shape, while the cross mode distorts it into a "cross" shape. As mentioned above, the plus mode and the cross mode have symmetry through a 45-degree rotation.

1.1.3   Gravitational wave radiation

A gravitatonal wave is generated by accelerated masses analogous to the radiation of electro-magnetic waves that are induced by acceleration of charged particles. However, the gravitational wave radiation requires quadrupole (or higher-order multipole) moments rather than a dipole moment, which is electromagnetic radiation requires.

Starting from the wave equation eq. (1.8) in the presence of the energy-momentum tensor on the right-hand side,

$$\left(-\frac{1}{c^2} \frac{\partial^2}{\partial t^2} + \frac{\partial^2}{\partial x_i^2} \right) h_{\mu\nu} = -\frac{16\pi G}{c^4} T_{\mu\nu} \,. \tag{1.13}$$

By introducing the retarded Green's function $G(\boldsymbol{x} - \boldsymbol{x}')$ written as

$$G(\boldsymbol{x} - \boldsymbol{x}') = \frac{1}{4\pi |\boldsymbol{x} - \boldsymbol{x}'|} \delta(x^0_{\text{ret}} - x'^0) \,, \tag{1.14}$$

$$x^0_{\text{ret}} \equiv ct_{\text{ret}} \,, \quad t_{\text{ret}} = t - \frac{|\boldsymbol{x} - \boldsymbol{x}'|}{c} \,,$$

just as in electromagnetism, one can obtain a solution of eq. (1.13) in the form of the retarded potential

$$h_{\mu\nu}(x^0, \boldsymbol{x}) = \frac{4G}{c^4} \int \frac{T_{\mu\nu}\left(x^0 - \frac{|\boldsymbol{x}-\boldsymbol{x}'|}{c}, \boldsymbol{x}'\right)}{|\boldsymbol{x} - \boldsymbol{x}'|} d\boldsymbol{x}' \,. \tag{1.15}$$

If we suppose that the region of $T_{\mu\nu} \neq 0$ is small enough and the observer is far from the source, eq. (1.15) can be approximated to the lowest-order terms of the mass multipole expansion as

$$h_{ij}(t, \boldsymbol{x}) = \frac{1}{r} \frac{2G}{c^4} \ddot{Q}_{ij}(t') \,, \tag{1.16}$$

where $r \equiv |\boldsymbol{x} - \boldsymbol{x}'|$, $t' \equiv t - r/c$ and Q_{ij} is the mass quadropole moment determined as

$$Q_{ij}(t') = \int \rho(t', \boldsymbol{x}') \left(x_i' x_j' - \frac{1}{3} \delta_{ij} x^{i'} x^{j'} \right) \mathrm{d}\boldsymbol{x}' . \tag{1.17}$$

In eq. (1.16), the mass quadrupole, rather than a monopole or dipole, moment appears as the leading term of the multipole expansion. It can be intuitively understood that the mass (= monopole) and the kinetic momentum (= dipole) are conservative quantities in an isolated system and thus do not contribute to the radiation process.

Radiated energy

Here, the energy of gravitational wave radiation is briefly discussed. Using eq. (1.16), one can derive the total radiated energy over the solid angle per unit time, or *gravitational luminosity* $\mathcal{L}$, as follows:

$$\mathcal{L}_{\mathrm{gw}} = \frac{G}{5c^5} \left\langle \dddot{Q}_{ij} \dddot{Q}_{ij} \right\rangle . \tag{1.18}$$

Here the angle bracket $\langle ... \rangle$ indicates the spatial average of many wavelengths of emitted gravitational waves. This equation is equivalent to Larmor's fomula in elecrtomagnetic radiation.

To estimate the magnitude of energy radiated as gravitational waves, we scale the $\dddot{Q}_{ij}$ with a combination of physical parameters with basic units as

$$\dddot{Q}_{ij} \sim MR^2 T^{-3} \sim Mv^3 R^{-1} , \tag{1.19}$$

where M, R, T, and v are the typical mass, spatial size, time scale, and velocity of the source, respectively. First, we consider the generattion of gravitational waves in a laboratory-scale experiment in which a dumbbell-like system that consists of two iron balls weighing 100 kg each connected with a 2-meter bar is rotating at a frequency of 100 Hz. By plugging eq. (1.19) into eq. (1.18), one can obtain

$$\begin{aligned} \mathcal{L}_{\mathrm{gw}} &\sim \frac{G}{5c^5} \frac{M^2 v^6}{R^2} \\ &\sim 2.4 \times 10^{-23} \left(\frac{M}{100\,\mathrm{kg}} \right)^2 \left(\frac{v}{4\pi\,\mathrm{m} \times 100\,\mathrm{Hz}} \right)^6 \left(\frac{R}{15\,\mathrm{cm}} \right) \; [\mathrm{erg/s}] . \end{aligned} \tag{1.20}$$

This energy emission rate is extremely small such that it takes about a thousand years to generate energy equivalent to one photon of the cosmic microwave background. Therefore, it is hopeless sto construct an available source of gravitational waves on Earth and people pin their hope on the celestial sources.

For an astrophysical source usually bounded by its own gravity, we can assume that the kinetic energy and the potential energy of the system are comparable so that

$$Mv^2 \sim \frac{GM^2}{R} . \tag{1.21}$$

Using this relation, the gravitational luminosity eq. (1.18) becomes

$$\mathcal{L}_{\mathrm{gw}} \sim 2.3 \times 10^{57} \left(\frac{R}{R_{\mathrm{sch}}} \right)^{-5} \ [\mathrm{erg/s}] . \tag{1.22}$$

Here the spatial size is scaled with the Schwarzschild radius defined by $R_{\mathrm{sch}} \equiv 2GM/c^2$. This estimation indicates that the size of the object is the key property for gravitational wave radiation.

Amplitude

To discuss the amplitude of the radiated gravitational waves, the Newtonian source approximation is applied to eq. (1.16) such that

$$\begin{aligned} h &\sim \frac{1}{r} \frac{2G}{c^4} \frac{\partial^2}{\partial t^2} (MR^2) \sim \frac{1}{r} \frac{2GMv^2}{c^4} \\ &\sim \frac{R_{\mathrm{sch}}}{r} \left(\frac{v}{c} \right)^2 . \end{aligned} \tag{1.23}$$

one can parameterize the emission efficiency of gravitational waves with ϵ written as

$$\epsilon \sim \left(\frac{R_{\mathrm{sch}}}{R} \right) . \tag{1.24}$$

Thus, by rewriting eq. (1.23) with the parameter ϵ, an estimation of the gravitational-wave amplitude can be obtained.

$$h \sim \epsilon^{2/7} \frac{R_{\mathrm{sch}}}{2r} \tag{1.25}$$

$$\sim 1.5 \times 10^{-21} \left(\frac{\epsilon}{0.1} \right)^{2/7} \left(\frac{M}{M_\odot} \right) \left(\frac{r}{17\,\mathrm{Mpc}} \right) . \tag{1.26}$$

Here the mass M and distance r are scaled by the solar mass $M_\odot = 1.989 \times 10^{30}\,[\mathrm{kg}]$ and that from the Earth to the Virgo cluster of about 17 Mpc. Even if an optimistic radiation efficiency of $\epsilon = 10\,\%$ is assumed, the amplitude of gravitational waves from a system as heavy as the Sun is extremely small. For instance, when such a gravitational wave changes the proper distance between two free-falling masses separated by 3 km, the geometrical displacement is about 4.5×10^{-18} m.

1.2   Detected gravitational-wave sources

Since the Advanced LIGO detected the first gravitational wave (GW) event [3, 4], the number of detected gravitational waves has increased even after a few years' observation. Now the sources of all the detected events are the coalescences of compact star binaries

such as black holes and neutron stars [5, 6]. Recently the LIGO Scientific Collaboration and Virgo Collaboration opened a catalog of confident and marginal events of gravitational wave detection [7]. It implies that the accumulation of the detected GW events expands our understanding of scope of the universe. Here, the astrophysical picture of the compact binary coalescence is presented.

1.2.1 Compact binary coalescence

Compact binary coalescences have been regarded as the most promising GW sources for a long time, and thus have become the first GW events directly detected by human beings. A binary system formed by compact stars such as neutron stars, black holes, or white dwarfs, loses its orbital energy by gravitational radiation as the two stars approach each other. The first evidence of this orbital energy loss was discovered by Hulse and Taylor in their long-period radio observation of the pulsar binary PSR B1913+16 [8]. The orbital decay of the pulsar binary shows precise agreement with the energy that gravitational waves carry away from a system. As radiated energy grows as the two stars get closer to their center of gravity, the brightest gravitational wave emission is expected at the moment of collision of the two stars.

The typical compact binary coalescence scenario has three stages. The first stage is called *inspiral*, where the two stars revolve in a quasi-stable circular or elliptic orbit while approaching each other. After experiencing the last hundreds of revolution, the two stars fall into the region where the point mass approximation is no longer valid and then move to the second stage called *merger*. During the merger, the two objects are mixed to form a single compact object. Then, in the last stage, which is *ringdown*, the newborn single object settles to a stationary state through gravitational wave emission. The transitions occur over a period of subseconds to minutes depending on the total mass of the system, although the lifetime of the binary before merging can be in the order of tens of millions of years.

Inspiral phase

A waveform of GWs in the inspiral phase, known as the *chirp* signal, is predictable, and for this reason, the compact binary merger became the first event of direct GW detection. To support a binary system with a circular orbit (= sufficiently small eccentricity), for such a two-body problem, it is convenient to use the relative coordinate $\boldsymbol{x}_0$ and the center-of-mass coordinate $\boldsymbol{x}_{\mathrm{CM}}$, which are determined as

$$\boldsymbol{x}_0 = \boldsymbol{x}_1 - \boldsymbol{x}_2 \,, \tag{1.27}$$

$$\boldsymbol{x}_{\mathrm{CM}} = \frac{m_1 \boldsymbol{x}_1 + m_2 \boldsymbol{x}_2}{m_1 + m_2} \,, \tag{1.28}$$

where (m_1, m_2) and $(\boldsymbol{x}_1, \boldsymbol{x}_2)$ are the mass and the position of the corresponding star labeled as the subscription, respectively. We also denote the total mass by $m = m_1 + m_2$ and the reduced mass by $\mu = m_1 m_2 / m$. If we choose a frame such that $\boldsymbol{x}_{\mathrm{CM}} = 0$, what remains of interest is the single effective particle of mass μ and its coordinate $\boldsymbol{x}_0$. This procedure helps us to simplify the mass quadrupole moment in eq. (1.17) $\rho(t, \boldsymbol{x}) = \mu \delta^3(\boldsymbol{x} - \boldsymbol{x}_0)$, as the following expression:

$$Q_{ij}(t) = \mu \left((x_0)_i (x_0)_j - \frac{1}{3} r_0^2 \, \delta_{ij} \right) . \tag{1.29}$$

For the moment, we restrict the trajectory of the binary system in the xy-plane, which is given by

$$\begin{aligned} x_0(t) &= r_0 \cos(\omega_{\mathrm{s}} t + \pi/2) \,, \\ y_0(t) &= r_0 \sin(\omega_{\mathrm{s}} t + \pi/2) \,, \\ z_0(t) &= 0 \,. \end{aligned} \tag{1.30}$$

Here, the initial phase $\pi/2$ is chosen just for convenience' sake. Then, substituting eq. (1.30) into eq. (1.29) and taking the second derivative with respect to time, we can obtain

$$\ddot{Q}_{11} = 2\mu \, r_0^2 \, \omega_{\mathrm{s}}^2 \, \cos 2\omega_{\mathrm{s}} t \,, \tag{1.31}$$

$$\ddot{Q}_{12} = 2\mu \, r_0^2 \, \omega_{\mathrm{s}}^2 \, \sin 2\omega_{\mathrm{s}} t \,, \tag{1.32}$$

and $\ddot{Q}_{22} = -\ddot{Q}_{11}$. As the equation of mass quadrupole radiation eq. (1.16) is given by

$$h_+ = \frac{1}{r} \frac{G}{c^4} (\ddot{Q}_{11} - \ddot{Q}_{22}) \,, \tag{1.33}$$

$$h_\times = \frac{2}{r} \frac{G}{c^4} \ddot{Q}_{12} \,, \tag{1.34}$$

the amplitude of the two polarizations of the GW is described with the source parameters μ, r_0, and ω as

$$h_+(t) = \frac{1}{r} \frac{4G\mu \, \omega_{\mathrm{s}}^2 \, r_0^2}{c^4} \cos 2\omega_{\mathrm{s}} t_{\mathrm{ret}} \,, \tag{1.35}$$

$$h_\times(t) = \frac{1}{r} \frac{4G\mu \, \omega_{\mathrm{s}}^2 \, r_0^2}{c^4} \sin 2\omega_{\mathrm{s}} t_{\mathrm{ret}} \,. \tag{1.36}$$

Now, we release the trajectory of the binary system from the xy-plane to an orbit facing an arbitrary direction. In such a situation, if we assume that the observer is sufficiently far from the source, the observation of inclined plain waves can be regarded as that of axis-aligned plain waves with an inclined line of sight as illustrated in fig. 1.2. From the observational point of view, we can access information about the inclination of the source ι as the fainted amplitude which can be written as

$$h_+(t) = \frac{1}{r} \frac{4G\mu \, \omega_{\mathrm{s}}^2 \, r_0^2}{c^4} \left(\frac{1 + \cos^2 \iota}{2} \right) \cos 2\omega_{\mathrm{s}} t_{\mathrm{ret}} \,, \tag{1.37}$$

$$h_\times(t) = \frac{1}{r} \frac{4G\mu \, \omega_{\mathrm{s}}^2 \, r_0^2}{c^4} \cos \iota \, \sin 2\omega_{\mathrm{s}} t_{\mathrm{ret}} \,. \tag{1.38}$$
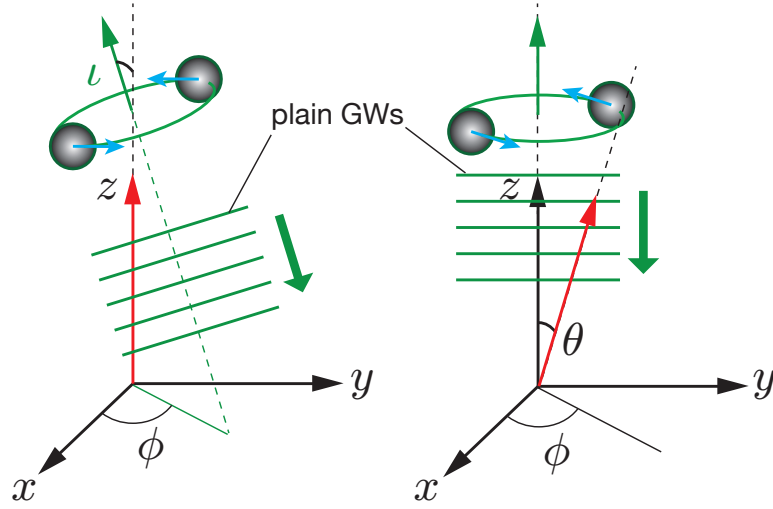
Fig. 1.2. Observation of plain GWs from the inclined binary system with a line of sight aligned to the z-axis (*left*) and the face-on binary system with a line of sight oriented to the (θ, ϕ) direction (*right*).

To eliminate degeneracy of the source frequency ω_s with the separation distance of the two stars r_0 as it gradually decreases while holding the Kepler's harmonic law of $\omega_s^2 = Gm/r_0^3$, we introduce the *charp mass* M_c, which is defined as

$$M_c \equiv \mu^{3/5} \, m^{2/5} = \frac{(m_1 m_2)^{3/5}}{(m_1 + m_2)^{1/5}} \,. \tag{1.39}$$

Using this chirp mass, we finally obtain the expression of the chirp signal as

$$h_+(t) = \frac{4}{r} \left(\frac{GM_c}{c^4} \right)^{5/3} \left(\frac{\pi f_{gw}}{c} \right)^{2/3} \left(\frac{1 + \cos^2 \iota}{2} \right) \cos(2\pi f_{gw} t_{ret}) \,, \tag{1.40}$$

$$h_\times(t) = \frac{4}{r} \left(\frac{GM_c}{c^4} \right)^{5/3} \left(\frac{\pi f_{gw}}{c} \right)^{2/3} \cos \iota \, \sin(2\pi f_{gw} t_{ret}) \,, \tag{1.41}$$

where f_{gw} is the frequency of the GWs associated with the source frequency such that $f_{gw} = \omega_s/\pi$. These expressions highlight the importance of the chirp mass M_c, which summarizes the information of the source mass through the chirp signal.

The primary feature of the chirp signal is that its frequency f_{gw} increases as the binary system evolves to coalescence, as the separation of the two stars must decrease for the system to compensate for the energy loss to GWs. Recalling the Kepler's harmonic law, the orbital energy of the binary system can be written as

$$E_{orbit} = -\frac{Gm_1 m_2}{2r_0^2} = -\left(\frac{G^2 M_c^5 \omega_{gw}}{32} \right)^{1/3} \,. \tag{1.42}$$

On the other hand, the luminosity of GW radiation can be obtained by substituting eq. (1.31) and eq. (1.32) into eq. (1.18).

$$\mathcal{L}_{\text{gw}} = \frac{32}{5} \frac{c^5}{G} \left(\frac{G M_c \omega_{\text{gw}}}{2 c^3} \right)^{10/3} \tag{1.43}$$

By equating eq. (1.43) to $-\mathrm{d}E_{\text{orbit}}/\mathrm{d}t$ given in eq. (1.42), one can obtain

$$\dot{f}_{\text{gw}} = \frac{96}{5} \pi^{8/3} \left(\frac{G M_c}{c^3} \right)^{5/3} f_{\text{gw}}^{11/3} \tag{1.44}$$

The integration of this equation tells us that the frequency f_{gw} diverges at a finite value of time t_0. Here, the time to coalescence is denoted as $\tau \equiv t_0 - t$; furthermore, the evolution of the chirp frequency follows the equation below.

$$f_{\text{gw}} = \left(\frac{5}{256} \right)^{3/8} \frac{1}{\pi} \left(\frac{G M_c}{c^3} \right)^{-5/8} \tau^{-3/8} \tag{1.45}$$

As shown in fig. 1.3, the frequency as well as the amplitude of the chirp signal increases by the end of the inspiral phase. For instance, the chirp signal from a $1.4 M_\odot$-$1.4 M_\odot$ neutron star binary has a frequency and amplitude of,

$$f_{\text{gw}} \approx 134 \text{ Hz} \left(\frac{M_c}{1.21 \, M_\odot} \right)^{-5/8} \left(\frac{\tau}{1 \text{ sec}} \right)^{-3/8}, \tag{1.46}$$

$$h \approx 2.5 \times 10^{-22} \left(\frac{M_c}{1.21 \, M_\odot} \right)^{5/3} \left(\frac{\tau}{1 \text{ sec}} \right)^{-1/4} \left(\frac{r}{17 \text{ Mpc}} \right)^{-1}, \tag{1.47}$$

The GW radiation in the chirp waveform ends when the radial distance of the binary decreases beyond the innermost stable circular orbit (ISCO), where stable circular orbits are no longer allowed. In Schwarzschild spacetime, the orbital radius corresponding to ISCO is located at r_{ISCO}, which is given by

$$r_{\text{ISCO}} = \frac{6 G m}{c^2} = 3 R_{\text{sch}}. \tag{1.48}$$

Therefore, the increase in the source frequency reaches its peak when $r_0 \simeq r_{\text{ISCO}}$. Using Kepler's law again, the source frequency at the ISCO is calculated as

$$f_{\text{ISCO}} = \frac{1}{2\pi} \frac{1}{6\sqrt{6}} \frac{c^3}{G m}$$

$$\simeq 2.2 \text{ kHz} \left(\frac{M_\odot}{m} \right). \tag{1.49}$$

Seeing eq. (1.49), f_{ISCO} turns out to depend on the source mass. For instance, a $1.4 M_\odot$-$1.4 M_\odot$ neutron star binary has $f_{\text{ISCO}} \sim 800$ Hz and a $30 M_\odot$-$30 M_\odot$ black hole binary has $f_{\text{ISCO}} \sim 36$ Hz. Note that its GW frequency is twice that of the source frequency.
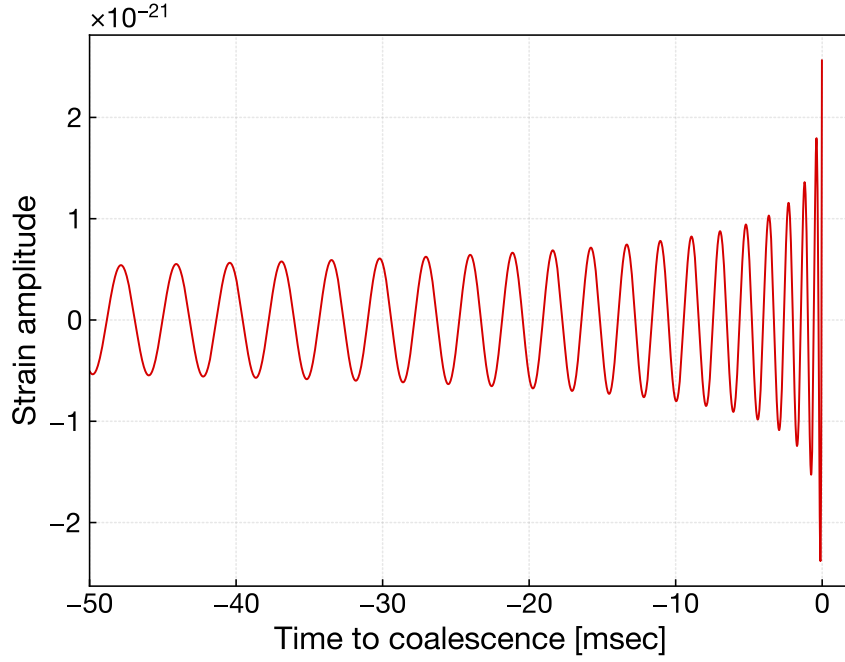
Fig. 1.3. Calculated chirp signal from a $1.4M_\odot$-$1.4M_\odot$ neutron star binary from 17 Mpc as distant as the Virgo cluster.

A more precise prediction of the chirp waveform is a subject for the post-Newtonian expansion, which treats the background spacetime curvature with the velocity of the source as if they are correlated to each other. In the framework of the post-Newtonian expansion, even though it is still assumed to be a low velocity and weak field, a slightly deviated chirp signal can be reproduced with $\mathcal{O}(v/c)$, the higher-order perturbations of relativistic terms. Thus, the source parameters such as individual mass and spin of the binary can be extracted through the coefficients of the post-Newtonian terms. Moreover, precise estimation of the post-Newtonian terms enables us to distinguish the modified theories of gravity as successors of the general relativity.

To distinguich these signals from the detector noise, data analysts use the *matched filter* algorithm that compares the detector output to the library of the waveform templates that scan the parameter space of binary coalescences.

Merger and ringdown phase

Although the waveform of GWs in the inspiral phase is predictable with sufficient precision, in the merger phase the dynamics of the binary system can no longer be approximated to point-mass-like or low-velocity ones. Therefore, numerical simulations, a field called *numerical relativity*, are one of the few powerful tools for demonstrating the coalescence, including the effects of fluid dynamics, relativistic motions, and evolutions of background curvature.

The waveform in the ringdown phase is dominated by a characteristic oscillation called the quasinormal mode (QNM), assuming the remnant object is a black hole. As the black hole just after the coalescence perturbs the spacetime, it will decay to a stationary state through damped pulsation associated with gravitational wave radiation. This indicates that the gravitational waves from the quasinormal mode include information about the spacetime structure beyond the event horizon. Thus, the gravitational waves can be used as a probe for properties of the black hole. Black holes and neutron stars have quasinormal modes for which gravitational waves can provide information about their equations of state to exclude inconsistent theoretical models.

1.3   Gravitational wave detection with laser interferometer

To detect gravitational waves, one wants to measure the proper distance between two separated points of the coordinate. We saw in section 1.1.2 that the gravitational waves make tidal displacements on the points of the coordinate marked by the free-falling masses. One way to reveal this variation of the space-time structure is to measure the round-trip travel time of light beams sent over the distance.

The mainstream of building gravitational wave detectors in this several decades is in the methodology of laser interferometer. After the famous J. Weber's resonant bar experiment in 1960's [9], people started developing the laser interferometer to detect gravitational waves in 1970's [10]. The significant advantage in the use of the laser interferometer is that the observational bandwidth can be much greater than that of the resonant bar detector, which enables us to track the frequency evolution of the signals or to access the waveform of the incident gravitational waves.

The current interferometers in operation of observing gravitational waves typically consists of a Michelson inteferometer with sensitivity enhancement by the addition of Fabry-Perot optical cavities.

1.3.1   Michelson interferometer

The Michelson interferometer is an extraordinarily accurate instrument for measuring difference in the travel time of light in its arms. The instrument is known to many physicists for the experiment of A. Michelson and E. Morley in 1887 which showed the non-existence of the luminiferous æther [11]. Interferometry of the light beams transmitted through each perpendicular but equated-length path shows the perturbation of the space-time as a change in detected power. When gravitational wave with a certain frequency pass through the inteferometer, it modulates the microscopic optical length of the arms at the same frequency.
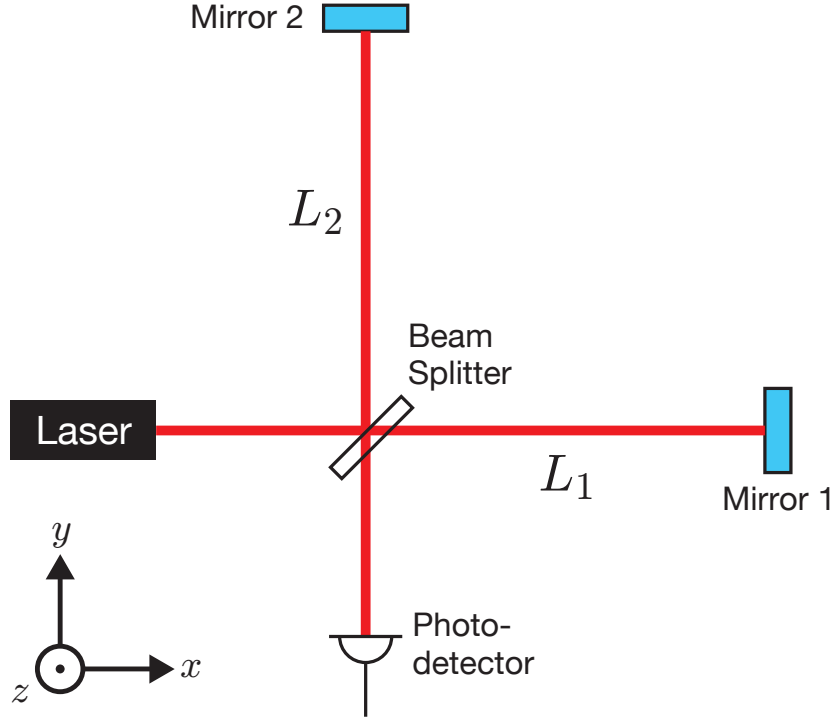
Fig. 1.4. Michelson interferometer

As a result, the gravitational wave changes the interference condition of the output beam. Letting the macroscopic arm length be L and the microscopic variation of the optical length be ΔL, the amount of the change in the arm The amount of the microscopic optical-length variation ΔL is approximately proportional to the macroscopic baseline length of the arm L, so that,

$$\Delta L \sim hL \,, \tag{1.50}$$

where h is the amplitude of the gravitational wave. Therefore, we can get straightforward implication that a Michelson interferometer with longer baseline acquires larger displacement in its arm length.

The simplest configuration of the Michelson interferometer consists of a monochromatic light source, 50%-50% beam splitter (BS), two end mirrors, and some photosensitive devices such as photodetector (PD), which are illustrated in fig. 1.4. he electromagnetic field of the induced laser with the laser angular frequency of Ω is written as

$$E_{\text{in}} = E_0 \, e^{i\Omega t} \,. \tag{1.51}$$

This laser beam is divided into two paths respectively in x-direction and y-direction at the BS. Both beams are reflected at the end mirrors and then recombined at the BS again. Assuming

that the phase shift in each arm is ϕ_1 and ϕ_2, one can write the electromagnetic field of the recombined beam as

$$E = E_1 \, e^{\mathrm{i}(\Omega t - \phi_1)} - E_2 \, e^{\mathrm{i}(\Omega t - \phi_2)} \,. \tag{1.52}$$

Here E_1 and E_2 denote the amplitude of the field that comes from each arm respectively. In the ideal case with completely symmetric mirrors, we have $E_1 = E_2 = E_0/2$. However, in realistic case where the reflectivity of the end mirrors differ from each other, the two beams are no longer symmetric and their amplitude means $E_1 \neq E_2$. The power of the light incident to the photodetector (PD) is

$$P = |E|^2 = E_1^2 + E_2^2 + 2E_1 E_2 \cos(\phi_1 - \phi_2) \tag{1.53}$$

The power has a cosinusoidal from with respect to the phase difference $\phi_1 - \phi_2$. Therefore, one can regard the Michelson interferometer as an instrument that detects the phase shift between two beams with different paths.

Response of Michelson interferometer to GWs

Suppose that +-mode gravitational waves meet the Michelson interferometer in the z-direction. Then the world interval of the perturbated space-time can be written as

$$\mathrm{d}s^2 = -c^2\mathrm{d}t^2 + (1+h)\mathrm{d}x^2 + (1-h)\mathrm{d}y^2 + \mathrm{d}z^2 \,. \tag{1.54}$$

As the laser beam travels along the null vector which satisfies $\mathrm{d}s^2 = 0$, The beam along the x-axis is expressed as

$$\frac{\mathrm{d}x}{\mathrm{d}t} = \pm\frac{c}{\sqrt{1+h}} \simeq \pm\left(1 - \frac{1}{2}h\right)c \,. \tag{1.55}$$

Here, we determine that the positive sign indicates the light going toward $+x$-direction. Integrating the $\mathrm{d}x$ along a round trip path between the BS and the x-end mirror gives

$$\int \mathrm{d}x = 2L_1 = c\int_{t-\Delta t_1}^{t} \left(1 - \frac{1}{2}h(t')\right)\mathrm{d}t' \,. \tag{1.56}$$

The round trip time of the beam is

$$\Delta t_1 = \frac{2L_1}{c} + \frac{1}{2}\int_{t-2L_1/c}^{t} h(t')\mathrm{d}t' \,. \tag{1.57}$$

Consequently, we can obtain the phase shift by the gravitational waves in the x-arm light.

$$\phi_1 = \Omega\,\Delta t_1 = \frac{2L_1\Omega}{c} + \frac{\Omega}{2}\int_{t-2L_1/c}^{t} h(t')\mathrm{d}t' \tag{1.58}$$

Applying the same approach, the phase shift in the y-arm is

$$\phi_2 = \Omega\,\Delta t_2 = \frac{2L_1\Omega}{c} - \frac{\Omega}{2}\int_{t-2L_2/c}^{t} h(t')\mathrm{d}t'\,. \tag{1.59}$$

Therefore, the phase difference between the two beams $\phi_1 - \phi_2$ is

$$\phi_1 - \phi_2 = \frac{2L_-\Omega}{c} + \delta\phi_{\mathrm{GW}} \tag{1.60}$$

$$\delta\phi_{\mathrm{GW}} = \Omega\int_{t-2L/c}^{t} h(t')\mathrm{d}t' \tag{1.61}$$

where it is assumed $L_1 \simeq L_2 \simeq L$、$L_- \equiv L_1 - L_2$. Equation (1.60) shows the change in the phase difference induced by the gravitational waves.

Frequency response of Michelson interferometer to GWs

Fourier transformation of the $h(t)$ is written as follows.

$$h(t) = \int_{-\infty}^{\infty} h(\omega)e^{i\omega t}\mathrm{d}\omega \tag{1.62}$$

Using (1.62), we can rewrite the equation of the phase shift by GWs (1.60) as

$$\begin{aligned}
\delta\phi_{\mathrm{GW}} &= \Omega\int_{t-2L/c}^{t}\int_{-\infty}^{\infty} h(\omega)e^{i\omega t'}\mathrm{d}\omega\mathrm{d}t' \\
&= \int_{-\infty}^{\infty}\frac{2\Omega}{\omega}\sin\left(\frac{L\omega}{c}\right)e^{-iL\omega/c}h(\omega)e^{i\omega t}\mathrm{d}\omega \\
&= \int_{-\infty}^{\infty} H_{\mathrm{MI}}(\omega)\,h(\omega)e^{i\omega t}\mathrm{d}\omega
\end{aligned} \tag{1.63}$$

$$H_{\mathrm{MI}}(\omega) = \frac{2\Omega}{\omega}\sin\left(\frac{L\omega}{c}\right)e^{-iL\omega/c}\,, \tag{1.64}$$

The $H_{\mathrm{MI}}(\omega)$ in this equation represents the frequency response of the Michelson interferometer to GWs.

The magnitude of the response $|H_{\mathrm{MI}}(\omega)|$ is visualized in fig. 1.5. When the arm length is much shorter than the wavelength of the gravitational wave, the frequency response of the Michelson inteferometer can be approximated as $H_{\mathrm{MI}} \sim 2\Omega L/c$, indicating that a detector with longer arm length has greater sensitivity to gravitational waves. However, longer arms beyond a certain length doesn't make improvement on the sensitivity since cancellation of the phase shift induced by the gravitational waves occurs during the round trip of the laser beam. The sensitivity starts the roll-off at the frequency where the following condition is satisfied:

$$\omega = \frac{\pi c}{2L}\,. \tag{1.65}$$
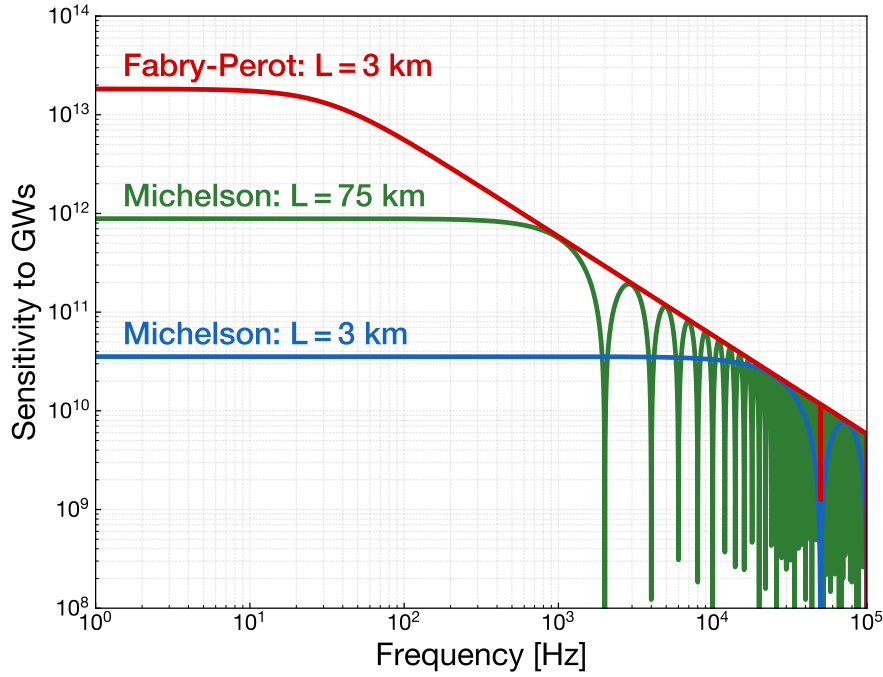
Fig. 1.5. Frequency response of the Michelson interferometer and the Fabry-Perot inteferometer to gravitational waves. It is assumed that the mirrors of the Fabry-Perot interferometer have the power transmissivity; $t_1^2 = 0.004$ and $t_2^2 = 10$ ppm.

For a gravitational wave of 1 kHz, the optimal arm length is about 75 km.

On the other hand, constructing the laser interfometer with such a large baseline length is impractical for geographical or technical reasons. To circumvent thi issue, we use Fabry-Perot cavities in the Michelson interferometer. In this configuration called the "Fabry-Perot Michelson interferometer", the effective arm length can be elongated beyond the physical separation of the mirrors.

1.3.2   Fabry-Perot interferometer

A Fabry-Perot interferometer (or cavity) is composed of two mirrors facing each other as shown in Fig.1.6. The light incident on the front mirror is reflected back and forth between the two mirrors repeatedly. A fraction of the light stored in the cavity is reflected back along the incident direction and a fraction is transmitted through the end mirror. Now, if the electric field of the input beam is denoted as E_i, the amplitude of the reflected light E_r is

$$E_\mathrm{r} = E_\mathrm{i} \left(r_1 - \frac{t_1^2 r_2 e^{-i\Phi}}{1 - r_1 r_2 e^{-i\Phi}} \right) . \tag{1.66}$$

Here, $\Phi = 2L\Omega/c$ is the phase shift through a round trip of the cavity, r_1 and r_2 are the amplitude reflectivities, and t_1 and t_2 are the amplitude transmissivities. The amplitude of
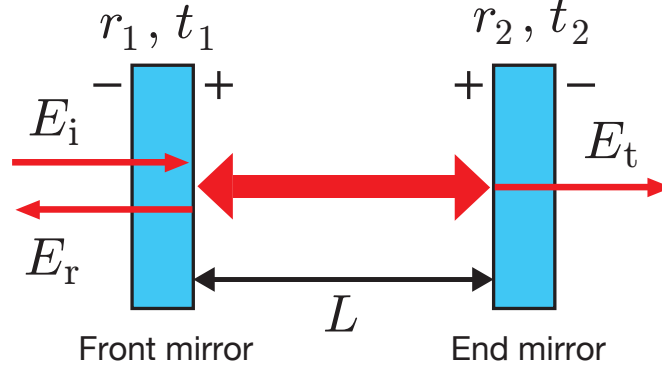
Fig. 1.6. Fabry-Perot interferometer

the transmitted light E_t is

$$E_\text{t} = E_\text{i} \frac{t_1 t_2 e^{-i\Phi/2}}{1 - r_1 r_2 e^{-i\Phi}} . \tag{1.67}$$

With these expressions, we can obtain the amplitude reflectivity and amplitude transmissivity of the FP cavity, r_cav and t_cav, respectively, as

$$r_\text{cav} = r_1 - \frac{t_1^2 r_2 e^{-i\Phi}}{1 - r_1 r_2 e^{-i\Phi}} , \tag{1.68}$$

$$t_\text{cav} = \frac{t_1 t_2 e^{-i\Phi/2}}{1 - r_1 r_2 e^{-i\Phi}} . \tag{1.69}$$

Then the power of the reflected and transmitted light P_r and P_t, respectively, are

$$P_\text{r} = |E_\text{r}|^2 = \frac{[(t_1^2 + r_1^2)r_2 - r_1]^2 + 4r_1 r_2 (r_1^2 + t_1^2) \sin^2(\Phi/2)}{(1 - r_1 r_2)^2 [1 + F \sin^2(\Phi/2)]} |E_\text{i}|^2 , \tag{1.70}$$

$$P_\text{t} = |E_\text{t}|^2 = \left(\frac{t_1 t_2}{1 - r_1 r_2} \right)^2 \frac{1}{1 + F \sin^2(\Phi/2)} |E_\text{i}|^2 , \tag{1.71}$$

where

$$F \equiv \frac{4 r_1 r_2}{(1 - r_1 r_2)^2} . \tag{1.72}$$

From the equation above, resonant condition can be determined as

$$\Phi = 2\pi n \qquad (n\text{: natural number}) , \tag{1.73}$$

in which state the transmitted light and intracavity light have maximum intensities. By rewriting the condition with the wavelength of the light, we obtain

$$2L = n\lambda \qquad (n\text{: natural number}) . \tag{1.74}$$

Therefore, in other words, the resonant condition is that the round trip distance of the FP cavity is a whole-integer multiple of the wavelength.

Using Eq. (1.71), the transmittance with respect to the the laser frequency can be plotted as shown in Fig. fig. 1.7. It can be seen that the transmittance has periodic peaks as the laser frequency shifts. The frequency range corresponding to the period is called the *free spectral range* (FSR), which is written as

$$\nu_{\mathrm{FSR}} = \frac{\omega_{\mathrm{FSR}}}{2\pi} = \frac{2L}{c} . \tag{1.75}$$

Then, recalling that eq. (1.71), we can derive the full width at half maximum (FWHM) of
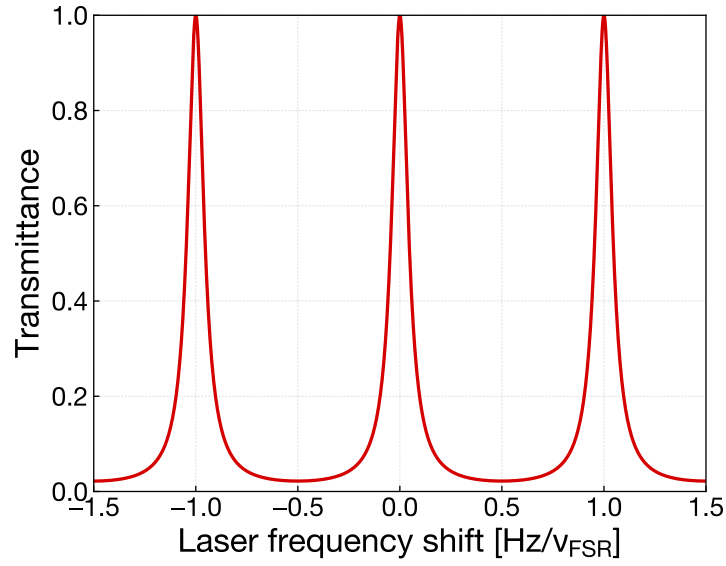
Fig. 1.7. Normalized transmittance of a Fabry-Perot interferometer with $r_1 = 0.75$, $r_2 = 0.99$ and $\mathcal{F} \simeq 10$

the peak ν_{FWHM} from the following equation:

$$\frac{1}{1 + F \sin^2(\pi L\, \nu_{\mathrm{FWHM}}/c)} = \frac{1}{2} . \tag{1.76}$$

Under the approximation that $\pi L\, \nu_{\mathrm{FWHM}}/c = \pi\, \nu_{\mathrm{FWHM}}/2\nu_{\mathrm{FSR}} \ll 1$ [3], one can perform a Taylor expansion for the sine.

$$\nu_{\mathrm{FWHM}} = \frac{c(1 - r_1 r_2)}{2\pi L \sqrt{r_1 r_2}} \tag{1.77}$$

Here, the fraction of ν_{FWHM} and ν_{FSR} is called *finesse*, a value which represents the sharpness of the resonant peaks described as

$$\mathcal{F} \equiv \frac{\nu_{\mathrm{FSR}}}{\nu_{\mathrm{FWHM}}} = \frac{\pi \sqrt{r_1 r_2}}{1 - r_1 r_2} . \tag{1.78}$$

---

[3] Because the FP interferometer has in general a finesse (described in later eq. (1.78)) much larger than unity, this approximation is valid enough.

From eq. (1.78), it turns that the finesse is determined only through the reflectivity of the mirrors. With a reflectivity closer to unity, the resonant peaks plotted in fig. 1.7 become sharp.

Frequency response of Fabry-Perot interferometer to GWs

One can calculate the n times round trip time of the light in the FP cavity Δt_n in the same manner as from eq. (1.54) to eq. (1.57).

$$\Delta t_n \simeq \frac{2L_1}{c}n + \frac{1}{2}\int_{t-2L_1n/c}^{t} h(t')\mathrm{d}t' \tag{1.79}$$

Through a Fourier transformation of eq. (1.62), Δt_n becomes

$$\Delta t_n \simeq \frac{2L_1}{c}n + \frac{1}{2}\int_{-\infty}^{\infty} h(\omega)\frac{1 - e^{-2iL\omega n/c}}{i\omega}e^{i\omega t}\mathrm{d}\omega . \tag{1.80}$$

Now recalling that eq. (1.66), the reflected beam is

$$E_{\mathrm{r}} = E_{\mathrm{i}}\left(r_1 - t_1^2 r_2 \sum_{n=1}^{\infty} r_1^{n-1}\, r_2^{n-1}\right)e^{-i\Phi n} . \tag{1.81}$$

Substituting $\Phi n = \Omega\,\Delta t_n$ into the equation above and linearizing h under the assumption that $|h| \ll 1$, we can get

$$\frac{E_{\mathrm{r}}}{E_{\mathrm{i}}} \simeq r_1 - \frac{t_1^2 r_2 e^{-i\Phi}}{1 - r_1 r_2 e^{-i\Phi}} + \frac{t_1^2 r_2 e^{-i\Phi}}{1 - r_1 r_2 e^{-i\Phi}}\int_{-\infty}^{\infty}\frac{\Omega}{2\omega}h(\omega)\frac{1 - e^{iL\omega/c}}{1 - r_1 r_2 e^{-\Phi}e^{-iL\omega/c}}e^{i\omega t}\mathrm{d}\omega . \tag{1.82}$$

Assuming the resonance that satisfies $\phi = 2\pi n$, the following equation is obtained:

$$\frac{E_{\mathrm{r}}}{E_{\mathrm{i}}} \simeq \frac{r_1 - (r_1^2 + t_1^2)r_2}{1 - r_1 r_2}\left[1 - i\int_{-\infty}^{\infty} H_{\mathrm{FP}}(\omega)\,h(\omega)e^{i\omega t}\mathrm{d}\omega\right] \tag{1.83}$$

$$H_{\mathrm{FP}}(\omega) = \frac{\alpha_{\mathrm{c}}\Omega}{\omega}\frac{\sin(\omega L/c)}{1 - r_1 r_2 e^{-2i\omega L/c}}e^{-i\omega L/c} \tag{1.84}$$

$$\alpha_{\mathrm{c}} \equiv \frac{t_1^2 r_2}{r_1 - (r_1^2 + t_1^2)r_2} \tag{1.85}$$

The $H_{\mathrm{FP}}(\omega)$ indicates the frequency response of the FP interferometer to gravitational waves.

For clarity, taking the magnitude of $H_{\mathrm{FP}}(\omega)$, we get

$$|H_{\mathrm{FP}}(\omega)| = \frac{\alpha_{\mathrm{c}}\Omega}{\omega(1 - r_1 r_2)}\frac{|\sin(\omega L/c)|}{\sqrt{1 + F\sin^2(\omega L/c)}} . \tag{1.86}$$

In the case of $\omega L/c \ll 1$,

$$|H_{\mathrm{FP}}(\omega)| \simeq \frac{\alpha_{\mathrm{c}}\Omega}{\omega(1 - r_1 r_2)}\frac{\omega L}{c\sqrt{1 + (\sqrt{F}L\omega/c)^2}}$$

$$= \frac{\alpha_{\mathrm{c}}\Omega}{\omega(1 - r_1 r_2)}\frac{1}{\sqrt{1 + (\tau\omega)^2}} , \tag{1.87}$$

$$\tau = \frac{\sqrt{F}L}{c} = \frac{2L}{\pi c}\mathcal{F} . \tag{1.88}$$

From this equation, we can find that the FP interferometer has a 1st-order low pass response to gravitational waves, as illustrated in fig. 1.5. The time constant τ determined by eq. (1.88) is the average of storage time of light inside the cavity. Hence, the roll-off frequency of the low pass response is written as

$$\nu_{\rm c} = \frac{\omega_{\rm c}}{2\pi} = \frac{1}{2\pi\tau} \,. \tag{1.89}$$

1.3.3   Noise sources

Owing to the tiny interaction of gravitational waves with matter, the GW detectors are susceptible to disturbances from any kinds of noise sources. Here, typical noise sources are briefly summarized.

Quantum noise

Interferometric GW detection has some fundamental noise sources that are often called quantum noise; they are caused by the use of laser power. The main sources of the quantum noise is shot noise and radiation pressure noise. Shot noise is a noise caused by the quantum fluctuation of the number of photons in the laser beam. Radiation pressure noise is a noise induced by fluctuation of the radiation pressure acting on the mirror surface. These quantum fluctuations are the conjugate quantities tied with the uncertainty principle, and they therefore influence the inteferometer sensitivity.

Thermal noise

The thermal vibrations of atoms with finite temperature cause fluctuations in the surface axial position and elastic shapes of the mirror, resulting in a fluctuation in the optical path length of the interferometer. This noise is generally called *thermal noise*. Thermal noise can be categorized into two forms of noise: the one that originates from the substrate or the coating layers of the mirror is called *mirror thermal noise*, the one caused by the suspension wires is called *suspension thermal noise*.

The impact of thermal noise is related to the mechanical loss of the materials via the fluctuation-dissipation theorem. To reduce the impact of thermal noise, one should choose a material with a high quality factor for the mirrors and the suspension components. Some of advanced gravitational wave detectors employ fused silica as the material of the mirror substrate and the suspension fibers owing to its high mechanical Q-factor ($\sim 10^7$) at room temperature. Thermal noise may also be mitigated by lowering the temperature, which is the strategy the KAGRA employs. Owing to dependence of the mechanical quality factor on temperature, fused silica does not exhibit a superior performance in cryogenic situations. On

the other hand, sapphire and silicon show high mechanical qualities in cryogenic temperatures and thus have become candidate materials for the mirror substrate.

Seismic noise

Seismic noise is an inevitable disturbance experienced by gravitational wave detectors constructed on the Earth. Continuous and random motion of the ground shakes the mirror, which results in uncertainty regarding the optical cavity length. This noise is the main target for the vibration isolation system, which aims to attenuate its impact on the gravitational wave detector. Hence, a more detailed description will be presented in the next chapter.

1.4 Targets and outline of this thesis

The goal of this research was to build vibration isolation systems for KAGRA and to achieve the required performances for the design sensitivity of the interferometer. In particular, this research focused on the 13.5-meter-tall vibration isolation system, the largest of the main mirrors forming the 3 km arm cavities. This study was carried out when the KAGRA was being upgraded. At that time, the primary components of the optics, mechanics, and electonics were installed and tested to achieve fully configurated operation. The vibration isolation system for the main mirrors was first assembled, installed, and tested in this study at the underground site as it is difficult to perform a prototype experiment owing to its large dimension. Although the mechanical components had been individually tested, the performance of the entire assembly was determined by installations and adjustments at the practical site. Moreover, the electric devices for the control of the vibration isolation system should be tuned according to the infrastructure of the digital system adopted in KAGRA. Therefore, the installation and performance test of the vibration isolation systems are indispensable to realizing the gravitational wave observation of KAGRA with its design sensitivity.

The outline of this thesis is as follows. Chapter 2 describes the basics of the vibration isolation and suspension systems. Some mechanisms of low-frequency oscillators used in the KAGRA suspension systems are also presented. Chapter 3 provides details about the vibration isolation system for the main mirrors called Type-A suspension. In this chapter, an overview of the global system of the KAGRA interferometer is provided first, and then the conceptual design of the suspensions and the required performances are mentioned. Then a detailed setup of the instruments, such as the mechanical components and elecrotic devices, are described. Chapter 4 discusses the control design of the vibration isolation systems. As explained in this chapter, the vibration isolation systems need to have controllability of the suspended stages to allow the interferometer to secure stable operation. As the dynamics of the vibration isolation systems can be represented with a mathematical model with good

accuracy, it is helpful to predict the behavior of the nominal system in order to compare it with the measurement results. In addition, the feasibility and expected performance of an advanced damping control technique called modal damping is also discussed in this chapter. Chapter 5 is the main achievement of this study describing the experimental results of the performance test of the Type-A suspension. As mentioned later, the Type-A suspension can be divided into two sections, namely tower and payload. This study focuses on the former, which represents the top five stages and has the key components important for the vibration isolation performance. This chapter presents the measured performance of the Type-A tower and discusses its agreement with the requirements. Finally, in chapter 6, the results of the performance test are summarized and then the conclusion and further prospects of this research are mentioned.

Chapter 2

Vibration isolation system

Vibration isolation is an essential technique for terrestrial gravitational wave telescopes. Mirrors in a laser interferometer on the Earth always suffer from seismic disturbances. The simple ideas to reduce the mirror's fluctuation caused by the ground motion are:

1. To place the mirrors at a quiet site.

2. To isolate the mirrors mechanically from the ground.

This chapter describes the basic concepts how to reduce the impact of seismic disturbance on interferometric gravitational wave observation. Section 2.1 mentions the nature of seismic background noise, the source of vibrations.

2.1 Seismic noise

The nature of seismic background noise is studied by J. Peterson [12]. He made a catalog of seismic background noise spectra obtained from a world wide network of the seismograph stations. From the data, one model of the ground spectra called *New High/Low Noise Model* (NHNM/NLNM) is established which provides the upper and lower bounds of the measured seismic motion. Figure 2.1 shows the power spectral density of the NHNM/NLNM together with the seismic spectra measured at all over the world.

At low frequency below 1 mHz, the spectra of seismic motion grows rapidly owing to tidal deformation of the Earth. Such low-frequency seismic motion does not disturb gravitational wave observation as the test masses of terrestrial detectors move with the ground.

There is a protrusion around 0.1–1 Hz in the spectrum which is known as *microseismic peak*. The microseism is caused by ocean waves beating land shores; hence it is observed strongly at locations close to the coasts and weakly in the middle of continents. As the microseismic motion around 0.1–1 Hz is not coherent between the test masses located kilometers apart, it can impede stable operation of the interferometer.
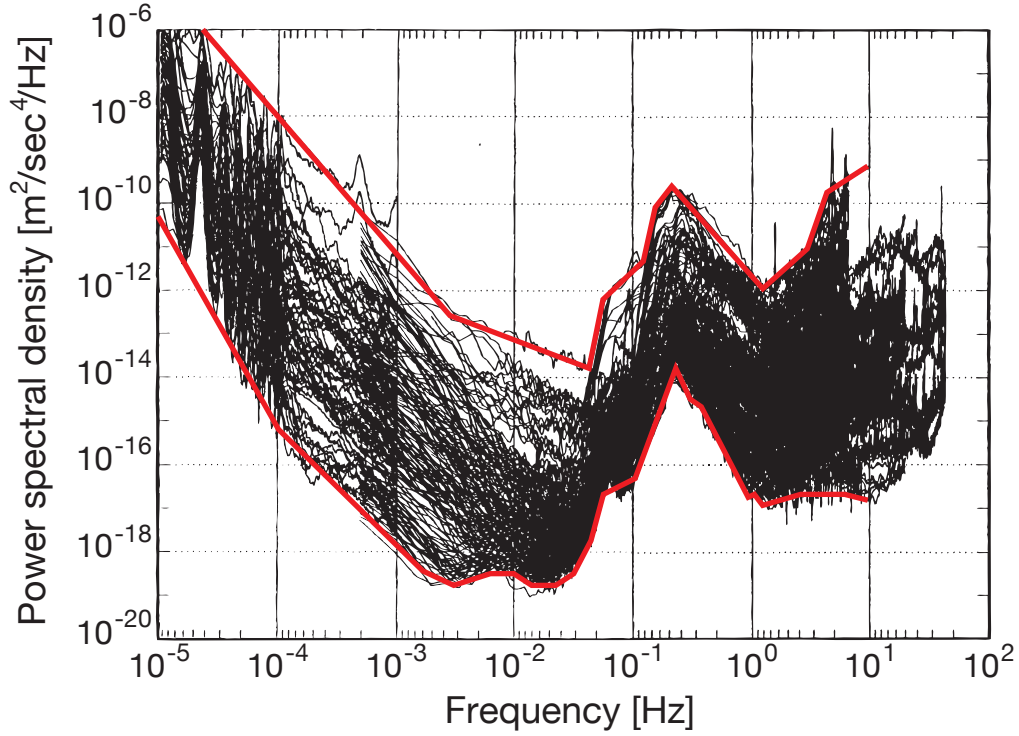
Fig. 2.1. The New High/Low Noise Model (red curves) with the seismic spectra measured in the world wide network of seismometers [12].

Seismic motions at high frequencies above 1 Hz are of interest for those in the field of gravitational wave detection, as terrestrial GW telescopes have the best sensitivity in the frequency band. Figure 2.2 shows typical seismic noise spectra at places where gravitational wave detectors are located. In this frequency region, the magnitude of seismic motion is isotopic, and can be approximated to a simple power law model written as

$$\tilde{x}_{\mathrm{seis}}(f) = A \times \left(\frac{f}{1\ \mathrm{Hz}} \right)^{-2} \quad [\mathrm{m/Hz}^{1/2}]. \tag{2.1}$$

Here, the amplitude factor A, which depends on the site, is typically in the range 10^{-8}–10^{-6}.

The seismic spectra at the underground site in Kamioka are 1–3 orders of magnitude smaller than those at the other sites. This is because the impact of seismic waves on the Earth's surface, which originate from atmospheric and human activities, significantly decreases in the underground environment owing to the hard bedrock. Thus, an underground site benefits from the basic vibration level of the ground in the observational frequency region. On the other hand, the microseism around ~ 0.2 Hz is not attenuated so much as it propagates through the continents.

The seismic motion in the KAGRA site is typically around 10^{-12}–10^{-10} in 10–100 Hz. Assuming the magnitude of displacement induced by gravitational waves in the kilometer-
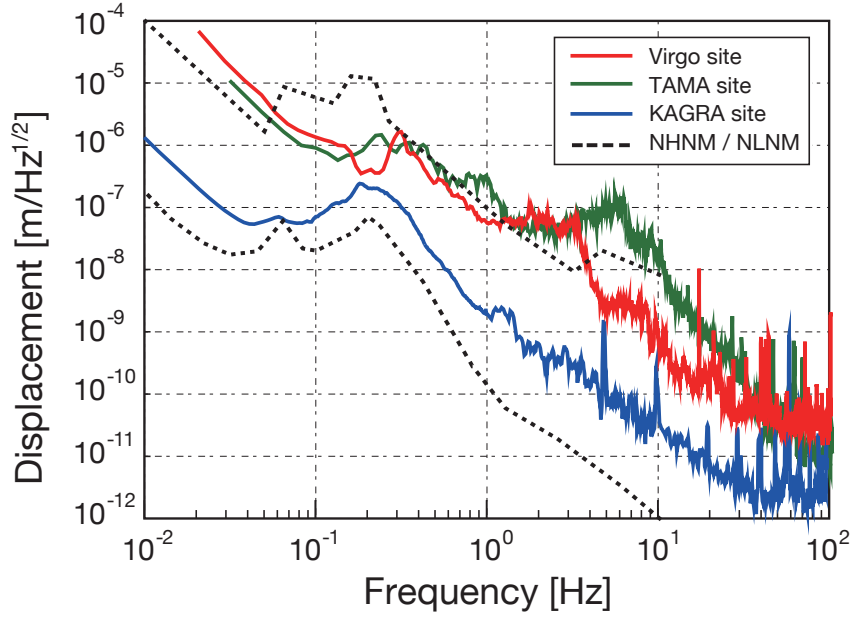
Fig. 2.2. Typical power spectrum density of seismic motions at the sites of the GW detectors [13].

scale interferometer is in the order of 10^{-20} m, the required seismic attenuation factor is about 10^{-8}–10^{-10}.

2.2 Passive vibration isolation

Vibrations propagate via mechanical waves over connected masses, and solid mechanical connections conduct vibrations more efficiently. Passive vibration isolation makes use of soft materials or flexible connections to attenuate the mechanical waves in their transmission path.

Passive vibration isolators can be modeled as a system that contains a mass, spring, and damping elements, and behaves like a harmonic oscillator. Now, we consider a simple one-dimensional harmonic oscillator with a spring and a mass, forgetting the damping elements for now, as depicted in the left panel of fig. 2.3. In the absence of any external force applied to the suspended mass, the equation of motion of this system is written as

$$M\ddot{x}(t) + k\left(x(t) - x_0(t)\right) = 0\,, \tag{2.2}$$

where M is the mass of the payload, k is the spring constant or stiffness, and x and x_0 are the displacements of the payload and the ground, respectively. When this equation is solved

in the frequency domain by taking the Fourier transform, it becomes

$$H(\omega) \equiv \frac{\tilde{x}(\omega)}{\tilde{x_0}(\omega)} = \frac{1}{1 - (\omega/\omega_0)^2}. \tag{2.3}$$

Here we introduced the resonant angular frequency ω_0 of the harmonic oscillation, defined as $\omega_0 \equiv 2\pi f_0 = \sqrt{k/M}$. In eq. (2.3), the $H(\omega)$ is the frequency response of the payload to the motion of the ground and is called *vibration isolation ratio*. It indicates how large vibrations of the supporting point are transmitted to the suspended payload in the frequency region.
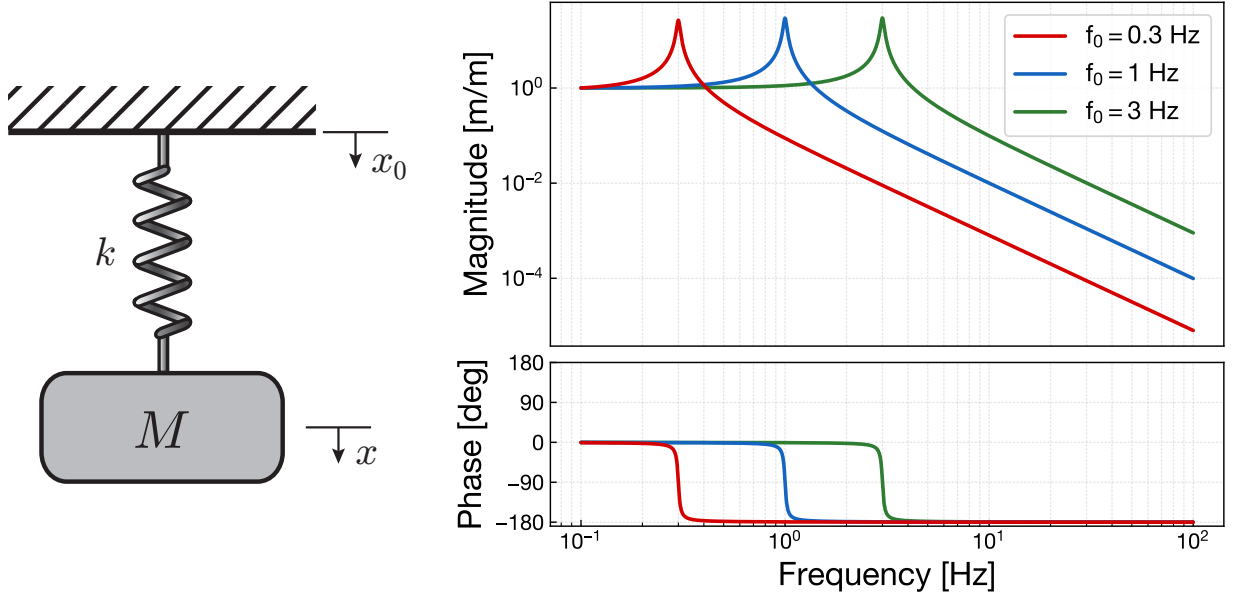
Fig. 2.3. A simple harmonic oscillator composed of a spring and a payload (*left*), and its vibration isolation ratio or frequency response to the ground motion with various resonant frequencies (*right*). For practical reasons, it assumes the quality factor of the resonances as $Q \sim 30$.

The right panel of fig. 2.3 shows the vibration isolation ratio of the harmonic oscillator with changing resonant frequency. At higher frequencies such that $f \gg f_0$, the amplitude of the vibration isolation ratio rolls off proportionally to f^{-2}. This means that the higher the frequency of vibration above the resonance, the higher the filtering effect the harmonic oscillator realizes. Hence, considering a given frequency region of interest such as 10–100 Hz for terrestrial GW observation, a mechanical oscillator with lower resonant frequencies can realize better seismic attenuation performance, as shown by the several curves in fig. 2.3.

In other words, the mechanical oscillator does not perform the function of vibration filtering for the entire frequency region. At lower frequencies of $f \ll f_0$ the ground motion is transferred directly to the payload without being attenuated. It can be assumed that, for non-oscillatory variation, the position of the payload follows that of the suspension point. This behavior is exhibited as the plateau in the magnitude plot of the response in fig. 2.3.
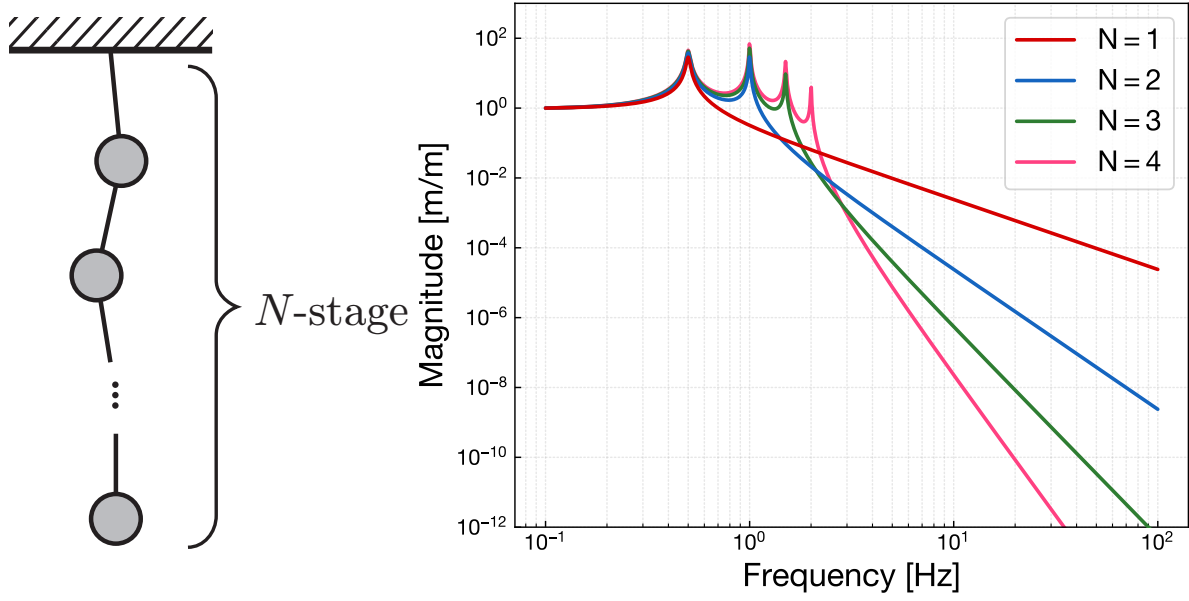
Fig. 2.4. An illustration of N-stage pendulum (*left*), and its vibration isolation ratio with various number of stages (*right*).

The most significant feature of the mechanical oscillator is the resonance, around which frequency of f_0 the ground motion gets rather amplified through the system. This behavior appears as the peak in the magnitude plot and the $-180°$ delay in the phase plot. In the case of an ideal harmonic oscillator with no dissipation, the magnitude of the peak goes infinity at the resonant frequency. However, in a practical system the oscillation cannot diverge owing to the existence of finite dissipation.

Multistage pendulum

n

A kilometer-scale interferometric gravitational wave telescope requires a seismic attenuation factor of $\sim 10^{-8}$–10^{-10} around 10–100 Hz. To achieve this attenuation performance with a single pendulum, for instance, the length of the pendulum must be of the order of 10^6 m, which is unreasonable in practice. The required attenuation performance can be obtained by cascading mechanical oscillators whose resonant frequencies are sufficiently lower than the frequency region of interest ($\gtrsim 10$ Hz). In an N-stage chain of pendula, the vibration isolation ratio is proportional to f^{-2N} at a higher frequency than the resonant frequencies of the chain. Figure 2.4 illustrates the seismic attenuation performance for various numbers of multistage pendulum chains.
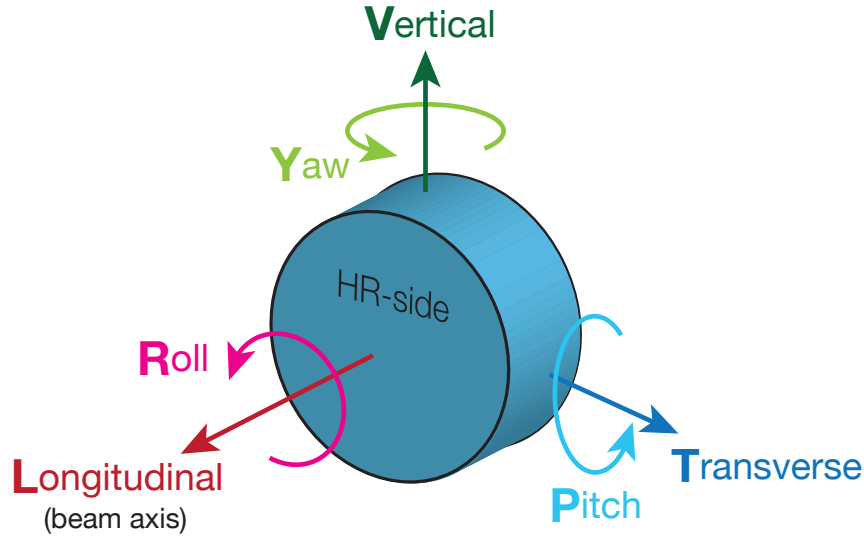
Fig. 2.5. Definition of the degrees of freedom of the suspension's motion. The "HR-side" indicates the surface with high-reflectivity coating. In this thesis, these six degrees of freedom (DoFs) are sometimes abbreviated as L, T, V, R, P, and Y.

2.3   Suspension's degrees of freedom

In the previous section, we considered only one-dimensional motions. However, when we extend objects to 3-dimensional rigid bodies with or without internal motions such as elastic vibration, we must consider the motions in six degrees of freedom (DoFs) for each body. Conventionally, we determine these six DoFs, namely longitudinal, transverse, vertical, roll, pitch, and yaw, as illustrated in fig. 2.5. Three translational axes are the right-handed basis for center-of-mass motions, while three rotational axes are defined so that right-handed screw rotations around the translational axes are positive. In this thesis, the six DoFs, i.e., longitudinal, transverse, vertical, roll, pitch, and yaw, are sometimes abbreviated as L, T, V, R, P, and Y.

To construct optical cavities and an interferometer, the mirror's motions in all the six DoFs are of considerable importance. If the mirror is considered as an optical component, one can easily imagine that the longitudinal translation couples directly to the change in the optical path length, and the pitch and yaw rotation affects beam alignment. However, in the case of gravitational wave detectors, which are required to achieve ultimate sensitivity, further effects of coupled DoFs need to be taken into account.

One of the inevitable coupled DoFs on the Earth is vertical-to-longitudinal coupling. For gravitational wave detectors with long arm lengths constructed on the Earth, because of the finite curvature of the Earth's surface, the direction of the local gravity at places that are far apart from each other results in imperfect parallelism of verticality. It causes the coupling
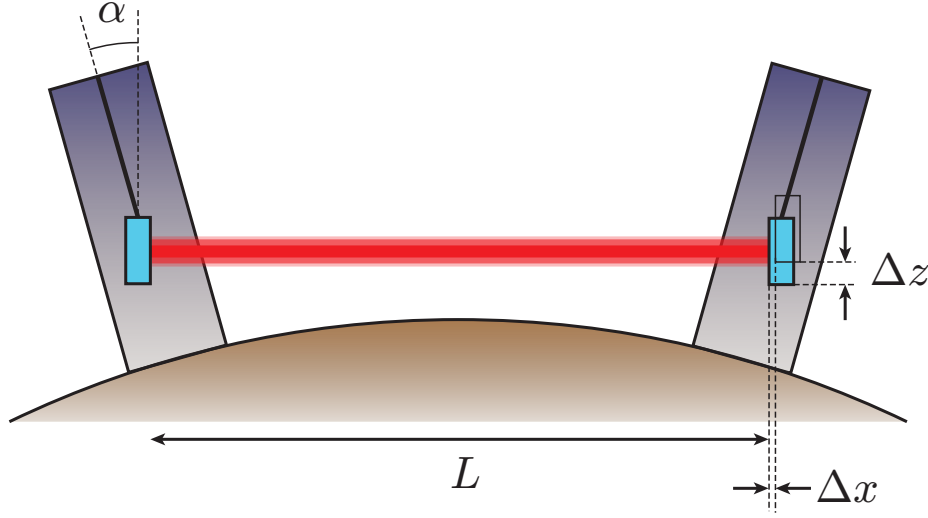
Fig. 2.6. Vertical-to-longitudinal coupling of the mirror motion due to the Earth's curvature.

from local vertical motion of the mirror to global longitudinal variation of the optical cavity, as depicted in fig. 2.6. The impact of coupling, $\Delta x = \alpha \, \Delta z$, is related by the factor α, which is associated with the separation distance of the mirrors L and the local radius of the Earth $R_\oplus$, through the relation $\alpha = L/2R_\oplus$. In the case of a 3 km separation, one can estimate the typical vertical-to-longitudinal coupling as $\alpha \sim 2.4 \times 10^{-4}$. To achieve a displacement noise of about 10^{-20} m in the observational frequency band under the isotropic seismic disturbance, we must also recognize the necessity of the vibration isolation in the vertical direction.

2.4 Anti-spring mechanisms

As mentioned in section 2.2, seismic attenuation performance in a given frequency region (e.g., 10–100 Hz for a terrestrial gravitational wave detector) can be improved by lowering the resonant frequencies of the mechanical oscillators. While using multiplied stages of pendulum, implementation of mechanical oscillators with lower-frequency resonance in a practical dimension is also needed to construct a gravitational wave detector.

This section describes two types of harmonic oscillators implemented in the KAGRA suspension systems, an inverted pendulum and a geometric anti-spring filter. Their design incorporates an anti-spring effect that can reduce the effective spring constant of the oscillators, resulting low resonant frequencies while maintaining compact dimensions. An anti-spring is a system that incorporates a force that pushes it away from its equilibrium point once it experiences a displacement. If an anti-spring system is combined with a positive spring constant inherent to most of the mechanical oscillator, the overall stiffness of the system can be tuned to nearly zero.

2.4.1   Inverted pendulum (IP)

An inverted pendulum (IP) is a system in which the center of mass of its oscillator is positioned higher than the supporting point on the ground. Unlike an inverted pendulum on a cart in the context of stabilization problems of control theory, we fixed the foot of the IP with a flexure joint onto the ground to obtain a positive angular stiffness k_θ so that the system acquired quasi-stability. By tuning the amount of weight loaded on the top of the IP, it was possible to realize an ultimate low resonant frequency of $\lesssim 100$ mHz in horizontal motion.
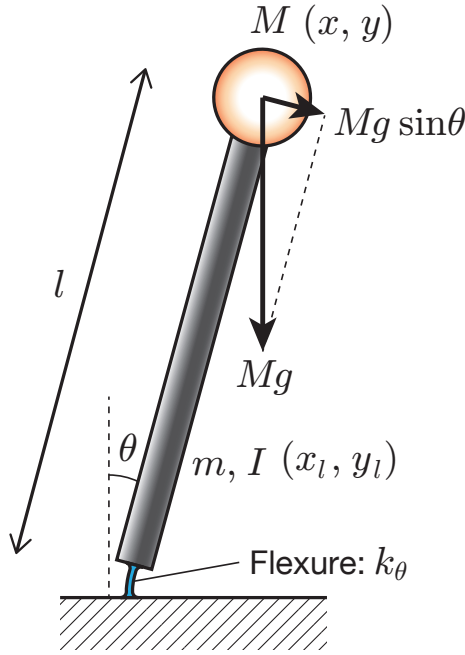
Fig. 2.7. Working principle of an inverted pendulum

Working principle

The dynamics shows how the anti-spring effect acts on the intrinsic stiffness of the IP. Given an IP depicted in fig. 2.7 with physical properties that are summarized in table 2.1, the Lagrangian L of the system is determined as

$$L = K - U, \tag{2.4}$$

$$K = \frac{1}{2}M\left(\dot{x}^2 + \dot{z}^2\right) + \frac{1}{2}m\left(\dot{x}_l^2 + \dot{z}_l^2\right) + \frac{1}{2}I\ddot{\theta}, \tag{2.5}$$

$$U = Mgz + mgz_l + \frac{1}{2}k_\theta\theta^2, \tag{2.6}$$

Table 2.1. Denotations of the inverted pendulum model

M	mass of the payload
l	length of the IP leg
m	mass of the IP leg
I	moment of inertia about the center of mass of the IP leg
(x, z)	position of the payload
(x_l, z_l)	position of the IP leg
(x_0, z_0)	position of the fixed point of the flexure on the ground
θ	angle of the IP leg with respect to the vertical axis
k_θ	rotational spring constant of the flexure

where K and U represent the kinetic and the potential energy, respectively. Under the geometrical constraints,

$$
\begin{aligned}
x_l &= \frac{1}{2}(x + x_0) \\
z_l &= \frac{1}{2}z \\
x &= l \sin \theta + x_0 \\
z &= l \cos \theta
\end{aligned}
\tag{2.7}
$$

the kinetic energy and the potential energy can be simplified as

$$
K = \frac{1}{2}M\dot{x}^2 + \frac{1}{8}(\dot{x} + \dot{x}_0)^2 + \frac{1}{2}I\left(\frac{\dot{x} - \dot{x}_0}{l}\right)^2 ,
\tag{2.8}
$$

$$
U = Mgl \cos\left(\frac{x - x_0}{l}\right) + \frac{mgl}{2} \cos\left(\frac{x - x_0}{l}\right) + \frac{1}{2}k_\theta \left(\frac{x - x_0}{l}\right)^2 .
\tag{2.9}
$$

The Euler-Lagrange equation of motion is therefore, with the 1st-order approximation,

$$
\frac{\mathrm{d}}{\mathrm{d}t}\frac{\partial K}{\partial \dot{x}} = \frac{\partial U}{\partial x} ,
\tag{2.10}
$$

$$
\left(M + \frac{m}{4} + \frac{I}{l^2}\right)\ddot{x} + \left(\frac{m}{4} - \frac{I}{l^2}\right)\ddot{x}_0 = -\left[\frac{k_\theta}{l^2} - \left(M + \frac{m}{2}\right)\frac{g}{l}\right](x - x_0) .
\tag{2.11}
$$

One can regard (2.11) as the equation of motion of a harmonic oscillator with an effective spring constant k_{eff},

$$
k_{\text{eff}} = \frac{k_\theta}{l^2} - \left(M + \frac{m}{2}\right)\frac{g}{l} .
\tag{2.12}
$$

The first term of k_{eff} represents the elastic restoring force of the flexure. In contrast, the repulsive force appears in the second term and acts to reduce the effective stiffness of the harmonic oscillation. This force is therefore called the *gravitational anti-spring force*. As the
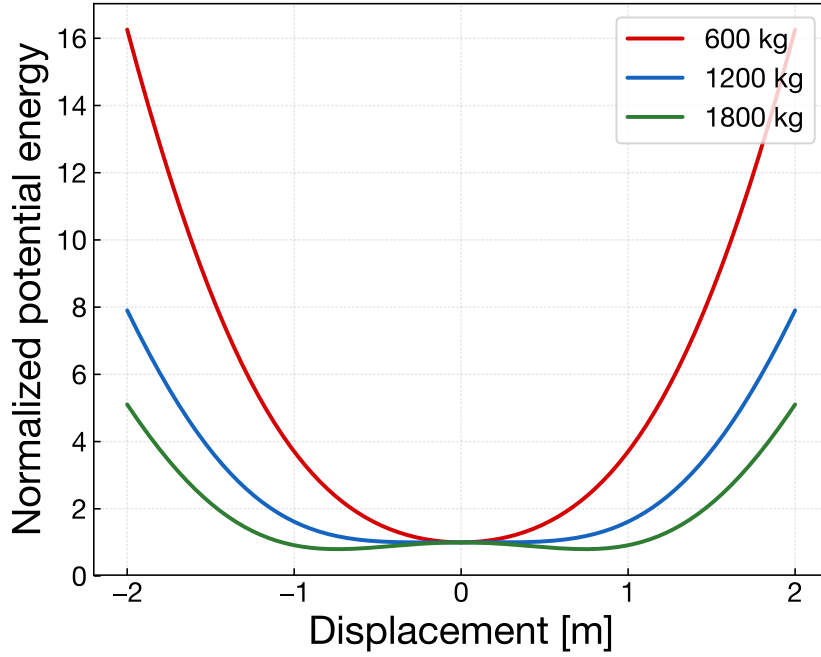
Fig. 2.8. Potential energy of the IP with different loads

gravitational anti-spring force is proportional to the mass of the payload and the IP leg, the effective spring constant can be tuned by changing the load on the IP.

However, if the restoring force and repulsive force are perfectly cancelled, the system is no longer oscillatory with a single equilibrium point. The potential energy of the IP with various loads is plotted in Fig 2.8. When the IP is not sufficiently loaded, its potential energy can be approximated to a parabolic curve dominated by the third term of (2.9). As the weight on the IP increases, the potential curve gets flattened around its equilibrium point of $x = x_0$. Beyond the critical loading, the first term of (2.9) increases and the system shows bistability, i.e., it has two equilibrium points. For stable operation of the vertically-standing IP, the load must be small enough to keep the effective spring constant positive.

In a stable condition where the IP has only one equilibrium point, from (2.12), the resonant frequency of the IP is determined as

$$f_0 = \frac{1}{2\pi} \sqrt{\frac{k_{\text{eff}}}{M + \frac{m}{4} + \frac{I}{l^2}}} \ . \tag{2.13}$$

With the set of parameters shown in the table, the dependence of the resonant frequency on the mass of the load is presented in Fig. 2.9. When increasing the load on the IP, the resonant frequency gradually decreases and then drastically drops, which makes the system unstable.
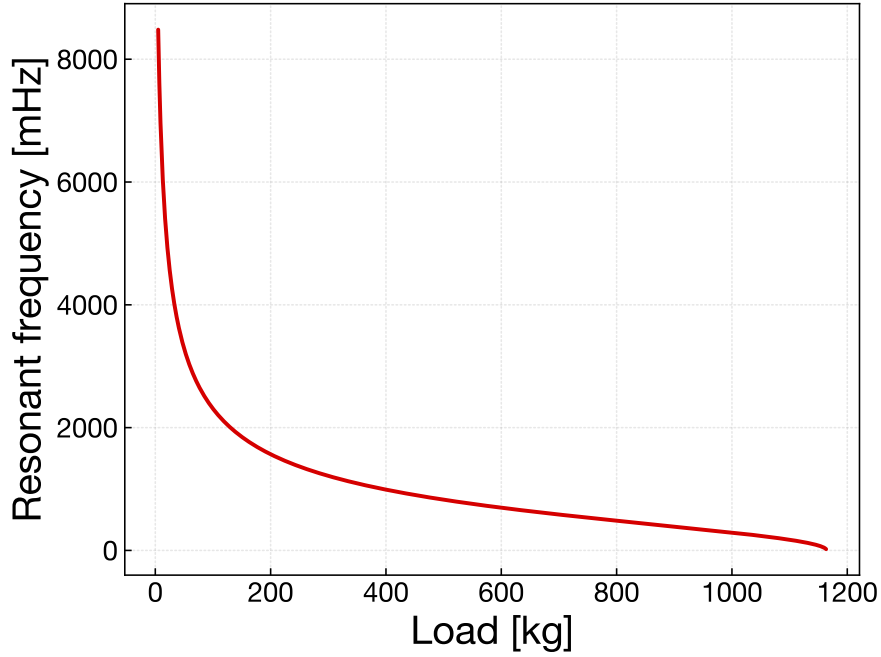
Fig. 2.9. Change in the resonant frequency of the IP with respect to the mass of the load.

Attenuation performance

The transfer function from the ground motion to the payload is obtained by solving eq. (2.11) in the frequency domain.

$$H_{\text{IP}}(\omega) = \frac{\tilde{x}}{\tilde{x}_0} = \frac{k_{\text{eff}} + \left(\frac{m}{4} - \frac{I}{l^2}\right)\omega^2}{k_{\text{eff}} - \left(M + \frac{m}{4} + \frac{I}{l^2}\right)\omega^2}$$
$$= \frac{A + B\omega^2}{A - \omega^2}, \tag{2.14}$$

where

$$A = \frac{k_{\text{eff}}}{M + \frac{m}{4} + \frac{I}{l^2}}, \quad B = \frac{\frac{m}{4} - \frac{I}{l^2}}{M + \frac{m}{4} + \frac{I}{l^2}}. \tag{2.15}$$

Seeing the plotted curve of this transfer function in Figure 2.10, the IP behaves similarly to an ideal harmonic oscillator up to a certain frequency above the resonance. However, the attenuation performance of the IP saturates at a certain level owing to the coefficient B that appears in eq. (2.14).

This saturation is due to a residual momentum transfer from the leg to the payload caused by the so-called *center of percussion effect* [14, 15]. When an impulsive force is applied onto a rigid body, the blow accelerates the body both in translation of its center of mass and in rotation around its center of mass, as illustrated in fig. 2.11. At this moment there exists a point where the translation and rotation cancel each other out and the net initial velocity
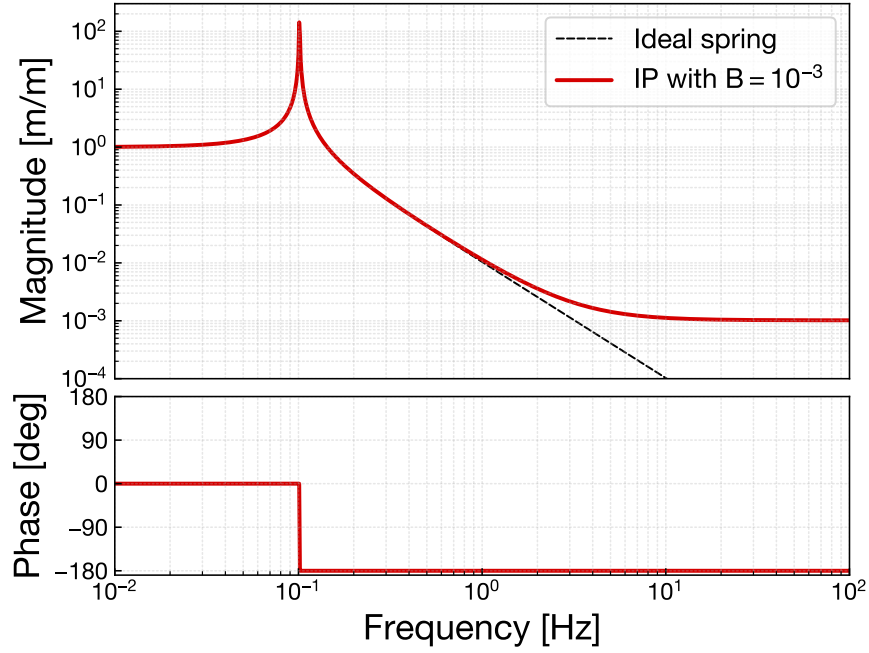
Fig. 2.10. Transfer function from the ground motion to the payload of the IP. That of an ideal harmonic oscillator is also plotted for comparison.

becomes zero. This point is called the *pivot point* or in other fields, the *sweet spot*, which we can regard as the momentary center of rotation for the impulse. The location of the pivot point is determined by the mass distribution of the body and is not necessarily within the boundary of the body.

The pivot point has a complementary point on the opposite side of the center of mass, the *center of percussion* (CoP). As mentioned before, a perpendicular impulse applied at a CoP will produce no reactive force at its corresponding pivot point. The position of the CoP and pivot point from a body's center of mass is tied with the following equation.

$$r_\mathrm{f}\, r_\mathrm{p} = \frac{I_\mathrm{body}}{M_\mathrm{body}} \tag{2.16}$$

Here, r_f and r_p are the radii of the CoP and that of the pivot point (see fig. 2.11), and M_body and I_body are the mass and moment of inertia of the body, respectively. This relationship indicates that the CoP and pivot point will swap positions when the impulse is applied on the other side of the center of mass.

In the case of the IP legs, they have mechanical constraints, as one end is connected to the payload and the other is fixed to the ground via the flexure; thus, they cannot rotate freely. This constraint is substantial at low frequencies so that the IP behaves as expected, i.e., like a harmonic oscillator with a low-frequency resonance. However, the constraint becomes fainter at higher frequencies which allows the IP leg to perform free rotation around its pivot point.
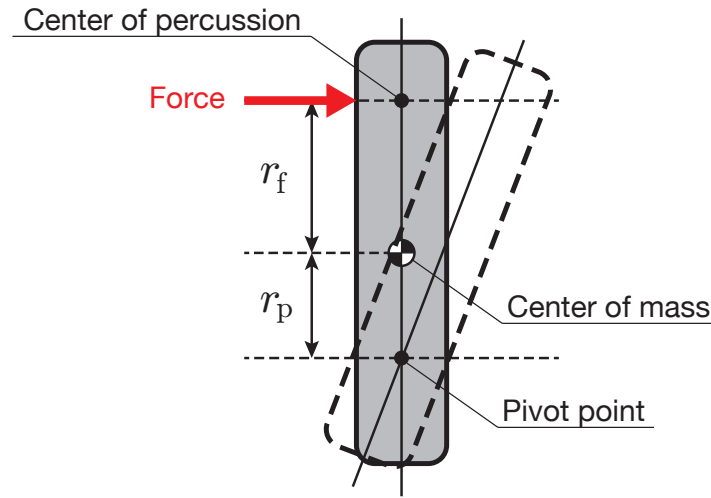
Fig. 2.11. Illustration of the center of percussion. When a rigid body receives an impulsive force that is not aligned to its center of mass, the body is subject to momentary acceleration both in translation of its center of mass and in rotation around its center of mass. There exists a point *pivot point*, where the translation and rotation cancel each other out and the net initial velocity becomes zero. The *center of percussion* is a complementary point for the pivot point located at the other side of the center of mass. In other words, the center of percussion is the point where a perpendicular impulse does not produce any reactive force at the given pivot point.

In order to reduce the residual momentum transfer from the leg to the payload, one needs to let the position of the center of percussion corresponding to the top end of the IP leg coincide with the foot of the flexure where the external force (ground motion) is applied. This allows the IP leg to rotate around its top end as the pivot point without exerting a force on the payload.

To adjust the position of the CoP, a counterweight may be added to the bottom of the IP leg as its position depends on the mass distribution of the body. Figure 2.13 shows that a counterweight improves the saturation level of the vibration isolation ratio. Typically, adjusted counterweights can mitigate the saturation level by 1–2 orders of magnitude in practice. For instance, the IP of the HAM-SAS developed for advanced LIGO achieved $\sim 10^{-3}$ attenuation without counterweights and $\sim 10^{-5} - 10^{-4}$ with them with an aluminum hollow leg of about 0.2 kg. The presence of a notch followed by the plateau depends on which direction (upper or lower) the position of the pivot point is offset from the target point.
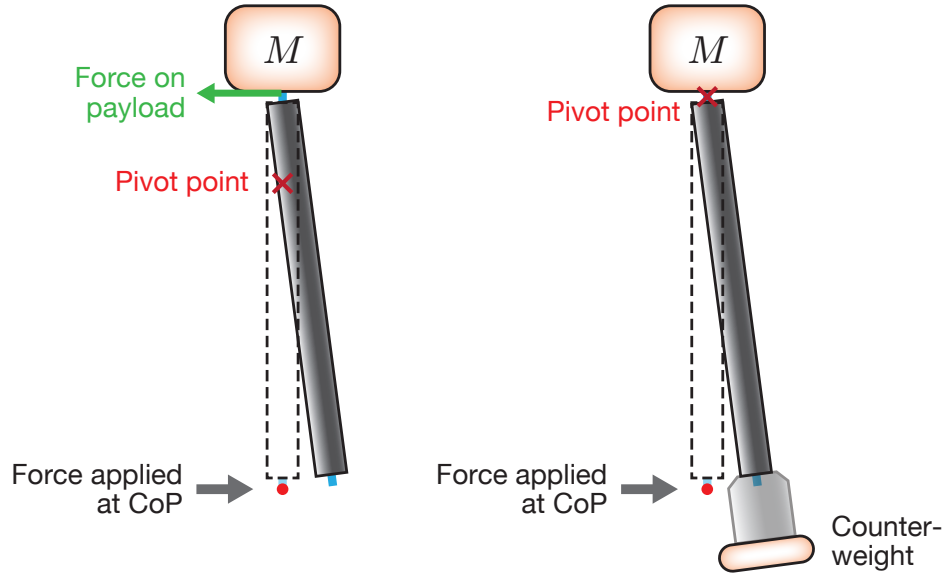
Fig. 2.12. Illustration of the effect of a counterweight on the pivot point. In general, the pivot point complementary to the center of percussion located at the bottom flexure does not coincide with the connecting part of the payload. Adding a counterweight at the bottom of the leg can move the pivot point to the top connecting part so that the IP leg can rotate without exerting a force on the payload, thereby improving its isolation performance from the ground.

2.4.2 Geometric Anti-Spring (GAS) filter

A getometric anti-spring (GAS) filter is a mechanical oscillator that uses of radially converging cantilever blades to obtain a low resonant frequency in the vertical direction under a heavy load [16, 17]. The quasi-triangular cantilever blades are connected at their vertices, which compresses them. The compression produces a repulsive force following vertical displacement that results in the formation of stiffness that counters the intrinsic stiffness of the cantilever blades. In the situation where the load and compression are tuned appropriately, the GAS filter adequates the low-frequency vertical resonance with typically ~ 0.3 Hz

Working principle

Here, brief dynamics of the GAS filter are presented to understand implementation of its anti-spring mechanism. The behavior of a GAS filter is modeled as a system in which a payload is supported by a normal vertical spring and a set of horizontal springs that are compressed against each other, as illustrated in fig. 2.14. Owing to the radially symmetric configuration of the cantilever blades, the horizontal components of the reaction forces that counter the compression vanish, and thereby, the keystone is constrained to move only in the
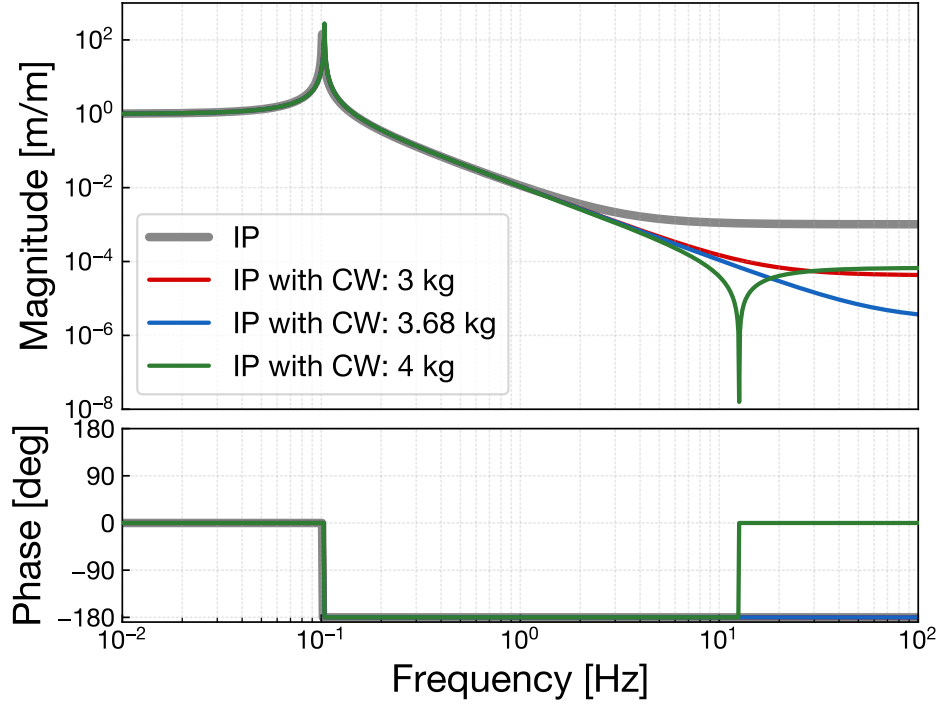
Fig. 2.13. Vibration isolation ratio of the IP with different loads of the counterweight (CW). The saturation level can be improved by 1–2 orders of magnitude with the counterweights. The presence of a notch at the frequency of $\sim 12\text{Hz}$ depends on which direction (upper or lower) the pivot point is offset from the target position.

vertical direction.

The keystone of the GAS filter stays at a working point $z = z_{\text{eq}}$, where the constant load Mg and the static force of the vertical spring are balanced, and the conceptual horizontal springs become orthogonal to the z-axis ($\theta = 0$) and experience maximum compression. Here g denotes gravitational acceleration and M the mass of the payload. When the keystone is displaced from the equilibrium position, its equation of motion is described as

$$M\ddot{z} = -k_z(z - z_{\text{eq}}) - k_x(l_x - l_{x0})\sin\theta\,, \tag{2.17}$$

where k_z and k_x are the spring constant of the vertical and horizontal spring, l_x and l_{x0} are the actual length and the natural length of the horizontal spring, respectively. In addition, the working point can be written as $z_{\text{eq}} = Mg/k_z$ owing to the balance condition. If we assumed that only the small motions around the working point, eq. (2.17) can be linearized as

$$M\ddot{z} = -\left[k_z - \left(\frac{l_{x0}}{x_0} - 1\right)k_x\right](z - z_{\text{eq}})\,, \tag{2.18}$$

where x_0 denotes the length of the horizontal spring at the equilibrium. From this equation,
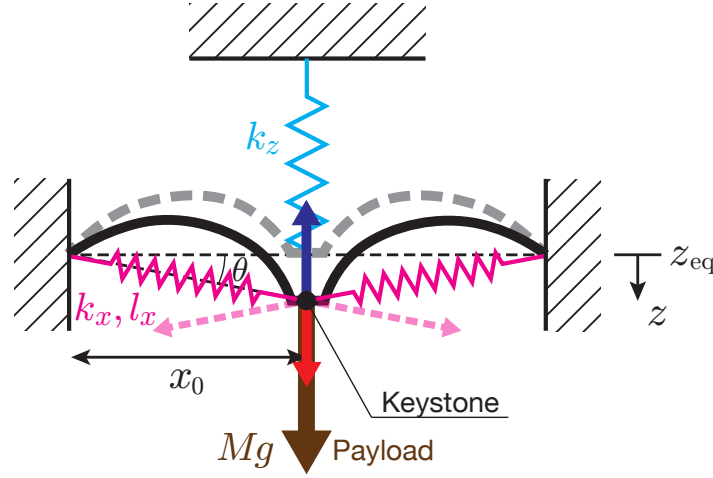
Fig. 2.14. Conceptual representation of a geometric anti-spring (GAS) filter. A set of cantilever blades are compressed supporting the keystone subject to the payload. The system can be modeled with a normal vertical spring (light blue) and a combination of compressed horizontal springs (pink). When the keystone is displaced, the horizontal components of the reaction forces against the compression cancel each other out (faint dotted pink arrow) and the net repulsive force along the z-axis (red arrow) remains. The resultant stiffness of the keystone is the sum of contributions from the intrinsic vertical spring and the net horizontal springs.

we can obtain the effective spring constant of the GAS filter as

$$k_{\text{eff}} \sim k_z - \left(\frac{l_{x0}}{x_0} - 1 \right) k_x \, . \tag{2.19}$$

This formula indicates that the effective spring constant decreases when the horizontal springs are under compression ($x_0 < l_{x0}$). The second term proportional to k_x corresponds to the repulsive force along the z-axis, which mitigates the intrinsic stiffness k_z. The geometric constraint on the keystone or the tip of the cantilever blades enables stiffness cancellation in vertical motions and therefore the mechanism is called *geometric anti-spring* effect. As this anti-spring mechanism is a local effect around the working point, the capability of the system to support a heavy payload is maintained.

Attenuation performance

The transfer function from the reference frame to the keystone can be written in the same form as that of the IP in eq. (2.14). Owing to the CoP effect, the seismic attenuation performance of the GAS filter saturates at high frequencies, which is typically limited to $\sim 10^{-3}$ [18]. It can be improved by mounting a compensation wand in parallel to the blades

with a couterweight. With a sufficient counterweight adjusting the position of the CoP so that it corresponds to the fixing radius of the blades, the saturation level can be mitigated to about 10^{-4}.

Thermal stability

Soft support of the GAS in the vertical direction is provided by the compressed blade springs with their elastic deformation. Thus, the strength of its repulsive force is sensitive to the change in the physical properties of the blade. In particular, the temperature dependency of the Young modulus can cause the working points of the keystone to drift. The amount of the change in the keystone's working point becomes larger when the resonant frequency of the GAS is tuned to be lower, which relationship can be typically evaluated as [19],

$$\frac{\Delta z}{\Delta T} = \frac{g}{E\omega_0^2}\frac{\partial E}{\partial T}$$

$$= 0.69 \text{ [mm/K]} \left(\frac{0.33 \text{ Hz}}{\omega_0/2\pi}\right)^2 \left(\frac{\frac{1}{E}\frac{\partial E}{\partial T}}{3.0 \times 10^{-4} \text{ K}^{-1}}\right) , \tag{2.20}$$

where ΔT is the temperature change, E is the Young modulus of the blade material, ω_0 is the angular resonant frequency of the GAS. This indicates that a non-negligible change in the height (in the order of millimeters) of the optics will take place at the bottom when the suspension has plural stages of the GAS filter. For this reason, the environmental temperature of the instruments has to be kept sufficiently stable.

2.5 Damping

Mechanical filters can isolate suspended masses from the seismic motion in a high frequency region. Furthermore, they carry the vibration directly to the masses at low frequencies or rather amplify the magnitude of the masses' fluctuation at the resonant frequencies. The amplification at these mechanical resonances often takes place out of the observational band, and thus does no immediate harm to the sensitivity of the interferometer. However, as the interferometer has to keep its interfered light in a specific condition with a narrow-ranged control, it cannot be operated with the largely-swinging mirrors with which the control can no longer survive. Therefore, the effective fluctuation of the mirrors needs to be reduced regardless of the frequency region.

The effective amplitude of the mirror fluctuation can be evaluated as the root-mean-square (RMS) amplitude. The RMS amplitude of a time-varying physical value $x(t)$ is defined as

$$x_{\text{RMS}} \equiv \sqrt{\int_a^b S_x(\omega)\, \mathrm{d}\omega} , \tag{2.21}$$

where $S_x(\omega)$ is the power spectral density of x. The interval of the integral is commonly set to $0 \sim \infty$ or is sometimes set to a frequency region of interest. The RMS amplitude of the seismic motion is typically in the order of microns at the ground surface and submicrons for underground regions. In the case of suspension systems that often have mechanical resonances below 1 Hz, the main contribution to the RMS amplitude comes from the peaks in the low frequency band ($\lesssim 1$ Hz) where driving disturbances at the resonant peaks are not sufficiently attenuated.

For the reasons above, implementation of a damping mechanism is necessary for the suspension systems in gravitational wave telescopes. Damping in a physical system means intentionally introducing dissipation processes into the system to produce resistive forces on the oscillating object. We install the damping mechanism on the suspension system not only to reduce the RMS amplitude but also to increase the robustness of the system against unwanted sudden disturbances such as earthquakes and falsely-injected actuation forces. If mechanical resonances with large amplitudes due to immediate disturbance remain for a long time, the interferometer cannot resume its operation, which indicates that the duty cycle or duration of its observation will be lost. Thus, it is essential to reduce the decay time of the mechanical resonances for the operationability of the interferometer.

A damping effect can be implemented on the suspension system in two ways: passive damping and active damping. In the following subsections, the brief explanations of these damping techniques are presented.

2.5.1   Passive damping

Passive damping introduces a viscous element into the system which generates a breaking force proportional to the velocity of the oscillator. If we consider a mass-spring-damper system, like the one illustrated in the left panel of fig. 2.15, the equation of motion of the oscillator is

$$M\ddot{x} + \gamma(\dot{x} - \dot{x}_0) + k(x - x_0) = 0 \,, \tag{2.22}$$

where γ is the damping coefficient. Bt interpreting this equation in the frequency domain through Fourier transformation, we can derive the transfer function from the ground displacement to the mass displacement:

$$H(\omega) \equiv \frac{\tilde{x}(\omega)}{\tilde{x}_0(\omega)} = \frac{1 + 2\mathrm{i}\zeta\dfrac{\omega}{\omega_0}}{1 + 2\mathrm{i}\zeta\dfrac{\omega}{\omega_0} - \left(\dfrac{\omega}{\omega_0}\right)^2} \,, \tag{2.23}$$

where the parameter ζ is called the *damping ratio*, which is determined by $\zeta = \gamma/2M\omega_0$. The strength of the damping is also sometimes referred to as the quality factor of the resonance; it is defined as $Q \equiv 1/2\zeta$.
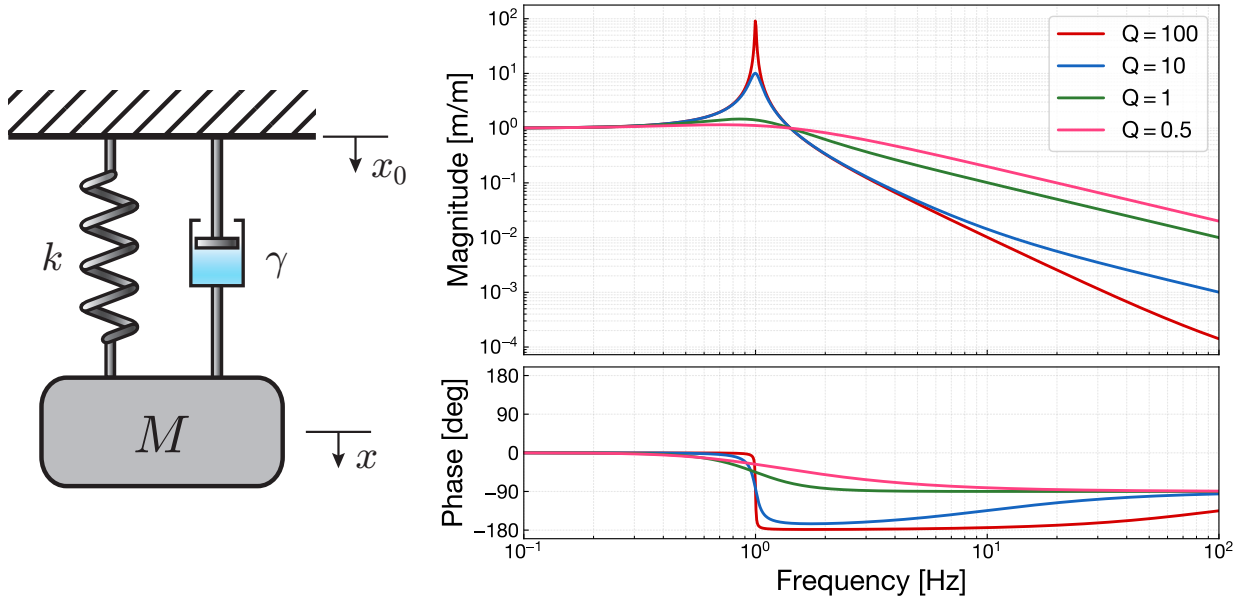
Fig. 2.15. An illustration of the mass-spring-damper system (*left*), and its vibration isolation ratio with various damping strength parameterized by the quality factor Q (*right*). The component of the viscous damping is represented as a dashpot.

The vibration isolation ratios of the mass-spring-damper system obtained by varying the strength of the viscous damping denoted as the quality factors Q is plotted in the right panel of fig. 2.15. As a stronger damping is applied to the suspended mass, the height of the resonant peak reduces, which is approximately equivalent to Q in the case of $Q \gg 1$. On the other hand, the magnitude of the attenuation factor rolls off with the proportionality of f^{-1} in high frequency regions above Qf_0, unlike that of the undamped system with a f^{-2} roll off. Therefore, the vibration isolation performance of the viscously-damped system degrades in the high frequency region.

The effect of the damping can be seen also in the impulse responses of the mass displacement. Figure 2.16 shows the responses of the viscously-damped system when an external impulsive force is applied to the mass, varying and the strength of the damping effect is varied. The system with small damping exhibits a sinusoidal waveform with slightly decaying amplitude. As the damping effect becomes prominent, the decay of the amplitude quickly comes into effect. The speed of the decay is characterized by the exponential decay time τ_e in which the oscillation amplitude decreases by a factor of $1/e$, which is written as,

$$\tau_e \equiv \frac{1}{\zeta\omega_0} = \frac{2Q}{\omega_0} \, . \tag{2.24}$$

The condition with a damping ratio ζ of one is called *critical damping*, where the oscillatory behavior of the impulse response turns into a non-oscillatory transient showing the shortest decay time. Then, if the damping ratio is larger than one, the system is robust to the external

force but has a longer decay time since the excess of viscosity resists restoration of the system to its original position.
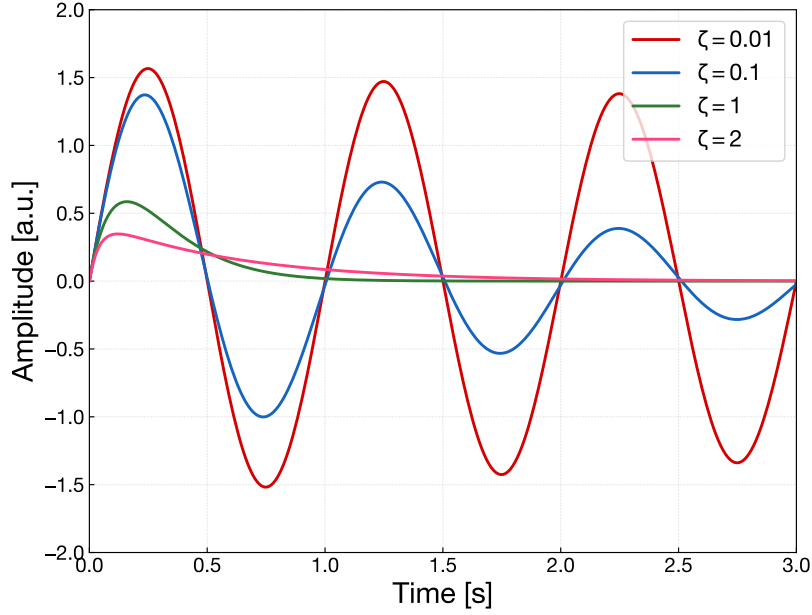
Fig. 2.16. Responses of the viscously damped system with various damping ratios driven by an impulsive force applied to the suspended mass.

The degradation of the vibration isolation performance in the viscously damped system can be mitigated by isolating the damper with some mechanical filters, as illustrated in fig. 2.17. This technique is called *flexible damping*. Although, in a system with flexible damping, the transfer function from the ground motion to the mass displacement has an additional resonant peak owing to the spring for the damper, the roll off in the high frequency region maintains a f^{-2} proportionality, like a system with no damping mechanism.

One simple way to implement the passive damping mechanism is by using an eddy current damper [20]. One unit of the eddy current damper consists of a set of permanent magnets and a conductive object that are placed so that they face each other. When the conductive object moves in the magnetic field formed by the permanent magnets, eddy currents are generated inside the conductive object resisting the change in the magnetic field, and thus they produce a breaking force of the moving object. The strength of the eddy current damping is formulated as the following relationship,

$$\gamma_{\text{eddy}} = A\sigma B \frac{\partial B}{\partial x} \, , \tag{2.25}$$

where B is the magnetic field of the permanent magnets, σ is the electrical conductivity of the facing object, and A is a geometrical factor determined by the area of the conductor. In qualitative words, stronger magnets and higher conductivity surface can achieve larger
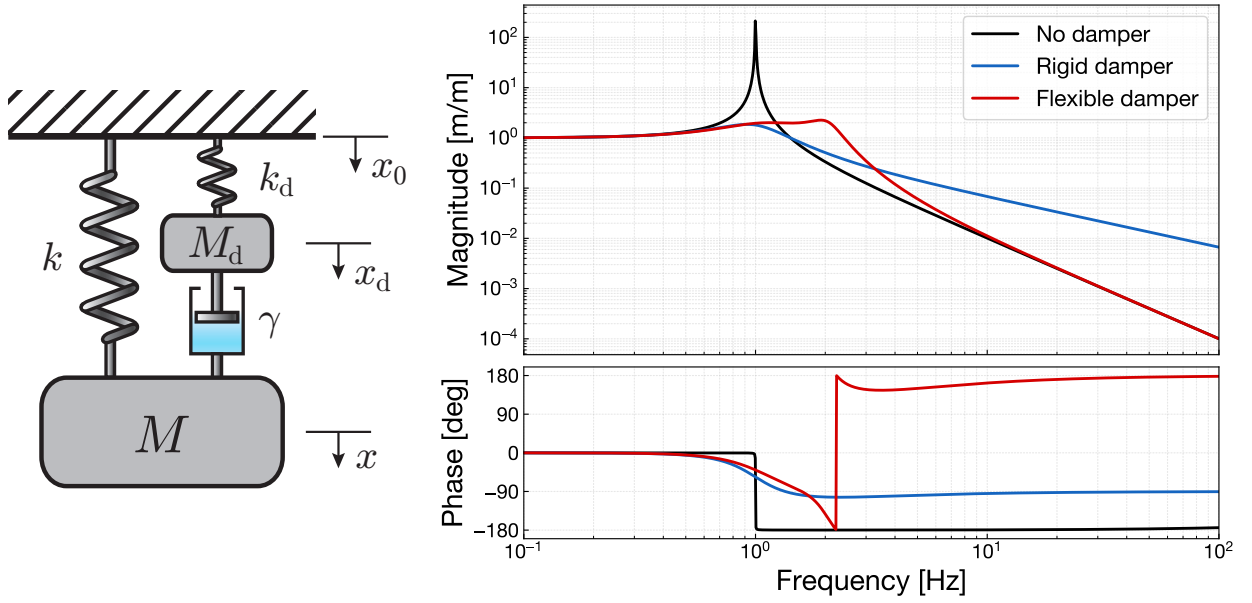
Fig. 2.17. An illustration of the suspended-mass system with flexible damping mechanism (*left*), and its vibration isolation ratio compared with those in the cases of no damper and rigid damping (*right*).

damping effect with an eddy current damper. The eddy current damper is often used in the suspension system because of its vacuum compatibility and the absence of hysteretic noise owing to its noncontacting functionality. Nevertheless, the disadvantage of the eddy current damper is there is a risk of introducing additional magnetic noise onto the test masses, which also have permanent magnets for control actuation. This disadvantages can be mitigated by separating the damper from the test mass, for example, by placing the damper on one of the upper stages.

2.6   Active vibration isolation

While the passive vibration isolation utilizes intrinsic low-pass characteristics of mechanical oscillators, the seismic attenuation is valid only at high frequencies above its resonant frequency. If one aims to isolate objects in a low frequency region, such as the microseismic disturbance around 0.2–0.5 Hz, the passive isolation scheme feels awkward if negative-stiffness components are not used. On the other hand, active vibration isolation which implements sensors, actuators, and controllers can effectively reduce the seismic transmissivity to the target object in an arbitrary frequency band in principle.

The basic concept of the active vibration isolation is a feedback control with an inertial sensor mounted on the target object supported with spring-like elements. The inertial sensor monitors the absolute motion of the object with respect to the inertial frame. The signal from

the inertial sensor is processed via the servo controller and then sent to the actuator in order to generate a motion-canceling force on the suspended body. This method can be effective as long as the inertial sensor has enough sensitivity to detect the motion of the target object without being limited by the sensor noise in the frequency region of interest. However, in practice, because of the AC-coupled feature of the general inertial sensors, the active isolation requires supplementary sensors and control loops such as relative displacement sensors for low-frequency stabilization and witness sensors placed on the ground for feedforward control and sensor correction.

The active vibration isolation is implemented on the inertial seismic isolators in advanced LIGO suspensions. A detailed discussion on the active isolation strategy and instrumentation is available in [21].

Chapter 3

KAGRA Type-A Suspension

In this chapter, we describe the design and setup of Type-A suspension system, the suspension system for KAGRA test masses that is characterized in this study. Section 3.1 briefly mentions the overall configuration of the KAGRA interferometer. In section 3.2, we review the suspension systems used for vibration isolation in KAGRA. From section 3.3 the detailed design of the Type-A suspension, which contains mechanical components, electric devices such as sensors and actuators, and control systems, is described. Although this chapter focuses on describing the Type-A suspension, most of the components enumerated above are shared with other types of suspension systems. Thus, the Type-A suspension and all other suspension systems in KAGRA are the topics of this chapter.

3.1 Overview of KAGRA interferometer

KAGRA is a power- and signal-recycling (also reffered to as *dual recycling*) Fabry-Perot Michelson interferometer with an arm length of 3 km. At the time of writing this thesis, KAGRA was undergoing a major upgrade campaign where suspension systems for core optics were being installed.In April–May 2018, KAGRA underwent a test operation with simplified Michelson interferometer formed by a cryogenic test mass. After the major upgrade in 2019, KAGRA will participate in joint observation with Advanced LIGO and Advanced Virgo called *observation run 3* or O3 in short, with incomplete sensitivity corresponding to a few (tens of) megaparsec of the inspiral range. KAGRA will start observations with its full sensitivity in the 2020s.

3.1.1 Conceptual design

The sensitivity of KAGRA is shown in fig. 3.1, which is generated from the design parameters summarized in table 3.1. There are two types of operational modes in KAGRA, broadband resonant sideband extraction (BRSE) and detuned resonant sideband extraction
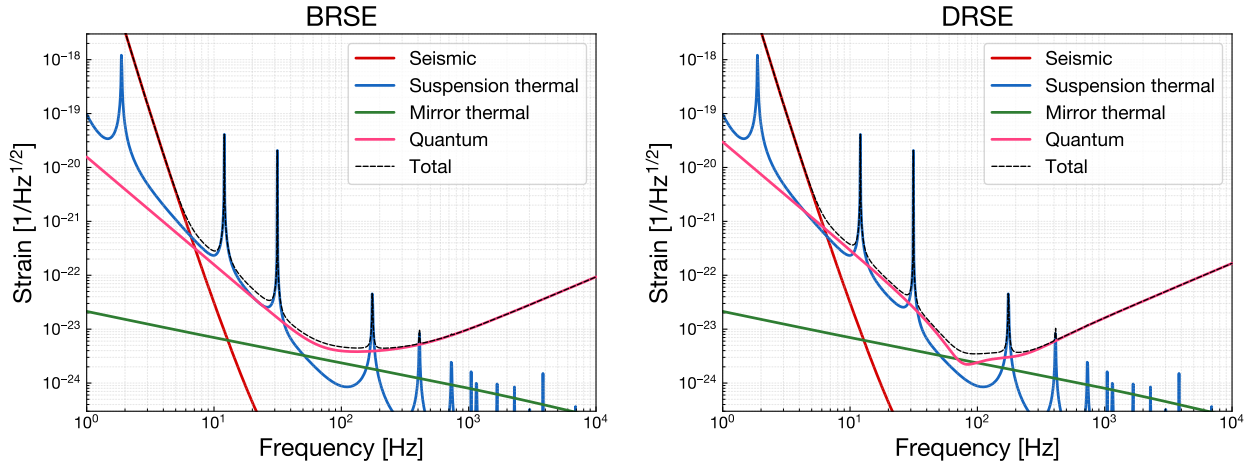
Fig. 3.1. Sensitivity curves and breakdowns of noise contributions in two operational modes of the KAGRA interferometer. The *left* panel shows the broadband RSE (BRSE) configuration, while the *right* panel shows the detuned RSE (DRSE) configuration.

(DRSE). In the BRSE operation, there is additionally an option of homodyne detection. We can switch the operational mode of the interferometer depending on which purpose we give priority to.

The sensitivity curve is designed to be dominated by the fundamental quantum noises, the shot noise at high frequencies, and the radiation pressure noise at low frequencies[22]. Although some peaks from suspension thermal noise exceed the quantum noises, they are not an issue. In the most sensitive frequency region, the mirror thermal noise which originates from the thermal dissipation of reflective coating layers, shows predominance even with cryogenic temperature. The sensitivity below 10 Hz is dominated by seismic noise and gravity-gradient noise.

In the design of KAGRA, we introduced two unique features to improve its sensitivity: the use of an underground environment and cryogenic test masses. These are some of the advanced options to be implemented in the next generation gravitational wave telescopes. Therefore, KAGRA has an aspect of a laboratory to demonstrate the feasibility and usefulness of these techniques.

Underground environment

The underground environment of the Kamioka mine is one of the unique features among the 2nd-generation gravitational wave observatories. The central station of KAGRA is situated at 36.41°N and 137.31°E inside the 1300-meter-high mountain Ikenoyama, where other observatories of high-energy physics such as Super-Kamiokande and XMASS are also constructed. Even though the KAGRA tunnel occupies an L-shaped space 3 km on a side, the ends of the arms are close to the foot of the mountain, and the end test masses are at least

Table 3.1. Main design parameters for KAGRA interferometer.

Parameter	Design value
Baseline length	3 km
Laser wavelength	1064 nm
Laser power at BS	674 W
Material of test mass substrate	Sapphire
Material of test mass coating	Silica/Tantala
Test mass diameter	22 cm
Test mass thickness	15 cm
Test mass weight	22.8 kg
Temperature of test mass	22 K
Suspension wire for test mass	Sapphire
Inspiral range (BRSE)	128 Mpc
Inspiral range (DRSE)	153 Mpc

200 m below the ground surface [23].

The first explicit advantage of the underground environment is tranquility of the seismic vibration as described in sec. 2.1. This low seismic vibration helps us to achieve the required displacement noise in the observation band and stable operation of the interferometer.

Before the location of KAGRA was selected, a joint research project of the Disaster Prevention Research Institute and Cryogenic Laser Interferometer Observatory (CLIO) performed a long period observation of the seismic vibration in the Kamioka mine [24]. T. Sekiguchi's analysis of 1.5-year data (2009.09–2011.02) from the measurement formulated the seismic noise models plotted in fig. 3.2. The red, green, and blue curves represent seismic noise spectra at the 90th (high), 50th (mean), and 10th (low) percentile levels respectively. The spectra below 1 Hz are the measured data in the 1.5-year observation, while those above 1 Hz are the extrapolations of the measurement results assuming proportionality to f^{-2}. As the seismometer CMG-T3 used in the measurement has a worse noise level above 1 Hz, the f^{-2}-proportionality at higher frequencies is confirmed through another measurement by M. Beker who uses a different seismometer, Trillium 240, at the CLIO site [25]. Note that the spectra below 50 mHz are also contaminated by the sensor noise of the CMG-T3.

The microseismic peak around 0.2 Hz shows a large variation in magnitude as the amplitude depends on the oceanic activity and thus on the weather condition. The RMS displacement of the seismic motion (cumulatively integrated down to 10^{-2} Hz) varies in the range of 0.08–0.5 μm with the 10–90 percentile range. In the following discussions, we take the high noise model in fig. 3.2 as the seismic vibration spectrum for a conservative estimate.

Figure 3.2 indicates that the spontaneous displacement noise in the Kamioka mine is
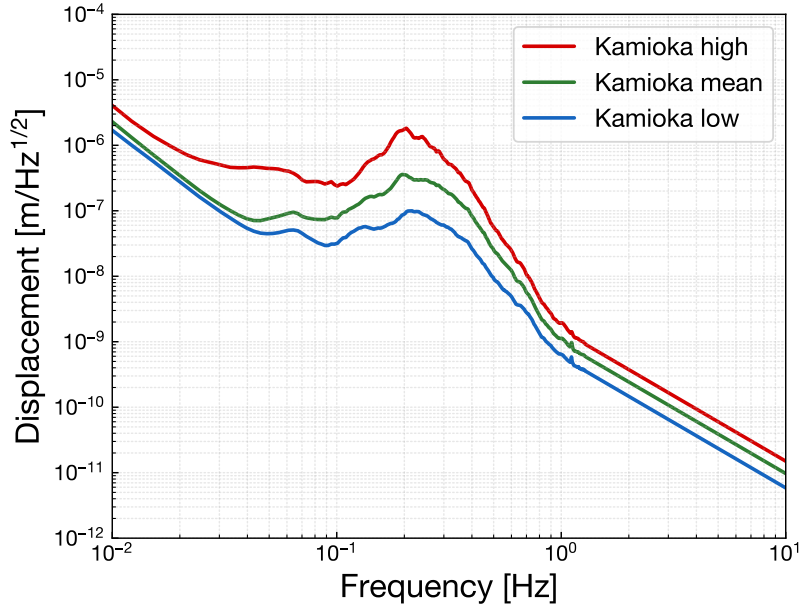
Fig. 3.2.   Seismic noise spectra of the Kamioka mine.   The three curves represent the seismic noise spectrum of 90th (high, *red*), 50th (mean, *green*), and 10th (low, *blue*) percentile levels. The spectra below 1 Hz are the measurement results, while those above 1 Hz are the extrapolation of the measured data assuming proportional to f^{-2}.

$\sim 10^{-11}$ m/Hz$^{1/2}$ at 10 Hz. Therefore, the required attenuation ratio at that frequency is about 10^{-8} for the test masses.

The second advantage of the underground environment is low gravity-gradient noise that can potentially limit the sensitivity at the lower end of the observation band. Gravity-gradient noise originates from both atmospheric and seismic density fluctuation, producing a varying gravitational force on the test mass. The main sources of this noise can be surface waves of human-induced activity, a bulk motion of the ground, or atmospheric phenomena. Unlike the direct transmission of the seismic noise, the gravity-gradient noise cannot be attenuated with any shields or filters in the path of gravitational coupling. Hence, the situation of the interferometer determines the available noise limit.

The underground situation can improve the gravity-gradient noise from both surface waves of the ground and atmospheric fluctuation. J. Harms estimated the gravity-gradient noise from these sources at the Kamioka mine as $\sim 10^{-20}$ m/Hz$^{1/2}$ at 10 Hz, based on a seismic vibration measurement at the CLIO site [26]. This value is about 2–3 orders of magnitude smaller than the requirement and $\sim 10^{-2}$–10^{-1} times as large as that of the site of Advanced LIGO. Meanwhile, the contribution from water flow near the interferometer may generate gravitational potential perturbation in considerable magnitude since a substantial amount of water can well anywhere in the tunnel. The impact of gravity-gradient noise from this water flow is estimated to be negligible unless either the water velocity is very high ($\gtrsim 10$ m/s) or

Table 3.2. Material properties of the candidates for mirror components

Material	Sapphire	Silicon	Fused silica
Density [g/cm^3]	3.98		
Young modulus [GPa]	398		
Poisson ratio	0.22		
Thermal contuctivity [W m^{-1} K^{-1}]	4300	2330 @ 10 K	0.7
Q-factor (20K)	10^8	10^8	10^3
Q-factor (300K)	3×10^6	10^6	10^7
Absorption @ 1064 nm			

the water flow exists so close to a test mass ($\lesssim 1$ m) [27].

Cryogenic sapphire test masses

The use of cryogenic mirrors is a simple solution to improve the noise contamination due to thermal fluctuations, as the energy of the thermal noise is proportional to the product of temperature and mechanical dissipation. Therefore, it is effective to cool the mirrors down to the cryogenic temperatures and to select a high-Q material as the substrate. In the setup of a laser interferometer, two thermal processes violate the gravitational wave detection: the suspension thermal noise, which is a fluctuation of the suspension point, causes translation of the center of mass of the mirror, and the mirror thermal noise, which is the sum of mechanical dissipations in the substrate and coating of the mirror.

In KAGRA, sapphire is chosen as a material for the substrate and suspension wire of the test masses. The properties of the candidate materials for mirror components of gravitational wave detectors are summarized in table 3.2. Among the candidate materials, sapphire has a high Q-factor, high thermal conductivity, and low optical absorption of 1064 nm wavelength laser at cryogenic temperatures. The high density feature of sapphire also helps to make the mirror heavier with a given volume, resulting in a high inertia. However, fused silica used for mirrors in Advanced LIGO shows characteristics suitable for the laser interferometer, cooling down to cryogenic temperatures deteriorates its Q-factor by roughly 4 orders of magnitude, from 10^7 to 10^3.

3.1.2 Optical layout

The KAGRA interferometer is composed of a number of optical components including not only the main parts of the dual-recycled Fabry-Perot Michelson interferometer but also input, output and auxiliary optics. A schematics of the optical layout of the KAGRA is shown in fig. 3.3.
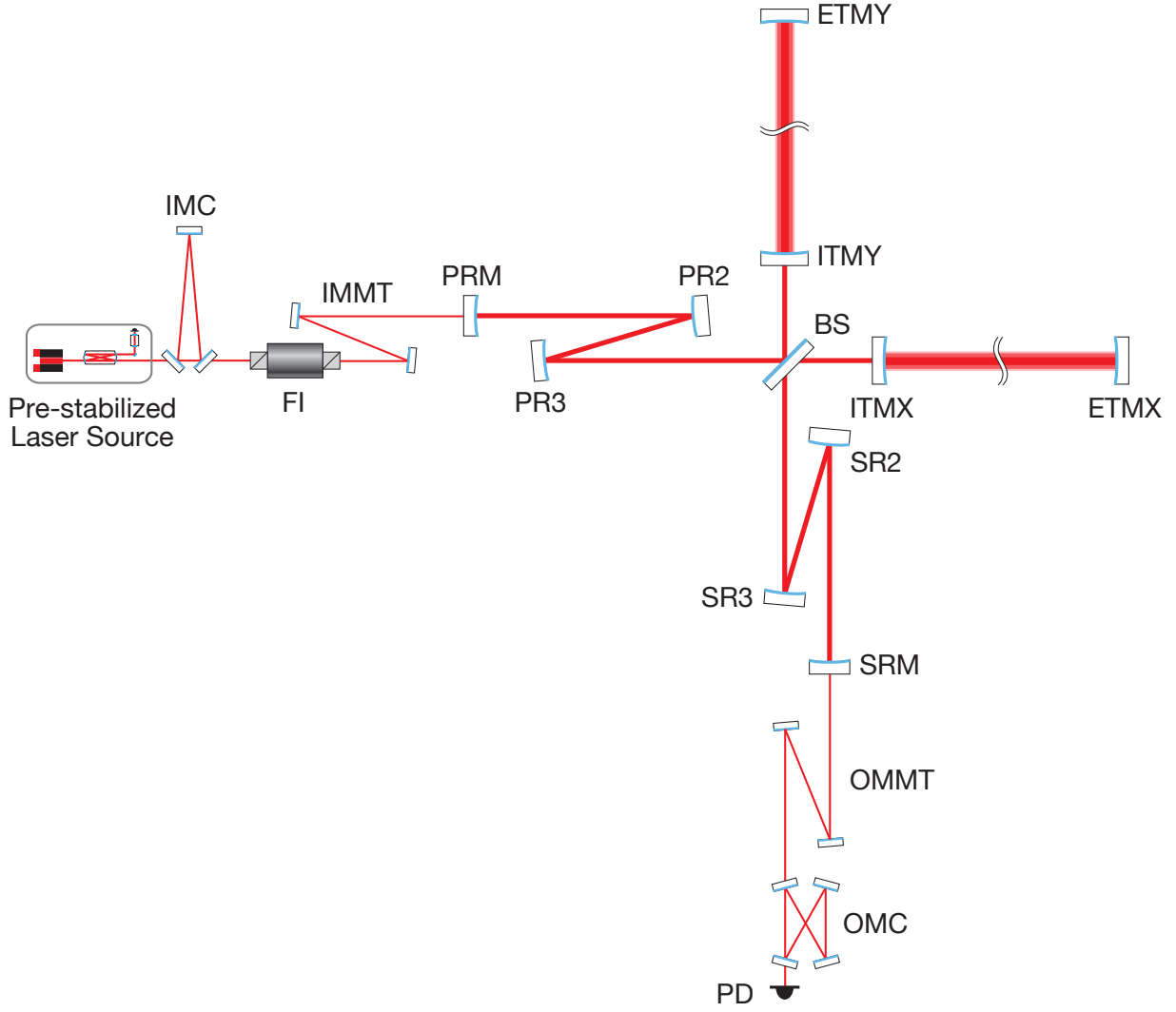
Fig. 3.3. A schematics of the optical layout of the KAGRA interferometer.

The laser source is a Nd:YAG non-planar ring oscillator (NPRO) that has very low intensity noise. Passing through the solid-state amplifier with increasing power of about ~ 200 W, the laser beam goes to the pre-stabilization stage, which applies further intensity stabilization with a pre-mode cleaner, a bow-tie shaped rigid cavity, and frequency stabilizaiton with a rigid reference cavity with high finesse. These pre-stabilization processes are implemented on an in-air breadboard, while following an optical path, and components are placed under vacuum environment.

The pre-stabilized laser beam is sent to the input mode cleaner (IMC), a triangular cavity with suspended mirrors for the purpose of spatial mode shaping and further frequency stabilization. The transmitted beam from the IMC goes through a Faraday isolator (FI), which blocks back-streaming light through a combination of a Faraday rotator and two polarizers to

force the passing beam to follow one path. Then the outcoming beam is magnified through the input mode matching telescope (IMMT) which has spatial mode shaping to match the beam to the following optical cavities. Thus, after these preprocessing steps, the dressed beam is sent to the main part of the interferometer.

The main part of the interferometer is a dual-recycled Fabry-Perot Michelson interferometer with an arm length of 3 km. The arm cavities are conventionally called X-arm and Y-arm, and are formed by the input test masses (ITMs) and the end test masses (ETMs). The incoming beam is divided into two perpendicular directions at the beam splitter (BS) and sent to the arm cavities. The reflected beams from the arm cavities are recombined at the BS. Their interference condition on the BS is retained such that all the power goes back to the incoming direction called the symmetric port.

There are two folded recycling cavities at the input and output of the main interferometer. At the input (symmetric port), the power recycling mirror (PRM) reflects the back-coming beam again to the arm cavities. The power recycling cavity, formed by the PRM and equivalent ITM (a virtual ITM located at the averaged distance of the ITMX and ITMY from the BS) stores the reflected power from the arm cavities, amplifying the effective intracavity power of the arms. Similarly, a signal recycling cavity is implemented at the output (anti-symmetric port) of the Michelson interferometer. Although the interfered light is kept dark during observation, a tiny amount of power leaks out at the anti-symmetric port when gravitational waves pass through the interferometer. The signal recycling mirror (SRM) sends the leaked photons (signal of the GWs) back to the arm cavities so that the interaction between the photons and the gravitational waves can be increased.

Finally, the leaked beam from the signal recycling cavity is detected at the photo-detector (PD), with post-processing through the output mode matching telescope (OMMT) and the output mode cleaner (OMC). The OMMT diminishes the beam radius by shaping its spatial mode so that it can match the following OMC cavity. The OMC is a bow-tie shaped cavity mounted on a monolithic breadboard with less thermal expansion.

3.2   Overview of KAGRA suspension systems

The main interferometer of KAGRA consists of a number of optics, whose fluctuations have different levels of impact on gravitational wave detection depending on its position. Hence, we employ three types of suspension systems for the optics of the main interferometer, namely type-A, type-B, and type-Bp suspension. The overview and configuration of these three types of suspensions are shown in fig. 3.4 and fig. 3.5, respectively. Basic information about the suspension types is also listed in table 3.3.

The type-A suspension is the largest vibration isolation system for the cryogenic test masses in the 3 km arm cavity. As the local motion of the test masses directly couples to

Table 3.3. Basic specification of the three types of the KAGRA suspension systems

	Type-A	Type-B	Type-Bp
Assigned optics	ITMX	BS	PRM
	ITMY	SRM	PR2
	ETMX	SR2	PR3
	ETMY	SR3	
Horizontal stages	9 (IP included)	5 (IP included)	3
Vertical stages	5	3	2
payload type	cryogenic	room temperature	room temperature
	parallel	branch	branch

the change in differential arm length, we apply the highest vibration isolation on them. The Type-A suspension has 9 suspended stages including an IP pre-isolation stage and 5 GAS filter with a height of 13.5 m. Owing to the height of the system, the base of the type-A suspension sits on the upper floor of the tunnel, which is separately excavated at a higher elevation. The bottom four stages are called *cryogenic payload*, containing a sapphire test mass and being operated under ~ 20 K. The cryogenic payload is a parallel chain of the main masses and the reaction masses. The reaction is connected to a cooling bar inside a double-shielded cryostat for conductive cooling via heat links. The detailed design of the type-A suspension will be described in the following sections.

The type-B suspension is the second largest vibration isolation system used for the BS and signal recycling mirrors. It has a total of five suspended stages and contains IP pre-isolation stage as well as the type-A suspension. The base of the Type-B suspension sits on an external support frame bedded on the ground floor of the tunnel. The payload of the Type-B suspension is a branched chain of the main masses and the reaction masses, which is operated at room temperatures. In the setup of a branched chain, a main mass and its recoil mass are suspended from the next main mass of the upper stage. On the other hand, in the parallel chain such as the Type-A suspension, the main mass and its recoil mass are separately suspended from their own next upper masses.

The Type-Bp suspension is the reduced version of the Type-B suspension and is used for the power recycling mirrors. It has three suspended stages and two GAS filters with the height of 2 m, while the IP pre-isolation stage and the number of GAS filters are omitted due to budgetary constraints. The base of the Type-Bp suspension sits on an inner frame of the vacuum chamber. The absence of the IP stage makes it impossible to adjust the position of the suspension point and control the fundamental mode of the whole translation. The first problem, the position adjustment of the suspension point, is solved by using a motorized base called a *traverser*. The second problem, the control of the translational modes of the entire

Table 3.4. Longitudinal displacement noise requirements at 10 Hz of the core optics of the KAGRA main interferometer. The stricter value in two operational mode of the interferometer is chosen.

Optics	Displacement noise [m/Hz$^{1/2}$] @ 10 Hz
TM	8×10^{-20}
BS	6×10^{-18}
PRM	1×10^{-15}
PR2, PR3	5×10^{-16}
SRM	5×10^{-18}
SR2, SR3	2×10^{-18}

chain, can be overcome with an additional recoil mass applied on the bottom GAS filter. Thus the Type-Bp suspension becomes a branched suspension from the top to the bottom. The design of the payload is shared with that of the Type-B suspension and is operated also at room temperatures.

The basic specification of these suspension systems are determined by the required seismic attenuation performance, or the required displacement noise under the seismic excitation of the Kamioka underground site. The sensitivity of the KAGRA main interferometer in the observational band is limited by the suspension thermal noise and quantum noise. The goal of the vibration isolation system is to attenuate other noise source contributions so that they are low enough compared to these fundamental noises. The requirements of the mirror displacement noise are set as small as 1/10 of the sensitivity curve above 10 Hz. The spectral requirements for the suspensions in each operational mode of the interferometer are plotted in fig. 3.6, and the their values at 10 Hz are summarized in table 3.4. In table 3.4, the stricter requirement of the two operational modes of the interferometer is listed. Comparing to the Type-A suspension, the allowed displacement noise for the Type-B optics is roughly 10^1–10^2 larger and for the Type-Bp optics is 10^4–10^5 larger. The requirements of the folding mirrors in the power/signal recycling cavities are 0.5 times lower than PRM/SRM, as their longitudinal displacement alters the cavity length by two times.

The discussion of the requirements above is the subject of longitudinal seismic attenuation and couplings from other DoFs or other noise sources. We need vibration isolation in the vertical direction owing to the vertical-to-longitudinal (V-to-L) coupling, as described in the previous chapter. In the case of a 3 km separation, the V-to-L coupling caused by the curvature of the Earth is estimated as at most 1%. In addition, there is another path of the V-to-L coupling that comes from the inclination of the KAGRA tunnel. KAGRA is not constructed on an exactly horizontal plane for a practical reason: as there are many ground-water springs inside the Kamioka mine, the L-shaped tunnel has been excavated with a tilt of

1/300 for drainage. Owing to this inclination, the local vertical motion of the mirrors alters the longitudinal cavity variation at least by 0.3% even without other mechanical couplings. Taking these considerations into account, we assume the V-to-L coupling in the suspension system as 1% in the following discussions.

Fig. 3.4. Overview of the suspension systems in KAGRA, rendered in a reduced scale. Three types of suspensions, namely Type-A, Type-B, and Type-Bp suspension, are employed for vibration isolation of the core optics.
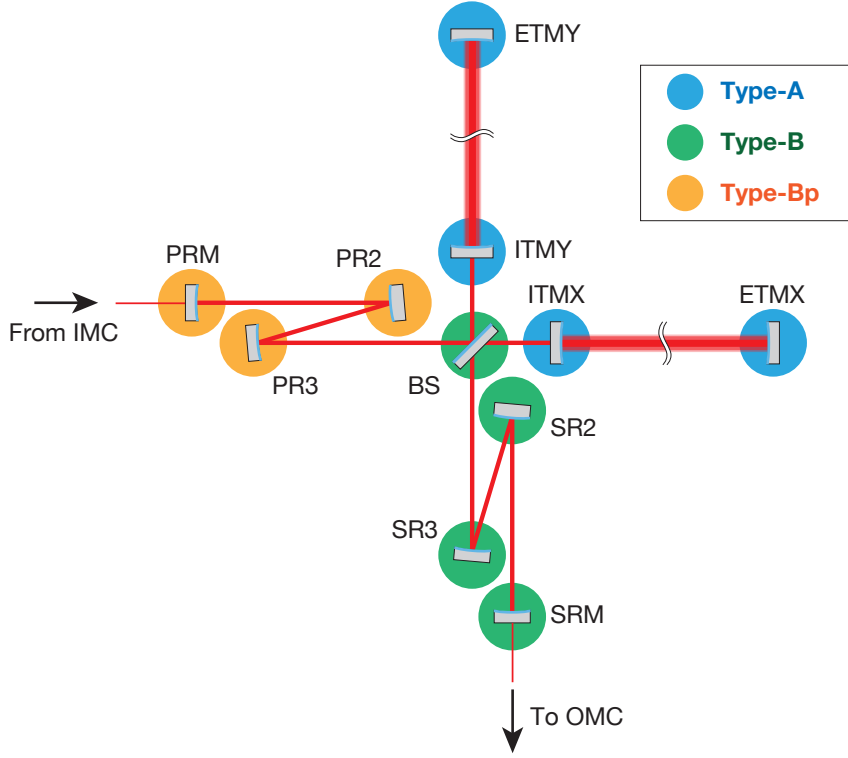
Type-A   **Type-B**   **Type-Bp**

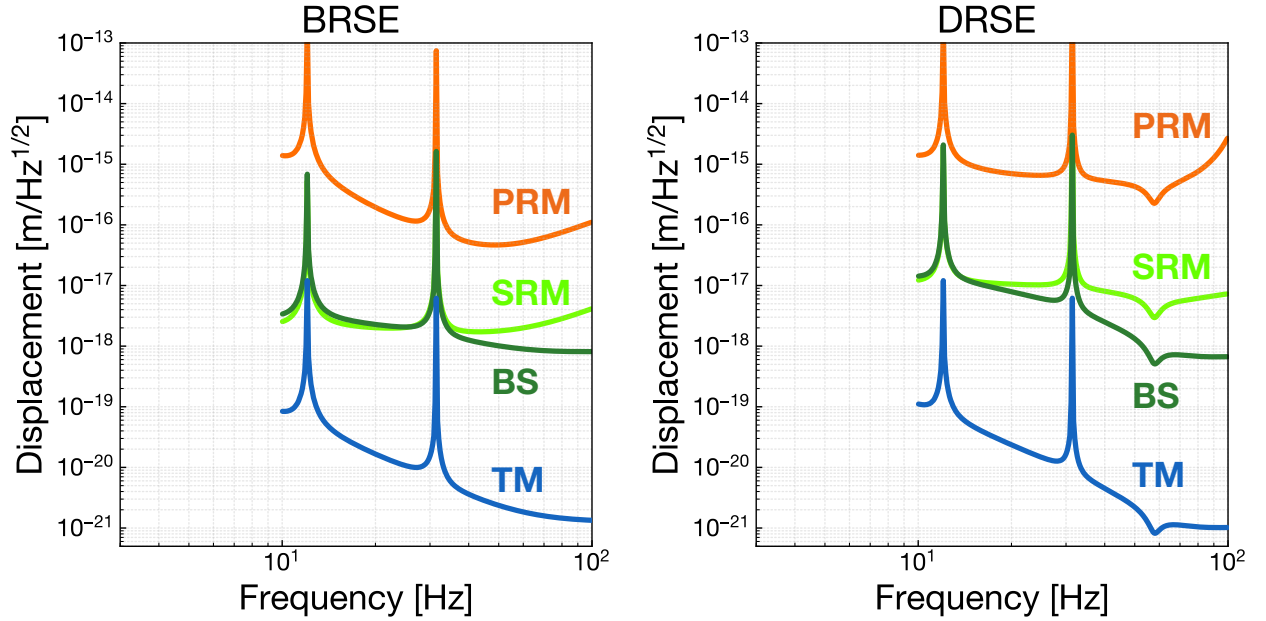**Fig. 3.5.** Configuration of the suspension systems in the KAGRA main interferometer.

Fig. 3.6. Longitudinal displacement noise requirements of the core optics of the KAGRA main interferometer in two operational modes.

3.2.1 Control phases

The KAGRA main interferometer is formed by optics individually suspended from their vibration isolation systems. While the optics need to be controlled globally to realize the interferometer operation as the whole, each optic is subject to incoherent disturbance caused by the seismic noise. Although the suspension systems achieve sufficient seismic attenuation in the frequency band of gravitational wave observation, they also have to suppress the out-of-band mirror fluctuation so that a global interferometer system can be achieved. The suspension systems enhance mirror vibration at their mechanical resonances as they stand, which typically have high quality factors, or long decay times, in other words.

We govern the suspension systems with active control in order to suppress these low frequency motions of the optics. The active control is based on linear feedback control making use of several kinds of vibration sensors, contactless actuators, and digital servo systems. The mechanical resonances can be damped also by passive dampers such as eddy current dampers, which have better stability of working once they are installed. Active control requires careful dedication to the servo design for stable operation, thus at this point, it has troublesome complexity. On the other hand, the flexibility of active control, which can easily switch the control strategy depending on the states of the interferometer even after the mechanics of the suspension system is installed, outweighs the difficulties of handling.

The states of the interferometer control can be categorized into three phases, namely calm-down phase, lock acquisition phase, and observation phase. The transition strategy between these phases is visualized in fig. 3.7. The calm-down phase is the state where the optics are swinging with large amplitudes and the interferometer is no longer kept aligned to produce any meaningful signals. In this phase, the suspension systems need to suppress the vibration of the optics to restore their nominal positions so that the interferometer can start lock acquisition. Here the control gives priority to robustness against large disturbances than quiescence of the control noise. Hence, the actual topic in the calm-down phase turns to mode damping of its mechanical resonances. Second, the lock acquisition phase is the state where the interferometer recovers the Fabry-Perot cavities so that they are locked in their resonant conditions. As the linear region of the interferometer (PDH) signals is considerably small, the control has to reduce the velocity of the suspended optics so that it is small enough to allow the limited actuation power to have an effect. The local control is also required to suppress the angular fluctuation so that the control loop with more sensitive sensors of the interferometer, such as the wave front sensors, can be engaged. Finally, all the cavities of the interferometer are locked and the control moves to the observation phase where gravitational wave detection is in operation. The most important point in this phase is less control noise to perform the observation with a better interferometer sensitivity, as well as to keep the mirror displacements and orientations in a certain range for stable operation.
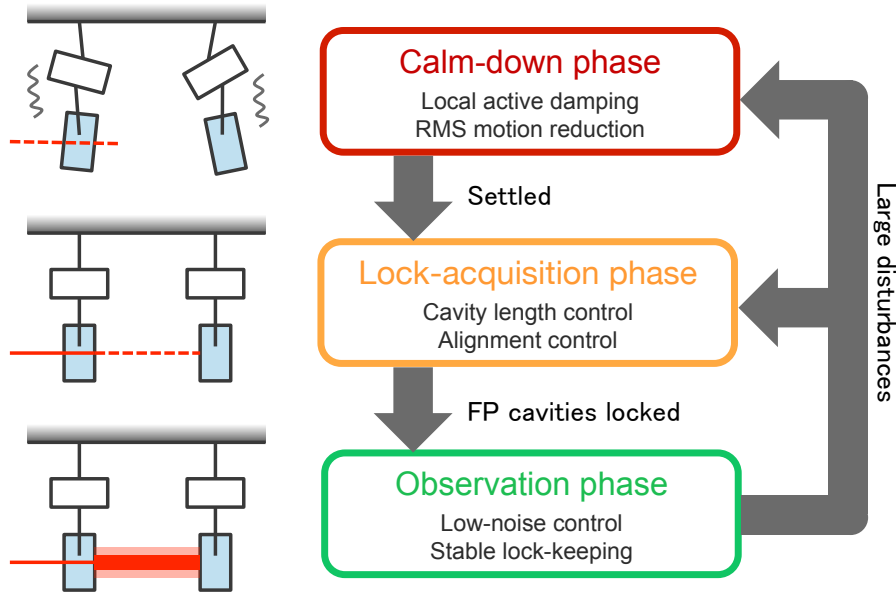
Fig. 3.7. Phases of the interferometer control in KAGRA. Information about each control phase is also summarized.

3.2.2   Requirements

The suspension systems need to provide sufficiently stabilized mirrors so that the residual motion is at a level suitable for the phase of the interferometer control. Thus, the requirements of the Type-A suspension are set in each control phase, as summarized in table 3.5. The derivations of each type of requirement are described in the following subsections.

1/e modal decay time

The calm-down phase places importance on quick recovery of the interferometer signals. However, a large amplitude of the mirror's residual motion, which is usually driven by the mechanical resonances of the suspension system, makes the signals unavailable. Thus, the requirement has been set that the 1/e decay time of the mechanical resonances involving in the interferometer operation has to be less than 1 min. This value is empirically determined so as not to prevent the interferometer from trying a lock acquisition for a long time [19].

RMS residual motions for calm down

Other requirements in the calm-down phase are basically intended to settle the excited vibrations to their usual stationary state so that smooth transition to the next lock acquisition phase can occur. Thus the requirements on the RMS displacement (L) and the RMS angles (P, Y) are set as $50\,\mu$m and $50\,\mu$rad, respectively [19]. The RMS displacement for the other translational DoFs (T, V) are required for another reason that is mentioned shortly later.

Table 3.5. Requirements on the vibration isolation and active control of the Type-A suspension. The abbreviations of the suspension's DoFs are as mentioned in section 2.3.

Calm-down phase		
Item	Requirement	For/Determined by
$1/e$ modal decay time	< 1 min	Quick recovery
RMS displacement (L)	< 50 μm	Smooth transition to next phase
RMS displacement (T, V)	< 0.1 mm	Miscentering
RMS angle (P, Y)	< 50 μm	Smooth transition to next phase
Lock acquisition phase		
Item	Requirement	For/Determined by
RMS velocity (L)	< 240 μm/s	Auxiliary laser locking
RMS displacement (T, V)	< 0.1 mm	Miscentering
RMS angle (P, Y)	< 880 nrad	Optical gain degradation < 5%
Observation phase		
Item	Requirement	For/Determined by
Displacement noise (L) @ 10 Hz	< 8×10^{-20} m/Hz$^{1/2}$	Sensitivity
Displacement noise (V) @ 10 Hz	< 8×10^{-18} m/Hz$^{1/2}$	Sensitivity (1% coupling to L)
RMS displacement (T, V)	< 0.1 mm	Miscentering
RMS angle (P, Y)	< 200 nrad	Beam spot fluctuation < 1 mm
DC drift (P, Y)	< 400 nrad/h	Sustainable lock for 1 day left

RMS velocity for lock acquisition

The arm length stabilization of the Fabry-Perot interferometer is accomplished by using modulated laser beams; this technique is called the Pound-Drever-Hall (PDH) technique or frontal modulation technique [28]. The amplitude or phase of the laser is modulated at radio frequencies before entering the main interferometer. By demodulating laser power detected at the photo-detector in the proper phase, one can obtain an error signal proportional to the displacement from the working point. Instead of yielding the small linear region of the proportionality of the error signal, the control locked with this scheme can stabilize the laser frequency or the position of the optics in an extreme precision. The width of the linear region is determined by the finesse of the cavity $\mathcal{F}$ and wavelength of the laser λ with the following equation,

$$\Delta L_{\mathrm{lin}} = \frac{\lambda}{2\mathcal{F}} \; . \tag{3.1}$$

According to the finesse of 1550 for the arm cavities and the wavelength of 1064 nm for the main laser in the KAGRA interferometer, the width of the linear region can be interpreted

as the geometrical displacement of the cavity of 3.4×10^{-10} m.

Acquiring the lock of the optical cavity means that the velocity of the cavity length variation has to be zero with respect to the resonant peaks aligned with the interval of the free spectral range. Hence the feedback force needs to stop the suspended mirror while the mirror is passing across the small linear region. However, the test mass actuators will often lack sufficient authority to gain control for nulling the mirror velocity since their design follows the policy of mitigating force noise. To support the lock acquisition of the arm cavities, the KAGRA interferometer adopts a so-called *green lock* scheme [29], which introduces a frequency-doubled auxiliary laser with lower finesse for the arm cavities.

The requirement of the RMS velocity in the longitudinal direction has been derived from the condition that the time scale where the mirror goes across the linear region of the PDH signal is sufficiently longer than the duration of the control bandwidth. Thus the incident velocity of the mirror needed to acquire the cavity lock should satisfy the following inequality,

$$v_{\text{in}} \lesssim \omega_{\text{b}} \Delta L_{\text{lin}} = \frac{\omega_{\text{b}} \lambda}{2\mathcal{F}} \; . \tag{3.2}$$

Here ω_{b} denotes the control bandwidth. In the case of Type-A suspension, the green lock can be equivalent to the lock acquisition in the scope of local control. Therefore, the incident velocity required for the green lock is calculated as 334 μm/s for $\omega_{\text{b}}/2\pi = 10$ Hz, $\lambda = 532$ nm, and $\mathcal{F} = 50$.

The actual incident velocity of the mirror shows a stochastic behavior because the mirror is driven by random disturbances. Assuming that the velocity of the mirror follows Gaussian distribution, the incident velocity of the optical cavity will have the following probability distribution [30],

$$f(v) = \frac{v}{v_{\text{RMS}}} \exp\left(\frac{v^2}{2v_{\text{RMS}}^2}\right) \; , \tag{3.3}$$

where v_{RMS} denotes the RMS velocity of the cavity length variation. By imposing a probability of the lock acquisition higher than 50% in this model, the RMS velocity of the length variation should be suppressed lower than $0.72\, v_{\text{max}}$, where v_{max} is the maximum acceptable velocity. From the discussions above, the requirement on the RMS velocity has been set as 240 μm/s for the Type-A suspension [19].

RMS alignment angles (P, Y)

The mirror rotation in the alignment angles, namely pitch and yaw, causes beam spot fluctuation and spatial mode mismatch in the interferometer. As the test masses are separated by kilometers, even small fluctuations of the mirror angles result in large beam spot displacements. The requirement in the lock acquisition phase comes from the requirement that the intracavity power should not degrade with a loss more than 5% [31], while the one

in the observation phase comes from the fact that the beam spot fluctuation at the 3 km distance should be less than 1 mm.

3.3   Mechanical design

The Type-A suspension is a nine-stage pendulum consisting of an IP pre-isolation stage, a chain of GAS filters, and a parallelized payload. The 3D drawing of the overall Type-A suspension is shown in fig. 3.8. The pre-isolation stage consists of the base ring, inverted pendulum legs, and a top GAS filter that sits on the base frame fixed on the ground. The first top stage is supported by three inverted pendulum (IP) legs. The chain of GAS filters starts from the top filter (F0) mounted on the top stage, includes the filters on succeeding stages named filter 1, 2, and 3, (F1, F2 and F3 in short, respectively,) and then ends with the fifth stage called the bottom filter (BF). The stages suspended from the BF are called the *cryogenic payload* (also called *payload* or CRYp in short), which begins with the platform (PF). From the PF, two chains of three-stage pendulums, namely test-mass (TM) chain and recoil-mass (RM) chain, are suspended in parallel. The three stages in the TM chain are named the marionette (MN), intermediate mass (IM), and the test mass (TM), which is a sapphire mirror that reacts to GWs. The RM chain has mass stages that surround the corresponding mass in the TM chain to apply an actuation force isolated from the ground disturbance.

The suspension wires above the PF are made of maraging steel with heat treatment to increase their tensile strength. In the payload, the sapphire fibers are designed for the suspension wire for the TM, paying special attention to the thermal conductivity. Other wires in the payload are made of maraging steel or copper beryllium depending on the location to be used.

Some auxiliary mechanical parts are connected to the suspension chain. One is the magnetic damper (MD), which applies viscous-damping force on the neighboring F1 stage. The magnetic damper is suspended from the top stage with three maraging wires. Another one is the heat link connected from the cooling bar to the marionette-recoil mass for the purpose of quick cooling via conductive heat transfer.
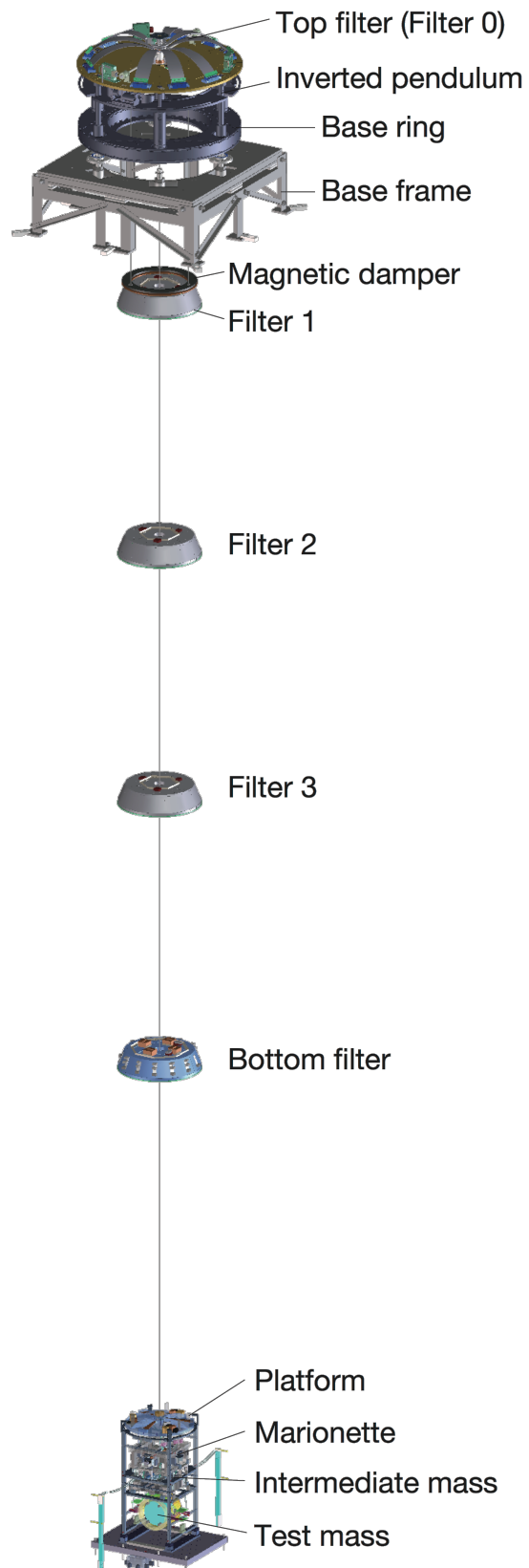
Fig. 3.8. An overview of the Type-A suspension from the top to the bottom.

3.3.1   IP pre-isolation stage

The IP pre-isolation stage, called *pre-isolator*, consists of IP legs, a base ring, and the top GAS filter. The function of this stage is to provide the first mechanical resonance below 0.1 Hz for horizontal motion. Since the position of the suspension point for the following chain is determined by the translation of this stage, it also provides controllability of the static position and yaw orientation of the mirror.

An overview drawing of the pre-isolator is shown in fig. 3.9. The top stage is supported by three IP legs in each 120° rotation. Three pillars placed at the mid point of the IP legs rigidly connect the base ring to the reference frame where units of the sensor-actuator device and the lock pillar are mounted to mechanically fix the top stages for safety reasons. On the top stage, the thinner tip of the cantilever blades is connected to the keystone enclosed by the central structure of the top filter. The velocity sensors, commercial products named *geophone L-4C*, packaged in the vacuum canister are mounted on the top stage so that the inertial sensor is independent of the ground disturbance. One of the suspension wires for the main chain is set at the keystone of the top GAS filter, while the other three wires for the magnetic damper are directly set on the ceiling of the top stage.

The detailed dimensions of the IP leg are shown in fig. 3.10. The total height of the IP leg is 520 mm, which is much smaller than that of the Virgo Superattenuator, which is of 6 m. This IP has the flexure joints at both ends of the hollow cylinder of the leg. The flexure joints are made of maraging steel, a special arroy known for its superior strength and toughness after aging treatment, that allows robust elastic bending beside the top stage displacement. The hollow legs of ~ 0.3 kg each mitigate the saturation of the attenuation performance at higher frequencies. A skirt around the bottom flexure where the counter weights are mounted enables the center of percussion to coincide with the fixing point of the flexure. The saturated attenuation factor, which is usually $\sim 10^{-3}$, can be improved to $\lesssim 10^{-4}$ by introducing the counter weights. Each IP stands on the cone bellows supported by in-air screw jacks that enable us to adjust the height of the IP's feet so that the ground plane to be horizontal.

The details of the top GAS filter will be presented in the next subsection, as its structure and functions are similar to those of the standard GAS filter. The sensors and actuators are also explained later.
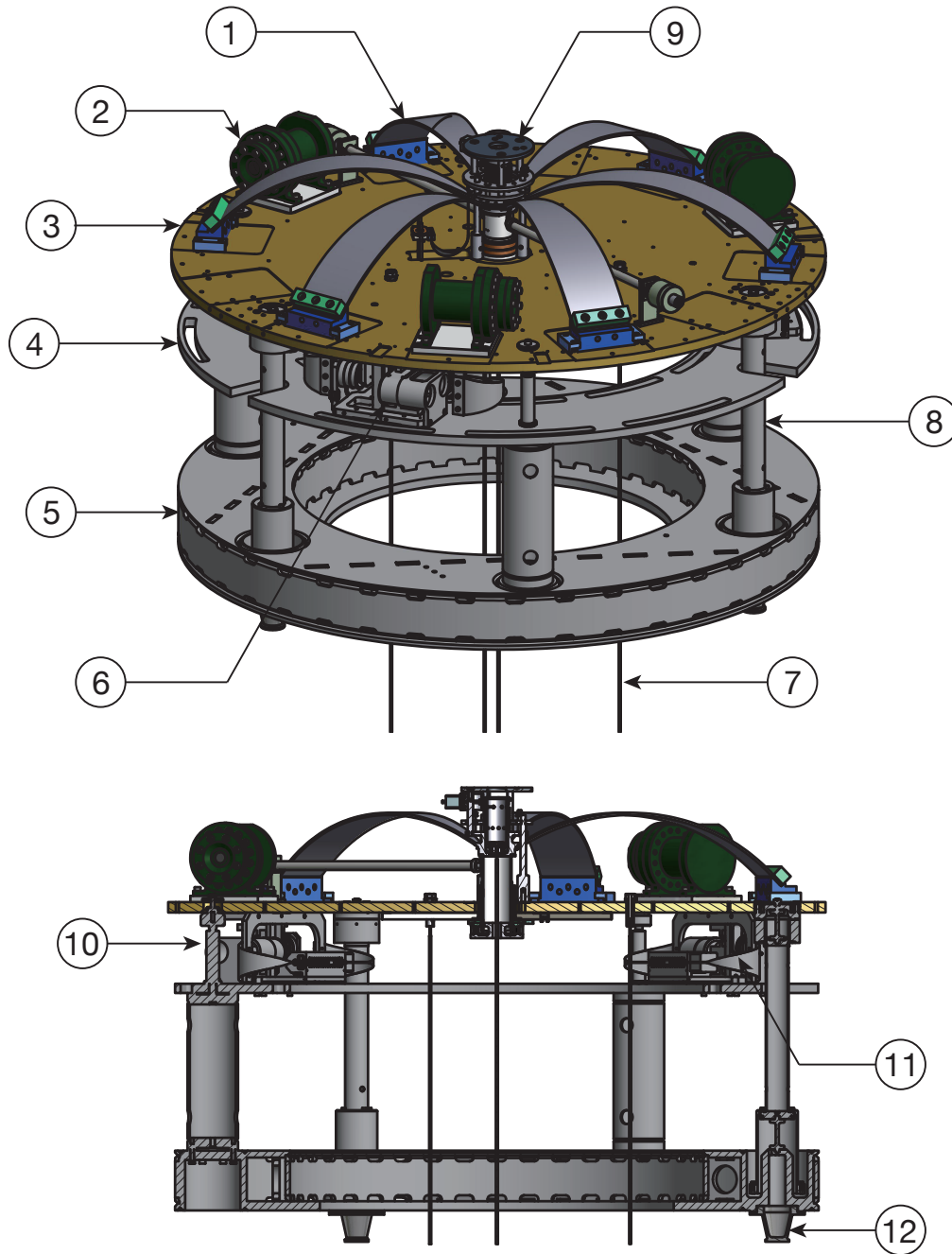
Fig. 3.9.   An overview of the pre-isolator (*top*) and its cross-section view (*bottom*). The numbered components are the 1) cantilever blade, 2) geophone capsulated in a vacuum canister, 3) table of the top stage, 4) reference frame rigidly connected to the base ring, 5) base ring, 6) unit of the LVDT and the coil-magnet actuator, 7) suspension wires, 8) IP leg, 9) keystone and the surrounding structure of the top filter, 10) lock pillar for the top stage, 11) motorized blade spring for static position control of the top stage and 12) cup of the cone bellows.
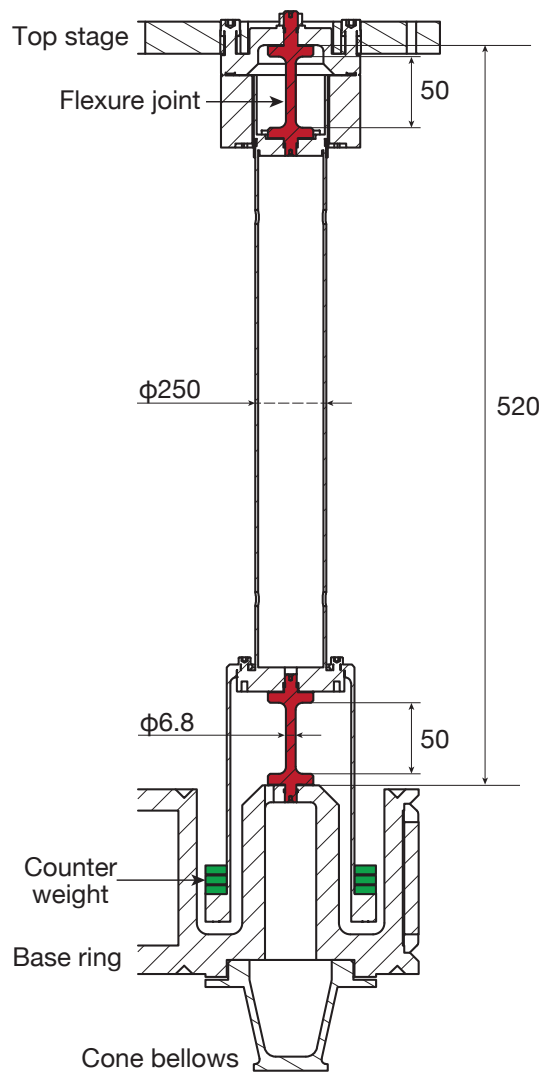
Fig. 3.10. A cross-section view of the IP leg.

3.3.2 GAS filter chain

The type-A suspension has 5-stage of GAS filter chain cascading from the IP pre-isolation stage in order to meet the required seismic attenuation in the horizontal and vertical directions. The first GAS stage, called *top GAS filter*, is implemented directly on the top stage. In the following three stages, we use a GAS filter called a *standard GAS filter* , as it has a more compact design. which is called The last stage of the tower part, called *bottom GAS filter*, has basically the same mechanical design as the standard GAS filters. However, the bottom filter is distinguished from the other standard filters because of some important functions that allows it to act as an interface between the tower and the payload.
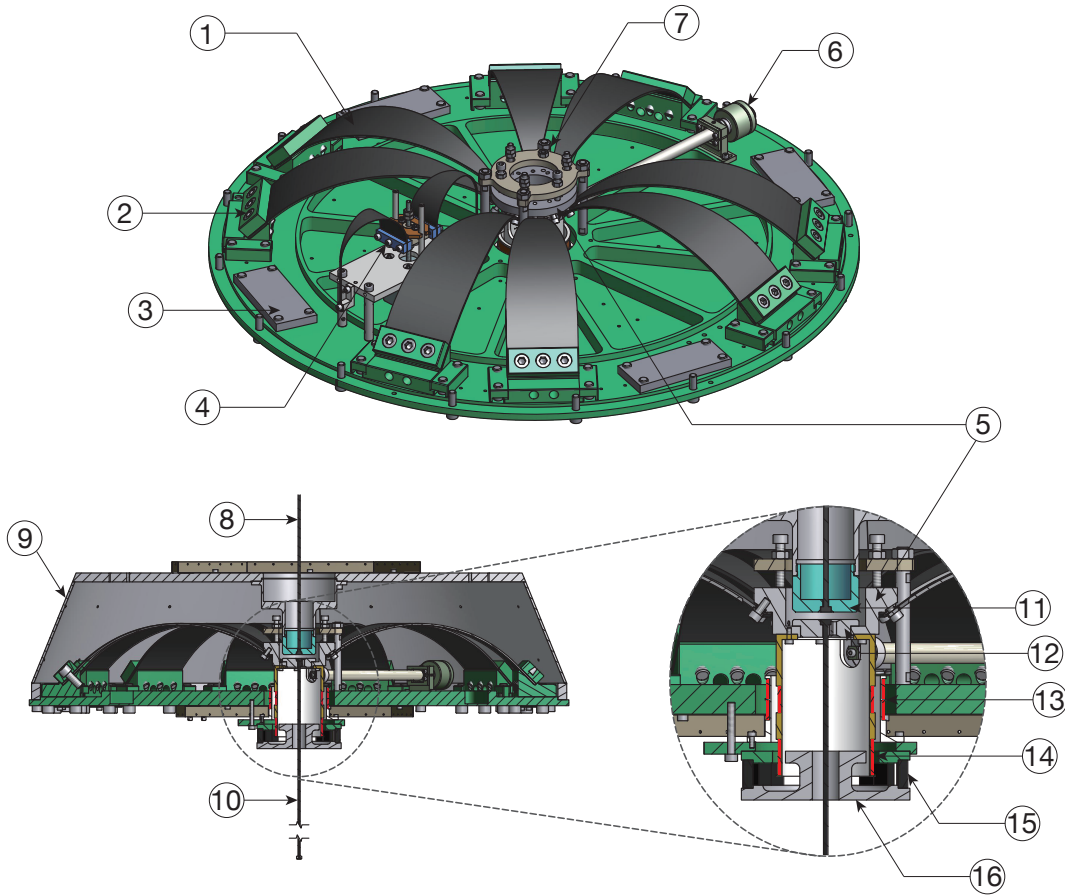
Fig. 3.11. An overview of the standard GAS filter without the cap (*top*) and its cross-section view with the cap (*bottom*). The numbered components are the 1) cantilever blade, 2) blade clamp, 3) ballast mass, 4) fishing rod, 5) keystone, 6) magic wand, 7) lock screws and nuts, 8) upper suspension wire, 9) filter cap, 10) lower suspension wire, 11) wire receptacle for the upper wire, 12) wire receptacle for the lower wire, 13) coils for LVDT displacement sensor, 14) actuator coil, 15) magnets and 16) iron yoke.

Blade profile

X	Y
0	40
13.63	39.7288
27.26	39.4575
40.89	39.2358
54.52	38.7481
68.15	37.9944
81.78	37.0412
95.41	35.8221
109.04	34.3812
122.67	32.7187
136.3	30.8566
149.93	28.7951
163.56	26.5784
177.19	24.1622
190.82	21.6484
204.45	19.0216
218.08	16.2175
231.71	13.2293
245.34	10.4429
258.97	8.20848
272.6	6.33315

Fig. 3.12. Dimension of a cantilever blade for the standard GAS filter in Type-A suspension.

The basic structure of a standard GAS filter is implemented on a disk-shaped base plate as shown in fig. 3.11. As described in section 2.4.2, quasi-triangular cantilever blades are radially mounted on a base plate. The tips of the bent blades are fixed to the keystone where a suspension wire for the lower stages is hooked. Owing to this axisymmetric constraint, the keystone can oscillate only in a vertical direction. The wire from the upper stage will be hooked at the center of the cap which is shaped like a trancated cone and clamped on the base plate with screws at its radial edge. The wire receptacles on both the cap and the keystone are positioned such that the suspension points become closer to its center of mass. In addition, a magic wand is attached on the keystone to compensate the center of percussion effect.

Each cantilever blade is designed to be subject to uniform stress distribution in the compressed situation. All the GAS blades in the KAGRA suspension systems have cosine profiles similar to the standard one, as drawn in fig. 3.12. Note that the surface stress is proportional to the thickness and inverse of the length of the blade, indicating this ratio is kept constant in usual design procedure.
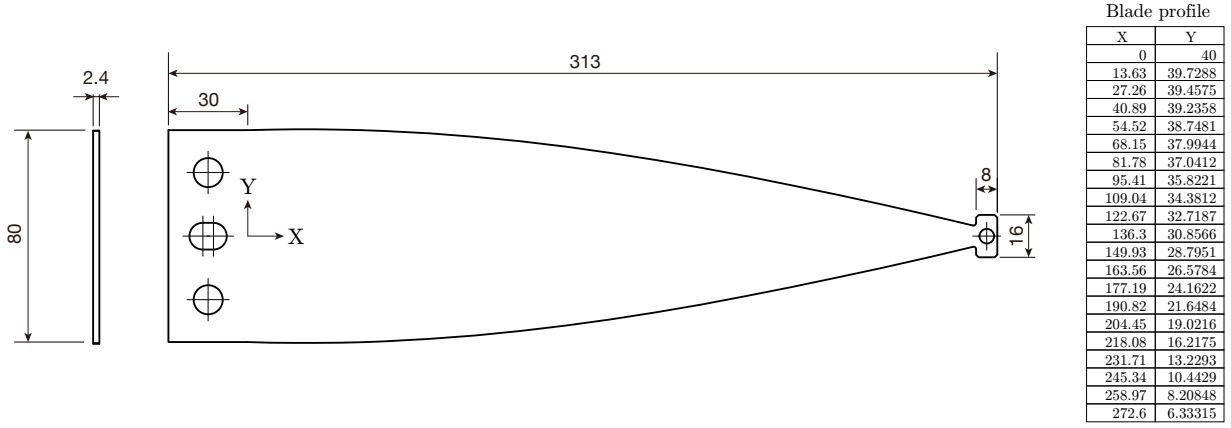
The width, thickness, and number of the GAS blades are adjusted so that their optimal load is equal to the suspended weight from the stage. Intuitively speaking, a stage that supports a heavier load requires a larger anti-spring effect to achieve the given resonant frequency. Therefore, the top GAS filter has thicker blades and the upper standard GAS filters has a greater number of blades. The blade parameters for each GAS filter are listed in table 3.6.

The vertical oscillation of the keystone is monitored with a LVDT displacement sensor, and is controlled with a coil-magnet actuator. These apparatuses are implemented coaxially at the bottom of the base plate. For static position adjustment, a motorized blade spring, called a *fishing rod*, is attached on the upper part of the keystone. Although the total stiffness of the keystone increases by adding the blade spring of the fishing rod, we confirmed that

Table 3.6. Blade parameters of the GAS filter in Type-A suspension.

Stage	Thickness [mm]	Base width [mm]	# of blades
Filter 0 (top)	5.0	125	6
Filter 1 (standard)	2.4	80	12
Filter 2 (standard)	2.4	80	10
Filter 3 (standard)	2.4	80	8
Bottom filter	2.4	80	5
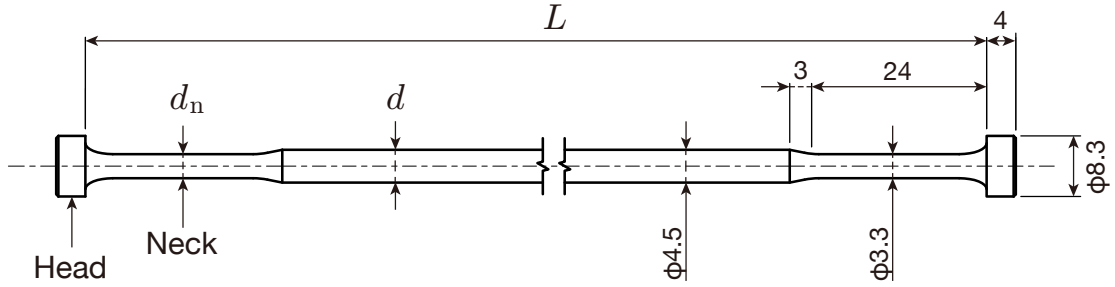
Fig. 3.13. Design of the maraging wire.

deterioration of its resonant frequency is less than 10 % for all GAS filters.

3.3.3 Maraging wire

The main chain from the top stage to the platform in the cryogenic payload is connected with single maraging wires. The maraging wire is capable of suspending a heavy payload with enough mechanical stability.

Maraging steel, the material used for not only the suspension wires but also the blades in the GAS filters and flexure joints in the IP legs, is a low carbon containing ($\lesssim 0.03\%$) iron alloy with nickel, cobalt, and molybdenum. Through martensitic transformation and age hardening [1], maraging steel acquires an ultimate tensile strength of $\gtrsim 1600$ MPa. It is widely used in suspension systems in gravitational wave detectors, as its low mechanical shot noise induced by microscopic creeps under stress, which is an accumulation of quantized yielding process, such as the movement of dislocations and diffusion of vacancies in crystalline structure, results in long-term plastic deformation even below the yield stress of the material.

The dimension of the wire is not uniform; it has thicker heads at both ends, which will be hooked on the wire receptacle at the keystone or the cap. It also has a thinner neck with a length of a few centimeters, as shown in fig. 3.13.

The neck part with a smaller diameter is machined in order to reduce the effective

---

[1] Actually, the name of "maraging steel" is a compound of *martensitic* and *aging*.

bending offset from the suspension point. In an ideal rigid body model with massless wire connections, the wire bends exactly at the clamping point on the body. However, in reality, the wire has bending elasticity and thus bends at an offset point from the clamping point with a finite radius of curvature. This effect, sometimes referred to as the *bending point effect*, will deteriorate the seismic attenuation performance because the effective length of the pendulum reduces and the, resonant frequency increases. The offset of the bending point Δ is calculated through the following relationship.

$$\Delta = \sqrt{\frac{EI}{T}} \tag{3.4}$$

Here E is the Young modulus (modulus of longitudinal elasticity), I is the second moment of area, and T is the tension on the wire. The wire with diameter of d has a second moment of area of $I = \pi d^4/64$. In the case of the suspension systems in KAGRA, the offset of the bending point stays in the mm-cm scale, much smaller than that of the wire length $L \sim$ of a few meters; therefore, the bending point effect can be assumed to be negligible.

The diameter of the neck is designed such that the maximum Mises stress under loading is below the yield stress of the maraging steel with a safety factor of 2 [32]. The fillet part between the head and neck is machined to be an elliptic dimension, which is optimized to mitigate stress concentration.

The chain of single-wire suspensions behaves also as a torsion pendulum with very low resonant frequency in general. The torsional oscillation is driven by the stiffness of the wire independently of the gravitational restoring force. The spring constant of the torsional motion is written as,

$$k_{\text{tor}} = G\frac{\pi d^4}{32L} \ , \tag{3.5}$$

where G is the shear modulus; the factor $\pi d^4/32$ originates from the polar moment of inertia of area. The torsional stiffness is calculated as an integration over the wire length, while the bending point offset described above is determined by the diameters in a few centimeters just from its clamping point. Thus, the maraging wire has a smaller thickness at the both ends and larger thickness in the middle. However, even with the thickness treatment, the single-wire suspension chain still possesses low-frequency torsional modes (< 0.1 Hz) that leads to large angular fluctuation of the mirror in yaw and misaligns the interferometer configuration. The Type-A suspension overcomes this torsional-mode problem by passive and active dampers, which will be explained in the following subsections.

3.3.4 Magnetic damper

As discussed in the previous subsection, a single-wire suspension chain behaves as a torsion pendulum with a very low resonant frequency ($\lesssim 0.1$ Hz). This torsional oscillation,

when once excited, lasts for a long time owing to its high quality factor originating from the intrinsic mechanical loss of the wire. For quick recovery of the interferometer operation, we have to decrease the torsional motions corresponding to the horizontal alignment of the mirror.

The magnetic damper is a passive damping mechanism that uses eddy currents. An eddy current damper consists of permanent magnets fixed on the reference side and conductive plates attached on the oscillator side to be damped. When a conductive object feels an alternation of nearby magnetic fields, it generates eddy currents on its surface so as to oppose the time-varying magnetic fields. A breaking force is therefore produced on the oscillator (or breaking torque for rotational oscillation).

The conceptual design of the magnetic damper in the KAGRA suspensions is a ring with arrayed permanent magnets suspended from the pre-isolation stage by three wires and placed just above the first standard GAS filter (F1). The magnets are arranged such that the overall magnetic dipole moment cancels out. The damper ring faces copper plates attached on the top of the F1 stage, with a gap of ~ 5 mm.

The single magnetic damper is not adequate to damp the torsion mode of the long chain of the Type-A suspension, since the magnetic damper can apply a breaking torque only onto the F1 stage, which is close to the node of the open-ended fundamental torsion mode. To damp a specific natural mode whose mode shape is known, it is effective to implement a damper at the position of its antinode where the mode has large amplitude. Thus, the second torsion-mode-damping mechanism is implemented on the bottom filter in the Type-A suspension, as described in the next subsection.

3.3.5 Bottom filter

The bottom filter is the last GAS stage in the tower part of the Type-A suspension. Although the basic mechanical design is same as that of the standard GAS filter, the bottom filter is distinguishable from them owing to some additional functions that allows it to interface the upper stages with the payload assembly, not only in Type-A suspension systems but also in other types of the suspension systems.

One of the important roles of the bottom filter is to provide controllability at the lower point of the suspension with comparably large actuation range. The bottom filter is equipped with sensor-actuator-unified devices named *BF LVDT* (sometimes also referred to as BF damper) for six DoFs measurability and controllability of the bottom filter motion with respect to the ground (exactly speaking, the ground means the security structure or the vacuum chamber that surrounds the suspension chain and is fixed onto the ground). We can implement a larger actuation range on the bottom filter than the payload stages because the force noise introduced by the actuator has less impact on the test mass.

The BF LVDT allows us to actively damp the torsional motion of the single-wire suspension. In most cases, the torsional oscillation is driven by the translational seismic motions coupled through some paths such as imperfect centering of the suspension point due to inaccurate assemblings. Thereby, as its low-frequency mechanical resonances provide sufficient attenuation in the yaw direction, the torsional motions are less problematic in terms of displacement noise, which affects the interferometer's sensitivity. However, when the yaw motion is excited by kicks, it takes a long time (typically > 1000 seconds) to decay, leading to misalignment of the mirror and a decrease in the duty cycle of the interferometer. As the position of the bottom filter is far from the node of the fundamental yaw mode (the suspension point on the top GAS filter), the actuation on the bottom filter can apply effective damping. One remaining concern is that the bottom filter is in close contact with the node of the second yaw mode and thus less controllable in the Type-A suspension. We should address this problem creatively.

Other than the BF LVDT, the bottom filter has some additional functions. In Type-B and Type-Bp suspension, the next stages, namely intermediate mass (IM) and intermediate recoil mass (IRM), are suspended divergently from the bottom filter. The 6-DoFs relative position of the IM with respect to the IRM is monitored and actuated in order to provide a further controllability of the mirror's displacement and alignment. As the IM is connected with a single wire while the IRM is connected with three wires, a tilt of the bottom filter turns into a relative translation of the IM and IRM. To adjust the tilt, the bottom filter is equipped with a motorized weight on the cap. In addition, the static yaw position can be adjusted with a picomotor implemented on the keystone of the bottom filter. Thus, the bottom filter is not only one of the GAS filters but also an interface providing functions that adjust the payload conditions.

3.3.6   Cryogenic payload

The suspension systems in KAGRA have a part of the bottom stages called a *payload* that includes the core optics. The one in the Type-A suspension is called the *cryogenic payload*, as it is cooled down to operate at cryogenic temperatures. As the detailed design and characteristics (both vibratory and thermal) will be presented in a future dissertation, here we only provide a brief description of the cryogenic payload.

The cryogenic payload consists of four stages with a parallelized pair of chains. A computed-aided drawing of the cryogenic payload is shown in fig. 3.14. A disc-shaped stage called the *platform* (PF) is suspended from the bottom filter with a single maraging wire that is 3.3 m long. There are two chains suspended from the PF in parallel, namely the TM-chain and RM-chain. The first stage of the TM-chain is *marionette* (MN), a cross-shaped mass supported at a point close to its center of mass with a single maraging wire in order to have
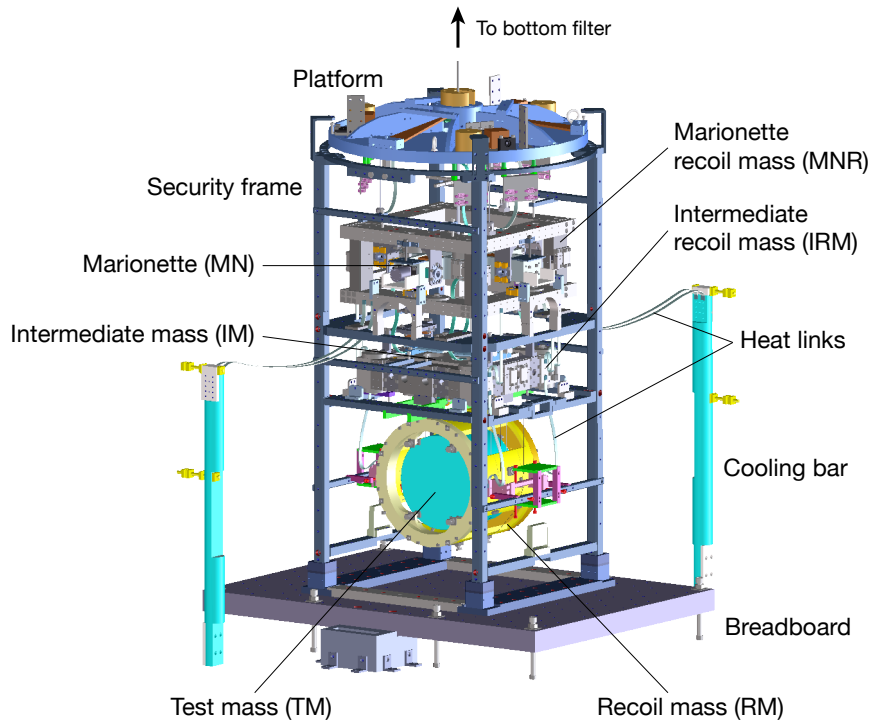
Fig. 3.14. An overview of the cryogenic payload.

low stiffnesses in its rotational DoFs. The next *intermediate mass* (IM) is the penultimate stage suspended from the four wires made of beryllium copper. Finally, the sapphire test mass (TM) is suspended with four sapphire fibers (35 cm long and 1.6 mm in diameter), each of which is hooked on a sapphire blade spring attached on the IM. The use of same material in the TM substrate and the fiber improves the thermal conductivity of the assembled system. These bottom three stages are accompanied with their reaction masses, providing controllability of relative position and alignment of the test mass independent of the seismic disturbances. There are permanent magnets on the TM-chain masses and coils on the RM-chain masses functioning as coil-magnet actuators to control each six differential DoFs of the MN-MNR and IM-IMR position, and three differential DoFs (namely longitudinal, pitch, and yaw) of the TM-RM position. Beside that, cryogenic photo-reflective sensors are additionally implemented in the configuration coincident with the coil-magnet actuators to produce local displacement of the TM-chain masses with respect to the RM-chain frames. In addition, static alignment control with respect to the ground structure can be performed with local angular sensors called optical levers.

The cooling of the cryogenic payload is based on the two paths of heat transfer, radiation cooling and conduction cooling. The whole of the cryogenic payload is housed in a double-layered cryostat, which is formed by a 8 K inner shield and 80 K outer shield. The surfaces of the cryostat, payload, and the security frame are treated with black coating for efficient
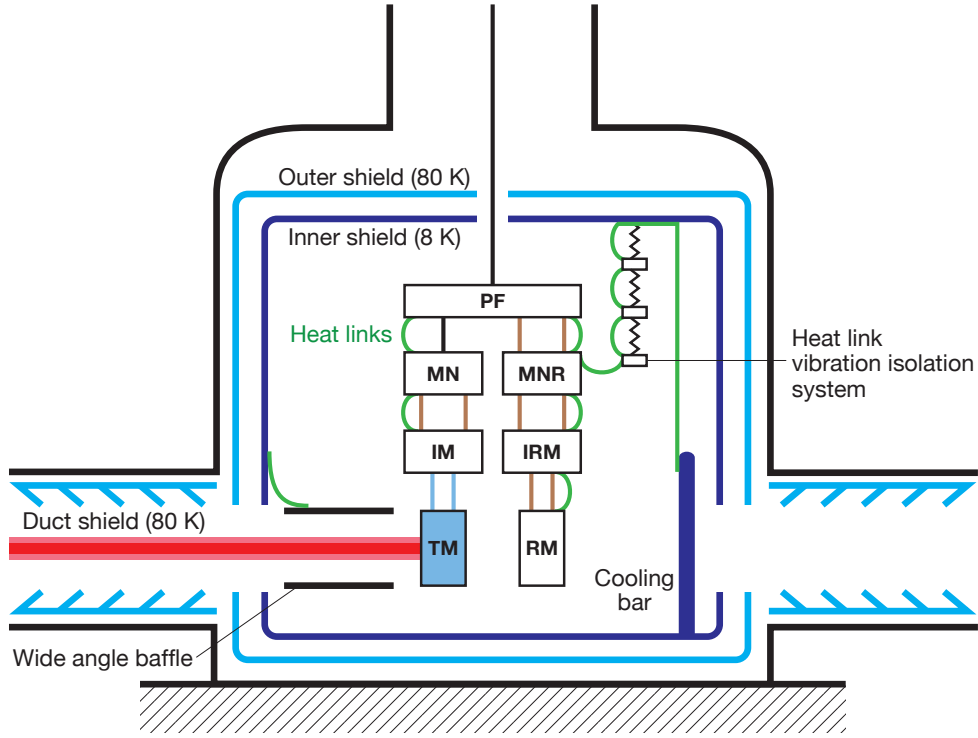
Fig. 3.15. Schematic diagram of the cooling system around the cryogenic payload.

radiation cooling. In addition, the stages of the cryogenic payload are connected to each other with high purity aluminum cables called *heat links* for conduction cooling. The absorbed heat on the test mass flows to the upper stages and is finally extracted to the cryostat structure through the heat links and cooling bars. As this mechanical conduction path could reintroduce additional vibrational disturbances to the isolated stages, a three-stage vibration isolation system is implemented on the cryostat to relay the heat links attached on the MNR. These cryogenic instruments are put under refrigeration with four units of pulse-tube cryocoolers. The cryocoolers have doubled vibration reduction stages whose first stage is connected to the 80 K outer shield and whose second stage is connected to the payload-cooling system and the 8 K inner shield. Although the shields of the cryostat have bore holes in front of the test mass so that the laser beam goes through, the holes can threaten the cooling time and attainable lowest temperature of the test mass by allowing intrusion of 300 K radiation from the room-temperature vacuum ducts. Therefore, 80 K duct shields are implemented inside the neighboring vacuum ducts to reduce the solid angle of the incoming 300 K radiation.

Fig. 3.16. Scheme of the LVDT position sensor

3.4 Sensors and actuators

3.4.1 Linear Variable Differential Transducer (LVDT)

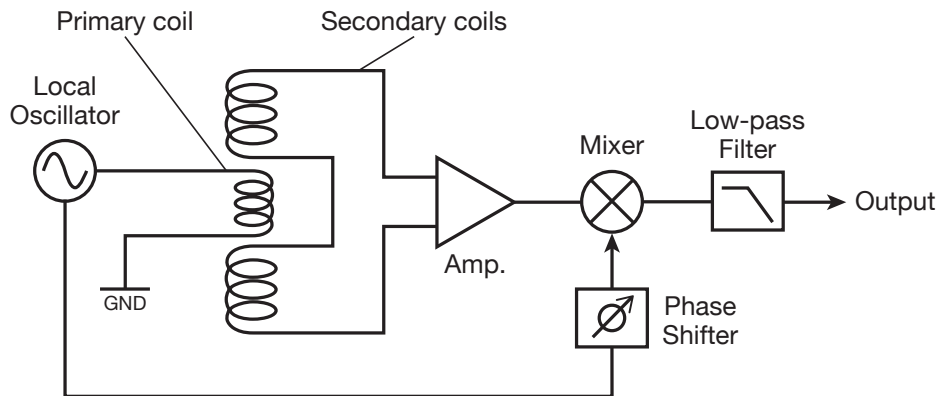The linear variable differential transducer (LVDT) is a relative displacement sensor using modulated magnetic field between inductively coupled coils [33]. Figure 3.16 shows the schematics of LVDT position sensing. The two kinds of coils, the primary coil and the secondary coils, are set coaxially aligned. One sends sinusoidal modulation signals of ~ 10 kHz to the primary coil, which produces an oscillating magnetic field around it. Then the secondary coils in the vicinity sense the variation in the magnetic field and generate induced voltages. As the two secondary coils are identical but counter-wound to each other, the induced voltage is canceled when the primary coil is placed at the center of the secondary coils. Thus, when the primary coil shifts from the center, the mutual inductance changes, and the differential induced voltages appear as net voltages at the subsequent readout. The net differential voltage is amplified and sent to the mixer which demodulates the oscillating voltage to obtain low-frequency ($\lesssim 100$ Hz) signals of the displacement of the primary coil.

One feature of the LVDT is good linear response to the displacement over large working range in axial direction. Our implementation has centimeters of its working range with resolution of sub-micrometers, specific values which depend on the applications. The KAGRA suspension systems have two types of LVDTs: a standard one used in the IP and GAS filters and a dedicated one used in the BF. As for the latter, it is designed so that the secondary coils of the LVDT is shared by actuator coil.
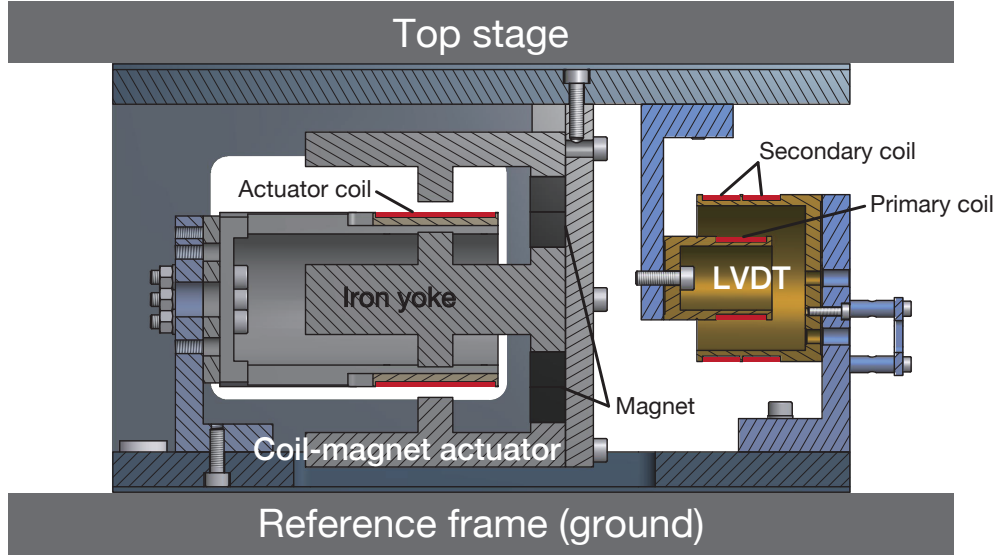
Fig. 3.17. Cross section of the unit of the LVDT and coil-magnet actuator mounted on the Pre-isolator.

3.4.2   Geophone

A geophone L-4C is a commercial high-sensitivity seismometer manufactured by Sercel. The geophone outputs voltages proportional to the velocity of its proof mass with respect to the housing. A proof mass with a weight of 1 kg is softly suspended with a spring and a damper with a resonant frequency of $\sim$ 1 Hz. A coil wound on the proof mass generates voltages induced by a permanent magnet attached on the housing. The geophone is a passive instrument that has a simple installation and can be easily maintained; it does not need any controls for the internal oscillator unlike the accelerometers used in TAMA-SAS.

The geophone has a 2nd-order high-pass frequency response below its resonant frequency. The frequency response of the geophone is

$$H_{\mathrm{geo}}(\omega) = \frac{G_{\mathrm{e}}\,\omega^2}{\omega_0^2 + 2i\eta\omega_0\omega - \omega^2} \; , \tag{3.6}$$

where G_{e} is the generator constant, η is the damping coefficient, ω and ω_0 are the angular frequency and angular resonant frequency, respectively. The conversion efficiency of the frame velocity to the output voltage is also plotted in fig. 3.18. Although the geophone has a flat response above the resonant frequency of 1 Hz, it shows frequency dependence proportional to f^2 at lower frequencies. The nominal parameters of the geophone are specified in table 3.7.

The output voltage from the geophone is amplified by a pre-amplifier circuit for better S/N ratio before being sent to the control system. The pre-amplifier circuit used in KAGRA suspension systems is designed in NIKHEF for the advanced Virgo. The first amplification
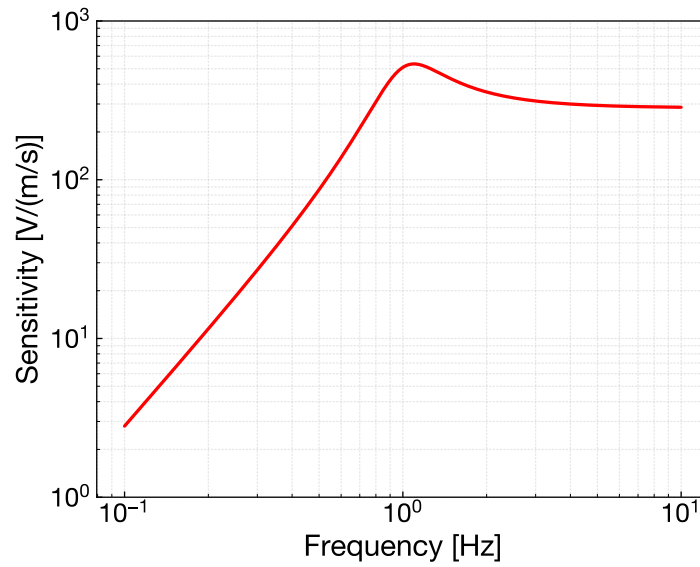
Fig. 3.18. Nominal frequency response of the L-4C geophone to ground velocity

Table 3.7. Nominal parameters of the geophone L-4C

Item	Value
Generator constant	276.8 V/(m/s)
Proof mass weight	1 kg
Resonant frequency	1 Hz
Damping coefficient	0.28
Coil resistance	5,500 Ω

stage with an operational amplifier CS3002, chosen owing to its low voltage noise feature, magnifies the signals by a factor of 374.5, then the second amplification stage gains the amplitude by 2.5 times while converting the signals into differential outputs. Thus, the pre-amplifier applies a 53.5 dB amplification to the equivalent differential signals.

On the other hand, the pre-amplifier also generates voltage fluctuation that limits the sensitivity of the geophone. A measured voltage noise spectrum with a breakdown into several noise sources' contributions is presented in [19]. The measurement indicates that the pre-amplifier noise is determined by Johnson noise at high frequencies (> 0.3 Hz), which is the thermal noise due to the resistance, and current noise at low frequencies (< 0.3 Hz) which comes from the operational amplifier.

Although the nominal parameters are given as summarized in table 3.7, the individual values of those parameters are calibrated by a simultaneous seismic vibration measurement with multiple types of seismometers. Additionally, we uses two units of Trillium Compact and one unit of Trillium 120QA seismometers produced by Nanometrics Inc., which are employed in KAGRA as environmental seismic monitors of the underground site. The Trillium

seismometer series have a flat response in the broadband region (0.01–10 Hz) and therefore exceed in simplicity of the calibration procedure.

The geophone and the pre-amplifier require in-air operation, while the suspension system is put in a vacuum environment. To secure the vacuum compatibility for the apparatus, we sealed them in vacuum pods made of stainless steel and kept the insides at atmospheric pressure. Air leakage from the vacuum pods was confirmed as negligible at least for several months in the prototype test of the Type-B suspension in NAOJ [19]. The relative position of the geophone inside the vacuum pod is fixed with rubber rings in order to prevent rattling on the internal surface, which will produce unwanted impulses in the readout signals. The damping effect of these rubber rings have been checked as negligible, indicating that the housing of the geophone and the vacuum pod can be regarded as a body.

3.4.3   Coil-magnet actuator

Suspension control in gravitational wave detectors requires vacuum-compatible and non-contacting actuators to apply force on the suspended bodies. A coil-magnet actuator is an instrument that meets such demands. One unit of the coil-magnet actuator consists of permanent dipole magnets and solenoid coils. It utilizes an electromagnetic force generated by the interaction between the static field of the permanent magnets and current sent to the coils.

The coil-magnet actuators used in the suspension systems can be classified into two types according to their working principle; voice-coil type and coaxial moving-magnet type. The voice-coil type actuator is a common implementation in audio speakers where the current in the coils generates a Lorentz force in a static magnetic field [34]. The lead wires of the coil are placed in a uniform magnetic field from the magnets shaped by high permeability iron yokes. As the permanent magnets are fixed on the reference frame, the Lorentz force received by the current becomes an actuation of the coil itself, or the suspended body which the coil is attached to. On the other hand, the coaxial moving-magnet type actuator has the permanent magnets and solenoid coils coaxially aligned to each other. The induced magnetic field of the coil attached to the reference frame applies an electromagnetic force on the permanent magnets glued on the suspended body. To mitigate dependence of the actuation force on the magnets' position, the magnets should be placed in a sufficiently uniform region of the induced magnetic field of the coil. All types of actuators implemented in the KAGRA suspensions are designed so that they have a sufficient linear region and large actuation capability. In the case of Type-A suspension, the actuators on the IP and GAS are the voice-coil type and the ones on the BF and payload are the coaxial type.

The design of actuators always involves a trade off between maximum actuation power and force noise. An actuator with a large actuation force will generate unwanted force noise

Table 3.8. Specification of the KAGRA coil drivers and assignment in the Type-A suspension [35]. The output resistances do not include the coil's impedance. The maximum current with the low power coil driver is 1.3 mA for the TM and 1.7 mA for the IM.

	OpAmp	Output resistance	Max current	Implemented on
Low power	AD8671	7.8 kΩ	1.3 mA or 1.7 mA	TM, IM
Modified low power	AD8671	1.4 kΩ	9.5 mA	MN
High power	OPA548	80 Ω	0.12 A	IP, GAS, BF

even in the presence of a small amount of electric fluctuation. In the case of suspension systems, the actuators located closer to the optics have a larger impact on the sensitivity of the interferometer. We therefore use three types of coil drivers to meet the available actuation range and force noise requirements, as specified in table 3.8. These coil drivers have different operational amplifiers for the current source and output resistance. As described in the following section, the actuation current sent to the coil is controlled with a digital system. The digital system has digital-to-analog converters (DACs) with an output range of ±10 V which limits the maximum actuation current to the coils and the coil driver does not determine the available current.

3.5 Digital signal processing

There are hundreds of thousands of channels that need to be managed during operation of KAGRA, even though the signals essential to GW detection correspond to a few channels. Moreover, achieving the outstanding sensitivity needed to observe GW signals needs systematic noise hunting where the people must survey an enormous number of channels to localize the sensitivity-limiting noise source. Even if we narrow our scope to a single suspension system, it has tens of signals to be processed, some of which are closed locally while some are interconnected with other suspension or control subsystems. These situations are complicated enough to motivate us to govern the entire observatory with computational instrumentation.

Digital control with computational machines provides easy accessibility and operability of the large system of the gravitational wave telescope. Use of a digital control system enables us to acquire the following features.

- Real-time remote control of the instruments

- Easy management of the multiple degrees-of-freedom control

- Low noise control by quantization

- Data acquisition infrastructure

Table 3.9. Specification of the KAGRA digital system.

Item	Value
Sampling rate	2048 Hz (decimated from 65536 Hz)
Through delay	80 μs
ADC/DAC resolution	16 bit (2^{16} = 65536 digital counts)
ADC voltage range	$\pm$20 V (1 count = 6.104×10^{-4} V)
DAC voltage range	$\pm$10 V (1 count = 3.052×10^{-4} V)
ADC noise level	3 μV/Hz$^{1/2}$ ($> 10\,$Hz)
DAC noise level	2 μV/Hz$^{1/2}$ ($> 10\,$Hz)
Number of ADC channels	32 ch. differential inputs / 1 ADC board
Number of DAC channels	16 ch. differential outputs / 1 DAC board

- Automated operation of the interferometer

The detailed specification of the KAGRA digital control system is summarized in [19].

Chapter 4

Control design

In this chapter, we present a concept of suspension control used in KAGRA. Design of the control system utilizes system modeling

4.1 System modeling

Modeling of the suspension system is an important part of understanding its dynamic characteristics and also a powerful tool to design the control strategies. Here we start with 3-dimensional rigid-body modeling, whereby the internal dynamics of the suspended mass are ignored and focus is placed on the modes only associated with the coupled multi-degrees-of-freedom vibration of the rigid components. This assumption is generally accurate when studying the low-frequency ($\lesssim 10$ Hz) dynamics of such a mechanical system. Moreover, it is also combined with the frequency region of interest where the control will be applied. This simple model can be used to solve the problem of the control design.

Control problems of the suspension systems are addressed by the framework of linear control theory. Although the full dynamics of the mechanical oscillator includes non-linearity in general, the linear approximation stays valid as the suspension system will be operated in a small region around its equilibrium point. We have another naive reason to restrict the system to be linear that is to utilize well-studied tools of linear control theory developed in the long history of the control engineering. Modeling and control problems of a non-linear system make things much complicated, despite the fact that we are hardly interested in such non-linear behavior.

4.1.1 Formulation of 3D rigid-body dynamics

In this study, a 3D rigid-body modeling toolkit coded in Mathematica® is used. It was initially developed by M. Barton for the LIGO suspensions and packaged into GUI software by T. Sekiguchi [36, 37]. Here the concept of 3D rigid-body modeling is briefly described.

The formulation of the dynamic characteristics of multi-DoFs mechanical oscillators is based on the linearized equation of motion. By expressing a set of positions and velocities of the system (= component masses) respectively as $\boldsymbol{x}$ and $\dot{\boldsymbol{x}}$, the equation of motion can be derived through the following steps.

1. Calculate the potential energy $U(\boldsymbol{x})$, dissipation function $R(\boldsymbol{x}, \dot{\boldsymbol{x}})$, and kinetic energy $K(\boldsymbol{x}, \dot{\boldsymbol{x}})$ of the system.

2. Minimize the potential energy to find the equilibrium point $\boldsymbol{x}_{\mathrm{eq}}$.

3. Differentiate the potential energy with respect to the pairs of coordinates of the equilibrium point to derive the *stiffness matrix* $\boldsymbol{K}$,

$$K_{ij} = \left. \frac{\partial^2 U(\boldsymbol{x})}{\partial x_i \partial x_j} \right|_{\boldsymbol{x}=\boldsymbol{x}_{\mathrm{eq}}} \tag{4.1}$$

4. In the same manner, differentiate the dissipation function and the kinetic energy with respect to pairs of the coordinate velocity at equilibrium to derive the *damping matrix* $\boldsymbol{G}$ and the *mass matrix* $\boldsymbol{M}$,

$$G_{ij} = \left. \frac{\partial^2 R(\boldsymbol{x}, \dot{\boldsymbol{x}})}{\partial x_i \partial x_j} \right|_{\boldsymbol{x}=\boldsymbol{x}_{\mathrm{eq}}} \tag{4.2}$$

$$M_{ij} = \left. \frac{\partial^2 T(\boldsymbol{x}, \dot{\boldsymbol{x}})}{\partial x_i \partial x_j} \right|_{\boldsymbol{x}=\boldsymbol{x}_{\mathrm{eq}}} \tag{4.3}$$

5. Finally the linearized equation of motion is written with the derived matrices as

$$\boldsymbol{M}\ddot{\boldsymbol{x}} + \boldsymbol{G}\dot{\boldsymbol{x}} + \boldsymbol{K}(\boldsymbol{x} - \boldsymbol{x}_{\mathrm{eq}}) = \boldsymbol{0} \,. \tag{4.4}$$

In this formulation, each suspended body has motions in 6 DoFs except for the IP stage, which has only three horizontal DoFs, namely longitudinal, transverse, and yaw directions. The GAS is treated as a 1-dimensional vertical spring, taking into account the saturation of attenuation performance caused by the imperfect cancellation of the center-of-percussion effect. We regard the suspension wires as massless springs with torsional elasticity and load elongation, neglecting their violin modes. To treat dissipation due to the internal friction of the elastic material, the spring constants of the vertical springs and wires have imaginary parts representing finite loss angles, which are assumed to be constant over the entire frequency region (equivalent to the structural damping process).

4.1.2   State-space representation

The techniques referred to in the control theory can be applied to systems whose time evolution can be described by a series of linear, time-invariant [1], first-order ordinary differential equations. When the state of the system can be determined by a set of variables $\boldsymbol{x}$, called *state variables*, its time evolution will follow the equation,

$$\dot{\boldsymbol{x}}(t) = \boldsymbol{A}\boldsymbol{x}(t) \,, \tag{4.5}$$

where the matrix $\boldsymbol{A}$, which is called *system matrix*, characterizes the dynamics of the state with dimension of $n \times n$ where n is the number of states corresponding the length of the vector $\boldsymbol{x}$. In this case, the system is said to be of order n. To incorporate the system with the available control input, one can extend the equation of state so as to include the response to a set of inputs $\boldsymbol{u}$ via a matrix $\boldsymbol{B}$ called *input matrix*. Then the equation of state of the system becomes

$$\dot{\boldsymbol{x}}(t) = \boldsymbol{A}\boldsymbol{x}(t) + \boldsymbol{B}\boldsymbol{u}(t) \,, \tag{4.6}$$

which associates the state of the system with the given input. When the input vector $\boldsymbol{u}$ has a dimension of m, the input matrix $\boldsymbol{B}$ must have a dimension of $n \times m$, the same number of rows as those of the state variables, and same number of columns as that of the input.

On the other hand, the output from the system $\boldsymbol{y}$ will be a superposition of the system's state projected via the *output matrix* $\boldsymbol{C}$ and direct couplings from the input via the *feedthrough matrix* $\boldsymbol{D}$, such that

$$\boldsymbol{y}(t) = \boldsymbol{C}\boldsymbol{x}(t) + \boldsymbol{D}\boldsymbol{u}(t) \,. \tag{4.7}$$

The combination of these equations that can uniquely determine the dynamics of the system (often also referred to as *plant*) is known as *state-space representation*. It is summarized as

$$\begin{aligned} \dot{\boldsymbol{x}}(t) &= \boldsymbol{A}\boldsymbol{x}(t) + \boldsymbol{B}\boldsymbol{u}(t) \\ \boldsymbol{y}(t) &= \boldsymbol{C}\boldsymbol{x}(t) + \boldsymbol{D}\boldsymbol{u}(t) \end{aligned} \,. \tag{4.8}$$

To derive the suspension's equation of motion for the state-space representation one more step needs to be performed. While the equation of motion for the suspension system is a second-order differential equation, one should introduce an additional first-order differential equation, $\boldsymbol{v} = \dot{\boldsymbol{x}}$, so that the equation of motion can be written in the form of a state-space model. Hence, by setting the state variables as $(\boldsymbol{x},\, \boldsymbol{v})$, we can obtain the state-space model

---

[1] Here "time-invariant" implies that the outputs of the system given arbitrary inputs do not depend on the absolute time. In other words, the time-invariant system must produce the same outputs with respect to the given inputs.

of the suspension system from eq. (4.4), which is written as

$$\frac{\mathrm{d}}{\mathrm{d}t} \begin{bmatrix} \boldsymbol{x}(t) \\ \boldsymbol{v}(t) \end{bmatrix} = \begin{bmatrix} \boldsymbol{O} & \boldsymbol{I} \\ -\boldsymbol{M}^{-1}\boldsymbol{K} & -\boldsymbol{M}^{-1}\boldsymbol{G} \end{bmatrix} \begin{bmatrix} \boldsymbol{x}(t) \\ \boldsymbol{v}(t) \end{bmatrix} + \boldsymbol{B}\boldsymbol{u}(t) \qquad (4.9)$$

The equation of motion determines only the components of the system matrix $\boldsymbol{A}$. The other matrices will be designed depending on the configuration of the sensors and actuators.

State-space representations allow researchers to describe the dynamics of the system as a time evolution of the state variables even if the system has multi-inputs and multi-outputs (MIMO). In conventional frequency domain analysis, the system is described by means of transfer functions that project the input onto the output. The transfer function is a useful tool for expressing a single-input-single-output (SISO) system.

4.2   Control topology

The KAGRA control system is composed of a set of parallelized single-input-single-output (SISO) feedback loops. The policy of the suspension control in KAGRA is to process the displacement signals on the Cartesian basis defined in section 2.3. The Cartesian signals can be obtained from the sensor readouts in their disposed bases through the matrix operation, after which the generated feedback signals in Cartesian coordinates are distributed to the real actuators to produce feedback forces in a proper direction.

The control topology for the Type-A suspension is illustrated in fig. 4.1. There are mainly four loops in the local control of the Type-A suspension. The IP control provides mode damping of the horizontal motions and DC positioning of the whole suspension chain. The GAS control deals with resonant mode damping and stabilization of the DC drift of the keystone's height. The BF control allows us to apply torsion mode damping on the single-wire chain, which is unfeasible in the IP control. Finally, the payload control addresses damping of the internal mode inside the payload and alignment control of the mirror. As the actuators in the payload have been designed so that the lower stage actuators, compared to the higher stage actuators, have a lower ability to mitigate force noise coupling, the payload control adopts a scheme of handing over the feedback signals to the upper stages with more powerful actuator; this process is called hierarchical control [38].

In the control simulation, the dynamics of the suspension system with multi-inputs and multi-outputs are represented as a state-space model. The inputs and outputs of the model are reshaped so as to correspond to a practical setup, such as the differential I/O, for the GAS sensors and actuators.
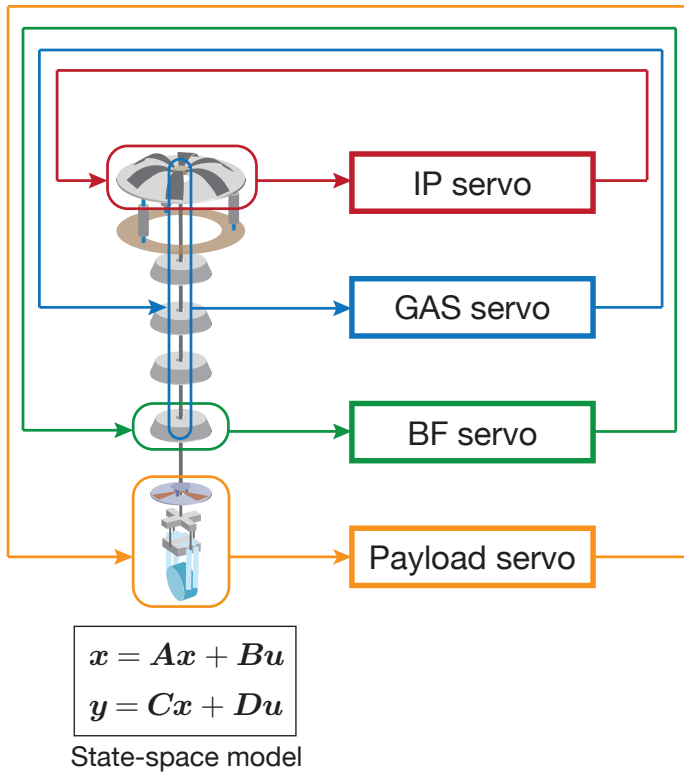
Fig. 4.1. Block diagram of the local control of the Type-A suspension. In the model calculations in this chapter, the dynamics of the suspension system are represented as a state-space model with properly-arranged inputs and outputs. Here the global and hierarchical paths are omitted.

4.3 1/e decay time reduction

The most important topic in tower control is mode damping of the mechanical resonances. As the low-frequency oscillators are implemented at the tower stages, the eigenmodes with large amplitude in the tower stages' DoFs tend to have relatively low resonant frequencies and thus a large impact on the RMS residual motion of the mirror.

The performance of mode damping is evaluated as the exponential decay time for each eigenmode, as required in the calm-down phase. The simulated exponential decay time for the mechanical eigenmodes of the Type-A suspension is shown in fig. 4.2. While the Type-A suspension has 75 eigenmodes in total, the number of modes whose shapes are mainly distributed over the tower stages is 36 and that whose shapes are primarily contributed by the payload stages are 39. In absence of any control, the eigenmodes from the tower stages are distributed in the lower-left region below $\sim 1\,\mathrm{Hz}$ with low Q-factors. In contrast, the eigenmodes from the payload stages have higher resonant frequencies with higher Q-factors that are mapped in the upper-right region in fig. 4.2. In practice, the quality of the mechanical resonances in the real suspension is generally limited by the actual installed setup such as the clamping of the suspension wires. Hence the model predictions of the quality factor or the 1/e decay time often lack the precision to demonstrate the real system. Nevertheless, the following simulation of the damping control helps us to estimate achievable exponential decay times as the servo design results in suppression of the modal amplitude that relies on
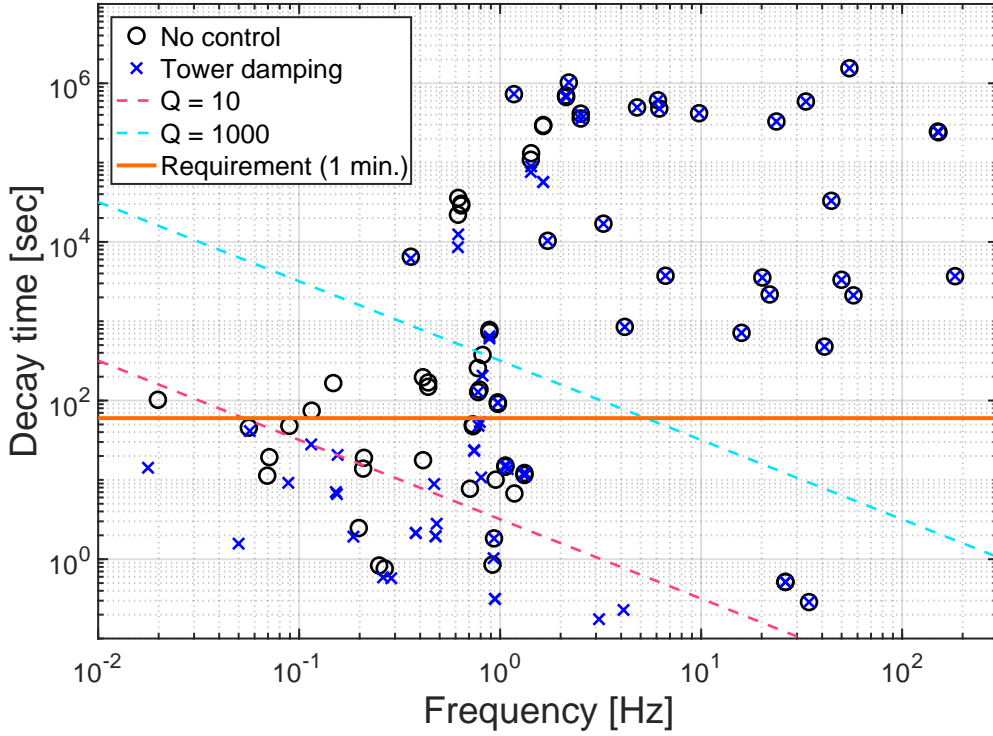
Fig. 4.2. Predicted 1/e decay time versus the mode frequencies of the mechanical resonances in the Type-A suspension. In the case which the tower damping control is engaged, the principal low-frequency modes are successfully damped so that their decay times are less than 60 s.

the intrinsic high-Q peak of the mechanical resonances.

We can see the reduction performance of the 1/e decay times with tower damping control in fig. 4.2. In this type of damping control, servo filters are engaged in the IP loops for all 3 DoFs, one GAS loop at F0, and BF loops in three rotational DoFs. The servo filters are designed as differential filters at the peak frequencies ($\lesssim 1\,\mathrm{Hz}$) generating feedback signals proportional to the velocity of the suspended stage that act as low-pass filters with a couple of poles in the 1–5 Hz range to reject the sensor noise reintroduction at high frequencies. Note that the damping control in the payload's DoFs is not discussed here because it will be addressed in a thesis on the cryogenic payload development[2]. According to the simulation, most of the eigenmodes coming from the tower stages can be successfully damped, and their exponential decay times are reduced to less than 1 min. Meanwhile, the decay time of the eigenmodes originating from the payload almost remain unaffected by the tower control loops. This fact illustrates the significance of the performance test of the Type-A tower alone independently of the cryogenic payload. However, some of the tower modes that are plotted

---

[2] This thesis will be published in the near future.

in the range of 0.5–1 Hz seem unrealistic for achieving a decay time shorter than 1 min. Although these modes are identified as the DoFs corresponding to the tilts of the standard GAS filters, the Type-A suspension is unfortunately not equipped with sensing or actuating devices for these DoFs. Nonetheless, as it is expected that the modes in these rotational DoFs will not have substantial impact on the mirror's residual motions, the exponential decay time can be left as they are if it can be confirmed that their couplings to the mirror motion are negligibly small.

4.4 Modal damping control

Modal damping is a convenient way to decouple vibration into the normal modes of the system so that they can be damped independently. The control problems of a high dimensional system with many coupled DoFs can be simplified as a set of single DoF control problems, thereby minimizing the complexity of the compensator design. As a result, it is relatively easy to find an optimal trade-off between damping performance and noise contamination in the damping control for each mode [39, 40].

In this work, modal damping is applied to the vertical modes of the Type-A suspension that originate from the chain of GAS filters. The advantage of these vertical DoFs is availability of many sensors and actuators distributed over most stages associated with the mode shapes. As the resonant frequencies of the coupled GAS modes are localized in the range of about 0.1–1 Hz due to the softness of GAS, one should place importance on the damping of those soft modes.

4.4.1 Modal decomposition

Modal damping handles vibration as displacement signals in *modal coordinates* and feedbacks them via controllers designed for each mode. The matrix that transforms Cartesian to modal coordinates can be obtained using the mass matrix $\boldsymbol{M}$ and the stiffness matrix $\boldsymbol{K}$. Assuming the system has no damping, the linearized equation of motion in eq. (4.4) is written in the Fourier domain as follows.

$$(-\omega^2 \boldsymbol{M} + \boldsymbol{K})\tilde{\boldsymbol{X}}(\omega) = \boldsymbol{0} \tag{4.10}$$

This equation has the form of an eigenvalue problem. By replacing the angular frequency as $\lambda = \omega^2$ and the displacement vector as $\boldsymbol{\phi} = \tilde{\boldsymbol{X}}$, the equation becomes

$$(\boldsymbol{K} - \lambda \boldsymbol{M})\boldsymbol{\phi} = \boldsymbol{0} \,. \tag{4.11}$$

Thus a set of eigenvalues λ and eigenvectors $\boldsymbol{\phi}$ of the system is obtained. As $\boldsymbol{M}$ is positive-definite and $\boldsymbol{K}$ is non-negative definite, these eigenvectors are orthogonal and thus can become

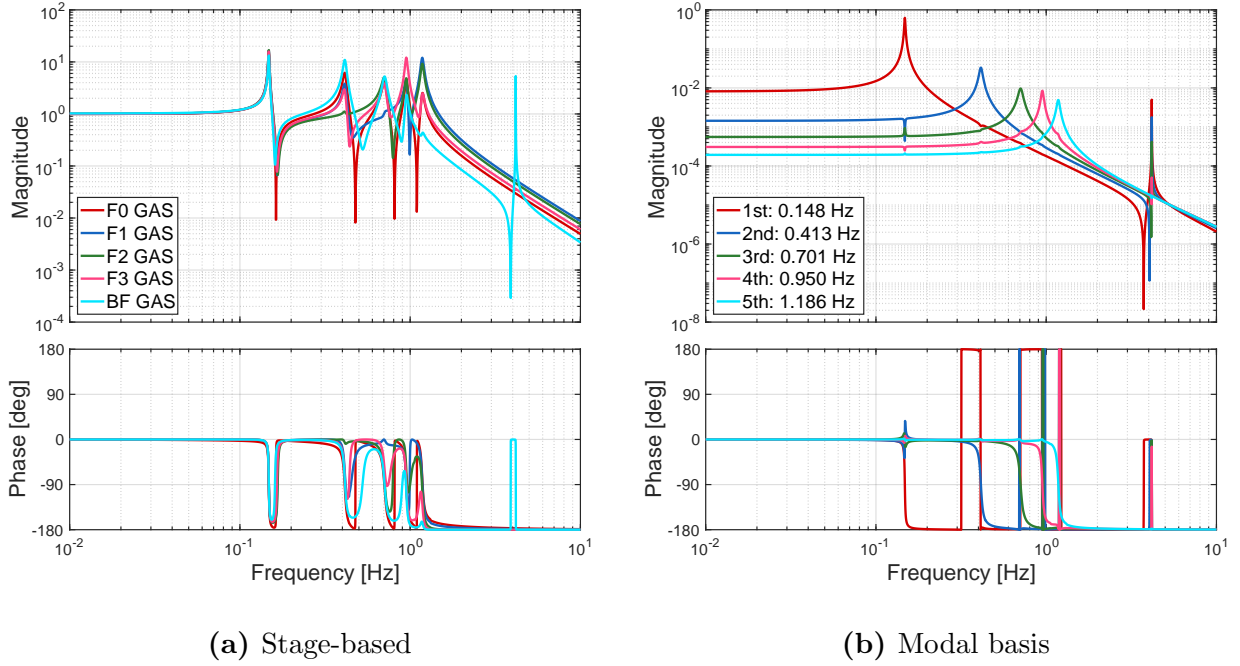**(a)** Stage-based   **(b)** Modal basis

Fig. 4.3. Calculated transfer functions of the GAS stages in the vertical direction. Every stage-based (LVDT- and actuator-wise) response in **(a)** has a fraction of all normal modes as a series of resonant peaks, while on the modal basis in **(b)**, the normal modes are separated into responses of a single second-order system.

the basis of coordinates called modal coordinate. The modal coordinate and the conventional Cartesian coordinates are related by the following equation:

$$\boldsymbol{x}(t) = \boldsymbol{\Phi}\,\boldsymbol{\eta}(t)\,, \tag{4.12}$$

$$\boldsymbol{\Phi} \equiv [\boldsymbol{\phi}_1\ \boldsymbol{\phi}_2\ \cdots\ \boldsymbol{\phi}_N]\,. \tag{4.13}$$

Here $\boldsymbol{\eta}(t)$ is a vector that represents the position of the system in modal coordinates. The matrix $\boldsymbol{\Phi}$ is the transformation matrix whose elements are the column-wise eigenvectors arranged along a row from low to high order modes. Using the matrix $\boldsymbol{\Phi}$, the sensor signals can be converted to displacements in modal coordinates (called *modal displacement*) that indicate the amplitude of a specific mode in the system. Conversely, the feedback signals that damp the specific mode are distributed to the actuators via the matrix $\boldsymbol{\Phi}$ suited for the mode shape.

The calculated diagonal transfer functions of the GAS vertical DoFs are shown in fig. 4.3, where they are compared with those in unit-wise (LVDT- and actuator-wise) and modal bases. Every unit-wise response is a mixture of all the normal modes that are shown as a series of resonant peaks in fig. 4.3a. On the other hand, the decoupled modal responses behave as a single second-order low-pass system like a simple harmonic oscillator, as shown in fig. 4.3b. Note that the norms of the eigenmode vectors used in the transformation matrix $\boldsymbol{\Phi}$ are
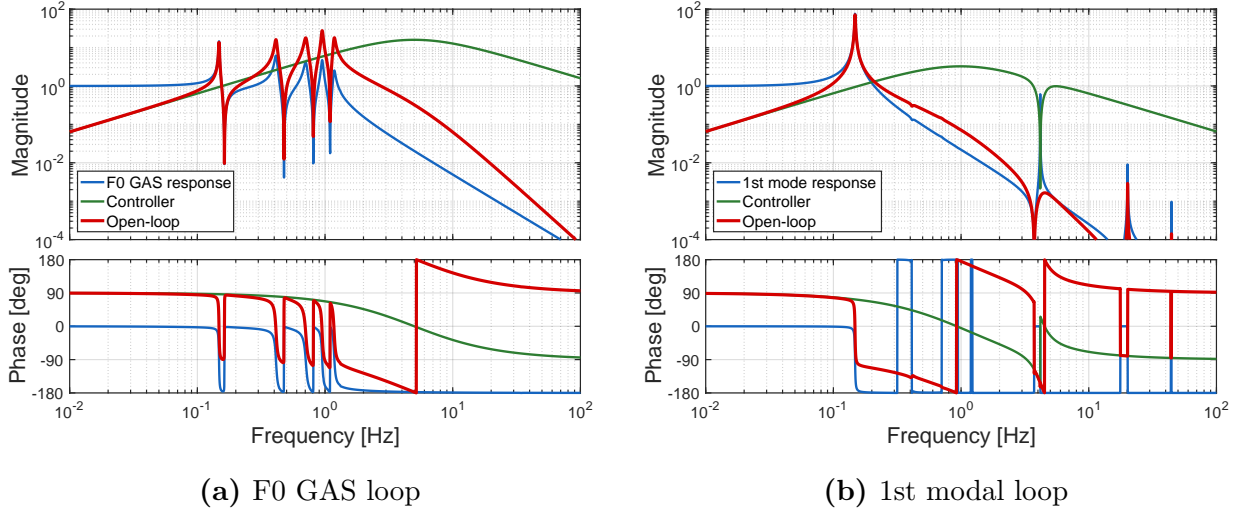
(a) F0 GAS loop **(b)** 1st modal loop

Fig. 4.4. Examples of the filter design and its open-loop transfer function for the damping control of the GAS vertical modes.

normalized by their modal mass m_r so that $\phi_r^\mathsf{T} M \phi_r = m_r$ is satisfied for the r-th order mode. The large resonance that appears at 4.17 Hz comes from the internal mode of the cryogenic payload that was ignored in the modal decomposition. Although there remains a small amount of deviation from an ideal second-order response in the modal responses due to the accuracy of the mode shape calculation, it is unlikely to be an issue in terms of controller design because its phase distortion above the mode frequency less than 3 deg. In practice, the accuracy of modal decomposition can be improved by diagonalization of the sensing and driving matrices.

4.4.2 Damping control performance

To see the damping performance of the modal control, we simulated the exponential decay time reduction of the vertical modes of the Type-A suspension with a simply-minded filter design. As the damping control aims to suppress the vibration amplification at the mechanical resonances, one should design the servo filter so that the resulting open-loop transfer function has a gain of more than unity at the resonant peaks. The basic strategy of the filter design here is placing one zero at a low frequency and several poles at a high frequency to cover the frequency region of the resonances. Such a zero-pole placement forms a differential controller at the peak frequencies, whereas it cuts off the high-frequency signals to prevent noise injection into the control loop. In this study, only the single-input-single-output (SISO) controllers are taken into account.

The examples of the filter design and their open-loop transfer functions are shown in fig. 4.4. In the stages-based control design, as almost all the mechanical resonances appear
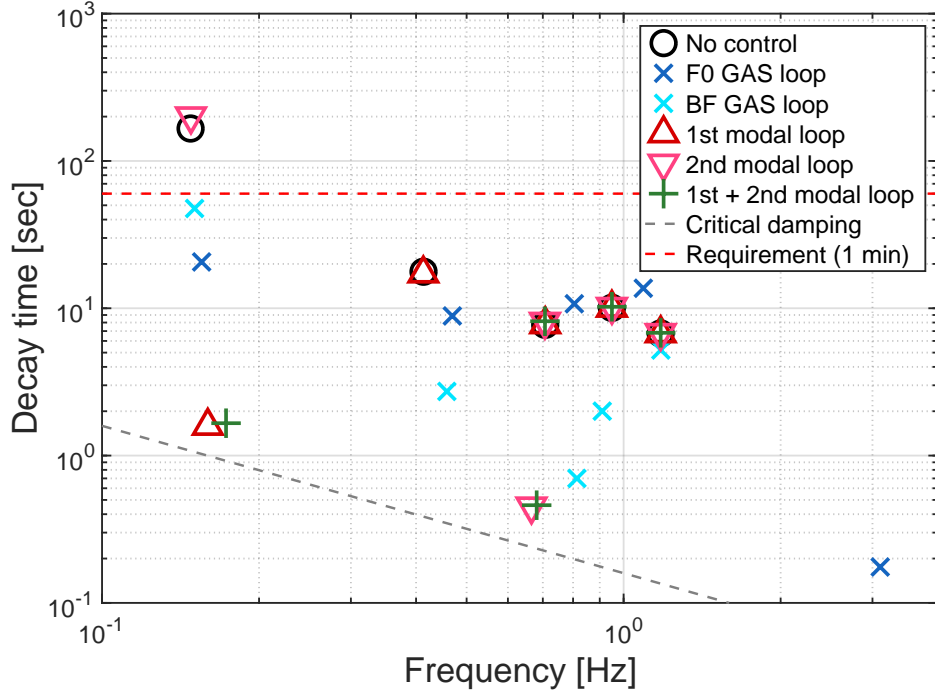
Fig. 4.5. Simulated exponential decay time for the vertical modes in the Type-A suspension. Only the lowest five modes that originate from the GAS structure are plotted.

within a decade of the frequency region, it is difficult to remove the higher order modes from the control and to lower the control bandwidth. On the other hand, the controller design in the modal basis is much less complicated owing to the absence of the following higher order modes. Although some modes that originate from the payload remain visible in the modal response, they can be easily rejected with notch filters due to their high quality factors and large differences in frequency from the lower-order modes of interest. In the examples of the filter design, the bandwidth of the damping control is 1.1 Hz in the F0 stage-based loop and 0.23 Hz in the 1st modal loop. The ignored higher-order mode at 4.17 Hz in fig. 4.4b, which is due to the blade spring at the platform stage, is rejected by a notch filter with a Q-factor of 3.

The results of exponential decay time reduction with various damping controls is shown in fig. 4.5. Here we simulated five setups of the control loop: two stage-based loops, two modal loops, and one combined modal loop. The F0 GAS and BF GAS loops are conventionally used to control the vertical modes using the sensor signal from a specific stage, which is fed back to the actuator at the same stage. These F0 and BF loops are chosen as benchmarks of the conventional scheme because they are the top and bottom stages, respectively, in the tower part. The 1st modal and 2nd modal loops are the novel schemes proposed in this study. To check the selectivity of modal feedback to damp the specific mode, a setup with two closed

modal loops is also investigated. All the controllers simulated here have been designed in a manner similar to those described in the previous paragraph.

In a natural state without any control, it is predicted that only the 1st mode has a long decay time in excess of the requirement of 60 s. When a stage-based loop is closed, as its open-loop gain is more than unity at every resonant peak, the decay times for all the eigenmodes are reduced, and the markers are replaced in fig. 4.5. However, the reduced decay time for each mode depends on the mode's shape, and thus one must design the control topology to achieve a higher damping performance on a specific mode. On the other hand, the modal damping loops exhibit large decay time reduction in each specific mode, slightly interfering with the other modes' properties. The performance in the setup of two closed modal loops seems consistent with the setups of each single modal loop closed. In addition, the simplified system response allows us to easily design a controller achieving damping performance close to the critical damping. It can be shown that the information about a specific mode contained in the sensor signals is effectively used to suppress the vibration in the mode. Thus the modal control scheme can maximize the effective sensor range and actuator range. As the control of the suspension system deals with vibrations in many coupled DoFs, modal damping is useful not only for the vertical modes but also other complicated DoFs, such as in payload control with longitudinal-pitch couplings.

Chapter 5

Performance test of Type-A tower

In this chapter, the experimental performance test of the type-A suspension is presented. Even before the payload is integrated, it is worthwhile to test the performance of the tower part of the Type-A suspension as the tower part contains important features of the low-frequency oscillator, which determines a major fraction of the vibration isolation performance. Therefore, a description of the experimental setup is described in section 5.1. In the following section 5.2, the measurement results for the system characterization in the frequency domain are presented. Although all of the characteristics of interest could not be tested, the functionality of torsion mode damping in the yaw direction and modal damping for the GAS vertical modes were performed and are reported in section 5.3 and section 5.4, respectively. In addition, we performed a vibration isolation ratio measurement in the period of the test operation of the cryogenic Michelson interferometer, where the installed Type-A tower is integrated with the actual cryogenic payload. The result of the vibration isolation ratio measurement is finally presented in section 5.5.

5.1 Experimental setup

The performance test described in this chapter includes the results yielded from two different setups, the Type-A tower and full Type-A suspension. Owing to the schedule of the KAGRA, the data for the performance test were taken when the KAGRA was undergoing an upgrade and the hardware installation of the Type-A suspension was ongoing yet to be incorporated into the interferometer. This study focused on the performances of the vibration isolation and controllability possessed by the tower part of the Type-A suspension.

The two different setups for the performance test of the Type-A suspension are depicted in fig. 5.1. The clear difference in these setups is the existence of the cryogenic payload, the bottom four stages. In the setup of the Type-A tower, a dummy payload is suspended instead of the cryogenic payload from the bottom filter. As described in chapter 5, the weight of the

105

Table 5.1. Difference between the Type-A tower and full Type-A setup.

	Tower	Full
Stages	6	9
Height [m]	9.8	13.5
Eigenmodes	39	75
	Dummy payload	Cryogenic payload
Sensors	geophone L-4C	photoreflective sensor
		optical lever
		optical length sensor
Actuator	none	coil-magnet actuator

dummy payload is adjusted to approximately coincide with that of the actual payload, while the length of the suspension wire for the dummy payload is 15 cm, which is much shorter than the actual maraging wire of 3.3 m because of the spatial constraint inside the vacuum chamber. Therefore, the Type-A tower is more than a little different from the full suspension geometrically.

Most of the tests described in this chapter were performed with the setup of the Type-A tower before integration with the cryogenic payload. Even without the actual payload, the Type-A tower can demonstrate the performance of vibration isolation and functionality of control. Although the dynamic characteristics of the system differ from those of the full configuration owing to the difference in mechanical geometry. The similarity and differences between these setups can be visualized in the eigenmode property shown in fig. 5.2. While the full Type-A suspension has a total of 75 eigenmodes, the tower has 39 eigenmodes, some of which are peculiar to the tower setup, such as ones associated with the tilt of the DP. We can see that the tower part includes most of the low-frequency eigenmodes common to both setups. As

- the lowness of the eigenmode frequencies determines the seismic attenuation performance in a given frequency region,

- the low-frequency eigenmodes have a large impact on the residual RMS of the mirror fluctuation,

the characterization of the mechanical dynamics and demonstration of the damping control for the Type-A tower can be regarded as equivalent to those of the full Type-A suspension. Moreover, as the tower or payload part is still a complicated multi-stage pendulum, it is necessary to examine each part alone from the view point of fault localization.
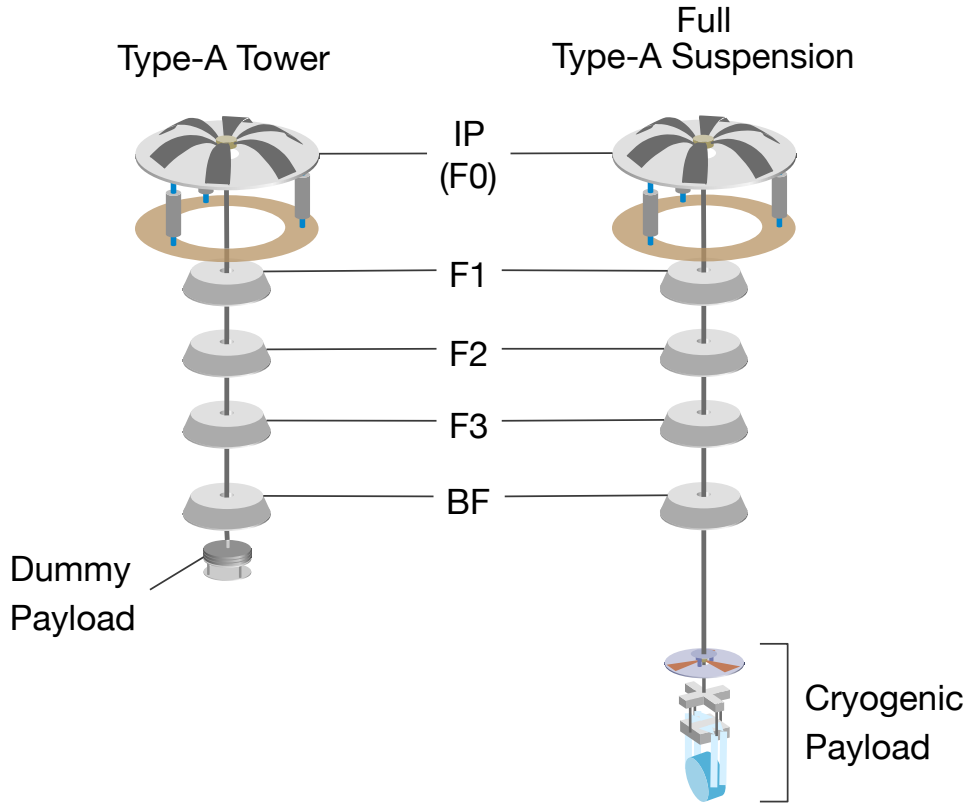
Fig. 5.1. An illustration of two setups for the performance test of Type-A suspension.

5.2 System characterization

The characteristics of the installed Type-A tower are determined by the accuracy of the mechanical assembling, which contains adjustments of the load or balance, geometrical positioning, and so many other factors. In this section, the oscillatory behavior of the installed system was identified by measuring the mechanical transfer functions and spectra in a stationary state for the controllable and observable DoFs. The measured results were compared with predictions of the 3D rigid-body model having the same design parameters, and their agreement with the predictions was determined.

5.2.1 Diagonal transfer functions

The mechanical responses of the suspension system are described in terms of force-displacement transfer functions of the suspended masses in the frequency domain. For this purpose, virtual sensors and actuators based on the Cartesian coordinate system were constructed in the digital system with linear combinations of real sensors and actuators.

The measurement was performed by injecting excitation from a virtual actuator in a certain DoF and taking the resulting displacements measured with the virtual sensors. We
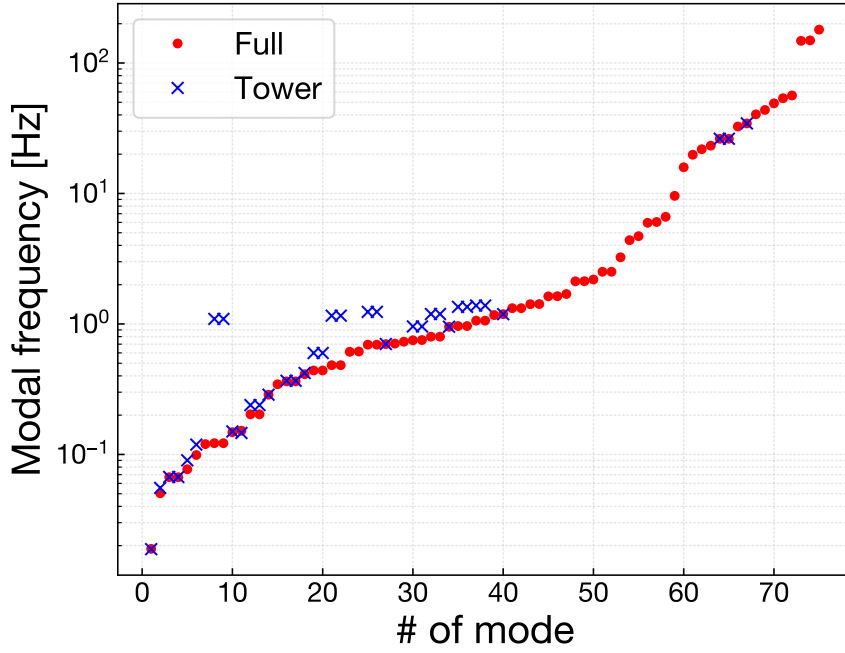
Fig. 5.2. Comparison of modal frequencies of the full configuration and the tower part of the Type-A suspension. The mode index of the tower is arranged so that the shapes of its modes are similar to those of the full suspension.

used two types of excitation signals: broadband Gaussian injection, which can excite the system in a wide frequency range, and monochromatic sinusoidal injection, which sweeps over the frequency range of interest. The former has a short measurement time, allows results for the entire frequency region to be obtained quickly, and has comparatively higher resolution of the sampled frequency points. The latter is superior in the S/N ratio of the measurement as it takes sampled data points one by one but instead needs a long measurement time. We used the Gaussian injection in most measurements where vibration in the DoF is sufficiently excited due to the softness of the spring or the strength of the actuation power. Only some DoFs, especially those at the bottom filter, are measured with the swept-sine excitation.

Note that all the DoFs of the stages and all the eigenmodes are not sufficiently controllable and observable owing to the configurations of the sensors and actuators.

Horizontal DoFs at inverted pendulum

The inverted-pendulum (IP) stage can move in three horizontal DoFs, namely the longitudinal, transverse, and yaw directions. The measured diagonal transfer functions in the horizontal DoFs of the IP are shown in fig. 5.3. The gross features of the transfer functions are consistent with the model prediction for all three DoFs. Nevertheless, several discrepancies between the measurement and model are recognized. The discrepancies and possible

explanations are detailed below.

- In the longitudinal and transverse directions, the measured resonant frequency of the first mode deviates from the model's value. The model predicts that the resonant frequency is 67.3 mHz, while in the measurement, it is 58.6 mHz in the longitudinal direction and 65.7 mHz in the transverse direction. These values are fall within 13% of the model's value. The deviation can be explained by assuming asymmetry in stiffness of the IP legs. If we consider a nominal value of 67 mHz for the resonant frequency of the IP stage, the installed system possesses sufficient low-frequency resonance for the first eigenmode. Note that the model does not take the asymmetry into account.

- A small bump appears at 0.4 Hz in the longitudinal and transverse transfer functions. This bump can be considered as a coupling from a resonance in the yaw direction.

- In the longitudinal and transverse transfer functions, the mismatch between the measurement and model in the frequency range from 0.7 Hz to 1.1 Hz reflects unmodeled dispersion of the suspension points on the GAS filters, which affects mode frequencies in their rotational DoFs. Owing to the change in mass distribution by load adjustment, the position of the center of mass is different for every GAS stage. In addition, the height of the GAS keystone is not constant; it drifts by a large amount with temperature changes. Hence the distance of the suspension points from their center of mass changes over time, which behavior is difficult to be modeled. However, the discrepancies can be acceptable as these not-well-modeled features coming from the tilt of the intermediate GAS stages have less impact on the residual motions of the mirror.

Vertical DoFs in GAS filter chain

With the exception of the bottom filter, in the chain of the GAS filter stages, vertical motions are the only DoFs that are measurable and controllable. As LVDT sensors and co-axial coil-magnet actuators are implemented on the keystones with respect to their filter's body, we can only measure the relative transfer functions between the suspended stages. As all the mode frequencies for the GAS vertical modes are expected to be above 0.1 Hz, the frequency responses above 0.03 Hz were measured with the Gaussian injection.

The measured diagonal transfer functions of the GAS vertical are shown in fig. 5.4. There are large deviations in the frequency responses between the measured results and model predictions. As the GAS filter chain can be regarded as a 5-stage-coupled mass-spring system, one expects to observe five mechanical resonances in its response. In fact, the model predicted five peaks in the frequency responses, the appearance of which (namely, height distribution of the peaks) in each stage depends on the shape of the mode. However, the measurement results
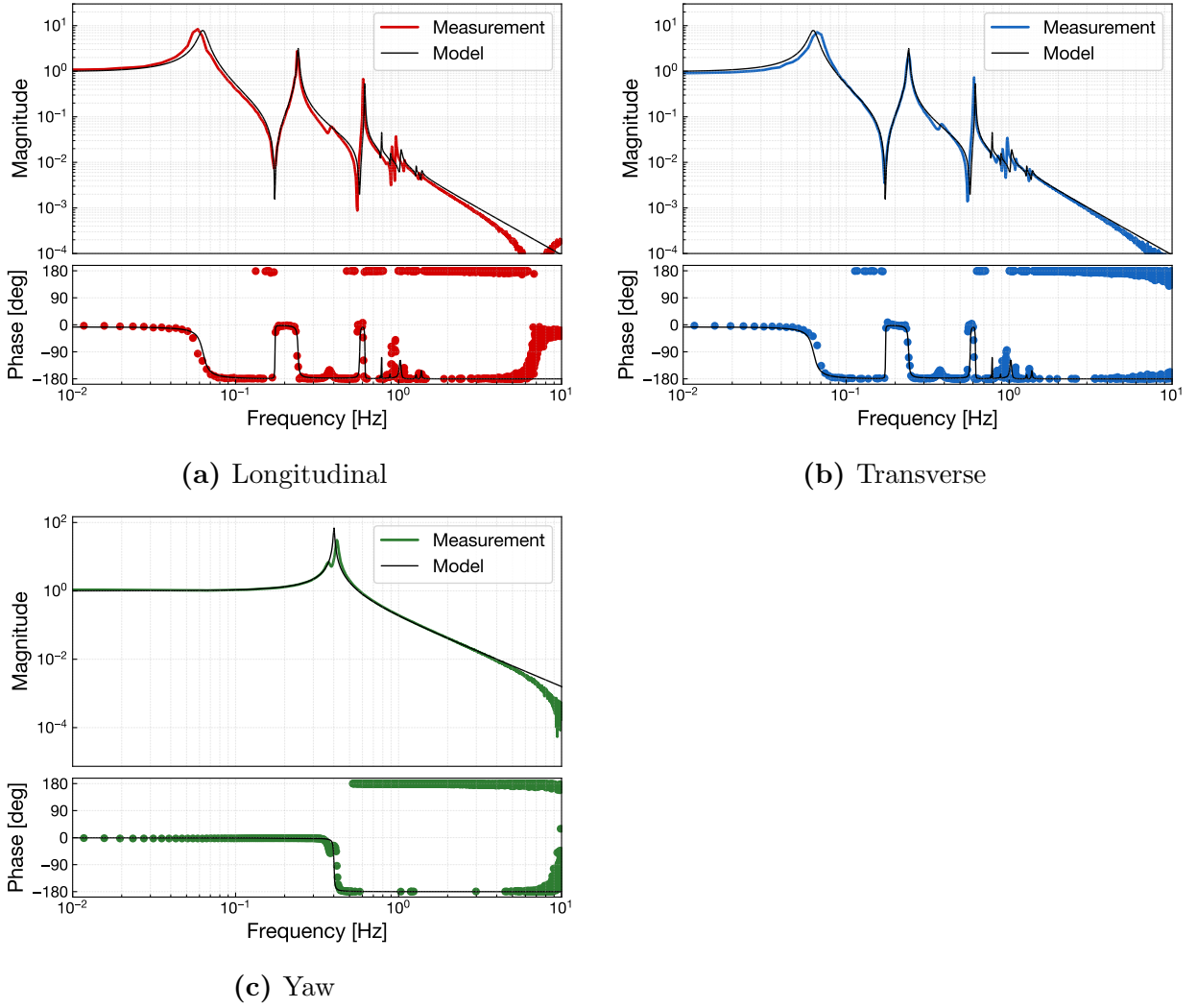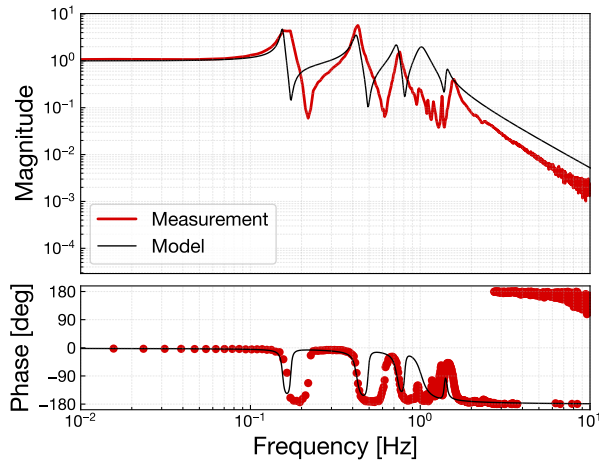
(a) Longitudinal

(b) Transverse

(c) Yaw

Fig. 5.3. Diagonal transfer functions about the IP stage. The measured data are plotted as colored curves and are compared with results of the rigid-body model, which are plotted as black curves.

show remarkable mismatches in their peak appearance for the higher order modes, although the modal frequencies for the lowest 1st, 2nd, and 3rd modes agree between the measurements and model predictions. These discrepancies seem to be caused by the uncertainty of the model and using incorrect sets of parameters such as mass, damping factor, and stiffness distribution. The uncorrelated deviation of the parameters in each individual stage affects the characteristics of higher order modes having finer mode shapes. The result indicates that the installed Type-A tower has many small deviations in physical parameters in the vertical direction.

In addition, small peaks not originating from the pure GAS vertical modes are visible in the measured frequency responses above ~ 0.8 Hz. These structures can be explained as

contributions of coupling from the tilt of the GAS filters. Given the horizontality of the GAS stages assembled by human hands, the tilt modes in pitch and roll rotation can cross-couple to the vertical translation. The resonant frequencies of such rotational modes are expected to be in the range of 0.8–2 Hz, depending on the static position of the keystone. Therefore, the unmodeled peaks being observed around 1 Hz in the measurement results are conceivable.

To summarize the discussions above, although the behaviors of the lower order modes are realized as expected, the constructed Type-A tower has some level of discrepancy from the design or the expected model. As the low-frequency behavior has an impact on the vibration isolation performance, it seems the total operationability of the vertical seismic attenuation is still valid. To investigate the performance further, the residual motion of the suspended dummy payload is discussed in the next section. Moreover, to construct a model of the existing system, another approach known as system identification may be employed to build a model based on the measured response. This method of measurement-based modeling may be applied to the Type-A suspension in the future.
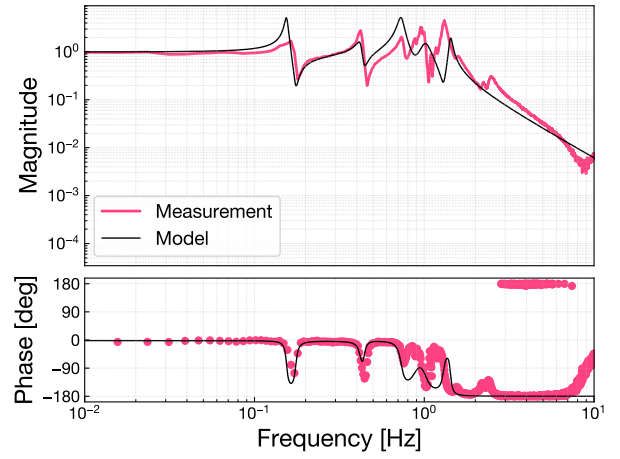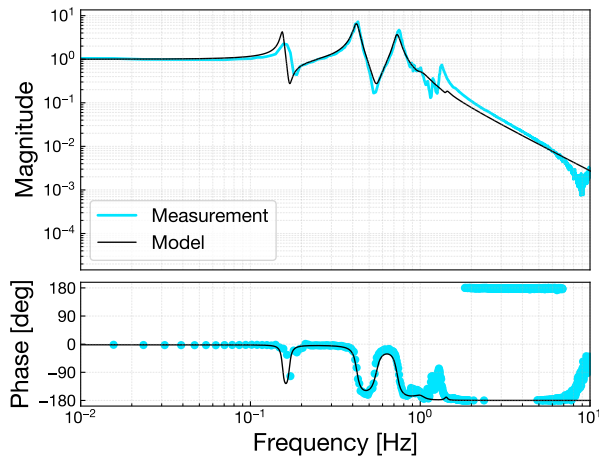
(a) F0 GAS
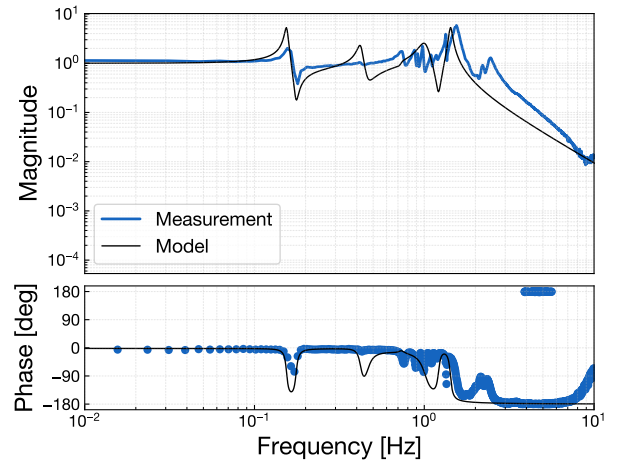
(b) F1 GAS
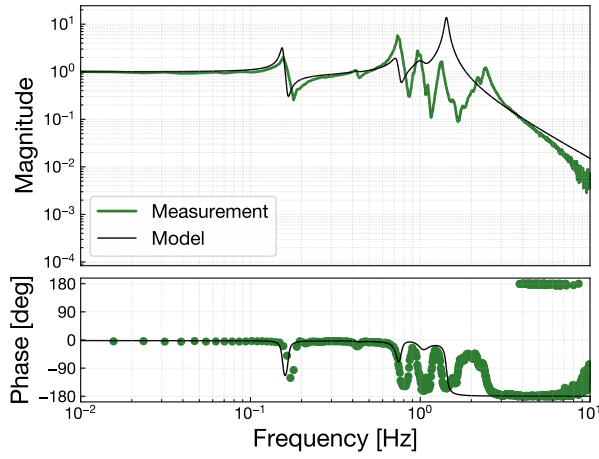
(c) F2 GAS

(d) F3 GAS

(e) BF GAS

Fig. 5.4. Diagonal transfer functions of the GAS stages. The measured data are plotted as colored curves and compared with results of the rigid-body model, which are plotted as black curves.

Six DoFs at bottom filter

The bottom filter has a total of six LVDT-actuator units that enable us to measure transfer functions in all the six DoFs around the BF. As these actuators on the BF were weak and broadband Gaussian injection could not excite the mechanical oscillation sufficiently, we performed the measurements with swept-sine excitation sampling 25 points per decade. Thus, the resulting transfer functions have relatively worse frequency resolutions.

The measured transfer functions about six DoFs of the bottom filter is shown in fig. 5.5. Similarly to the results of IP and GAS, the model predictions are also plotted as black curves. The explanations and discussions for each panel are listed below.

- The frequency responses in the longitudinal and transverse directions show good consistency up to the resonant peak of the 2nd mode at 0.241 Hz. However, the model predicts that the 3rd mode at 0.636 Hz is less visible in the measured longitudinal response and almost invisible in the measured transverse response. It might not have been accurately measured due to the worse frequency resolution or deterioration of coherence at the resonant peaks over averages of the measurements. As the peak structure up to the 2nd mode is observed and sufficiently explained withthe model, it is unlikely of malfunctioning owing to making mechanical contact on the surrounding instrument. In the frequency range of 0.8–1.4 Hz, there are several small peaks that seem to come from the tilt of the GAS filters coupled to the translational DoFs. These couplings are difficult to model and are below the problematic level in the results.

- The result in the vertical direction has, as discussed in the results of the GAS transfer functions, large deviation from the model, especially in the behavior of higher order modes. The possible explanations are similar to the ones described in the GAS results.

- In roll and pitch, the bottom filter shows expected frequency responses consistent with the model prediction. Some small structures other than the main peak of 0.907 Hz can be seen.

- The frequency response in yaw shows good consistency for both the measurements and model predictions in the broadband region. Although the quality factors of the three resonant modes are not sufficiently predicted, they are within the expected values because the quality factors in a real-world system are determined by practical situations and therefore difficult to model. The appearance of the 2nd mode at 60 mHz does not match the predictions of model. It seems to have been caused by the incorrect stiffness distribution of the model. As the 2nd mode has a mode shape that is less observable and controllable at the BF, a small deviation from the nominal parameters could result in comparatively large changes in the behavior of that mode.

- At high frequencies above ~ 2 Hz, all the transfer functions show f^2 dependency. This is known as a sprious coupling in the BF LVDT, where the excitation signals sent to the actuator are directly transmitted to the sensor coil owing to implementation of the shared coil.

According to the discussion above, we can summarize that the bottom part of the installed Type-A tower shows roughly expected performance as it being designed. In this test, the diagonalization of the sensor and actuator were not completed yet owing to the limitation of the experiment period. As the yaw rotation of the BF is extremely soft, the coupling between the yaw rotation and other DoFs may become an obstruction of the control design. The diagonalization of the sensor and actuator, which reduces the cross couplings in the DoFs, is necessary in the further steps.
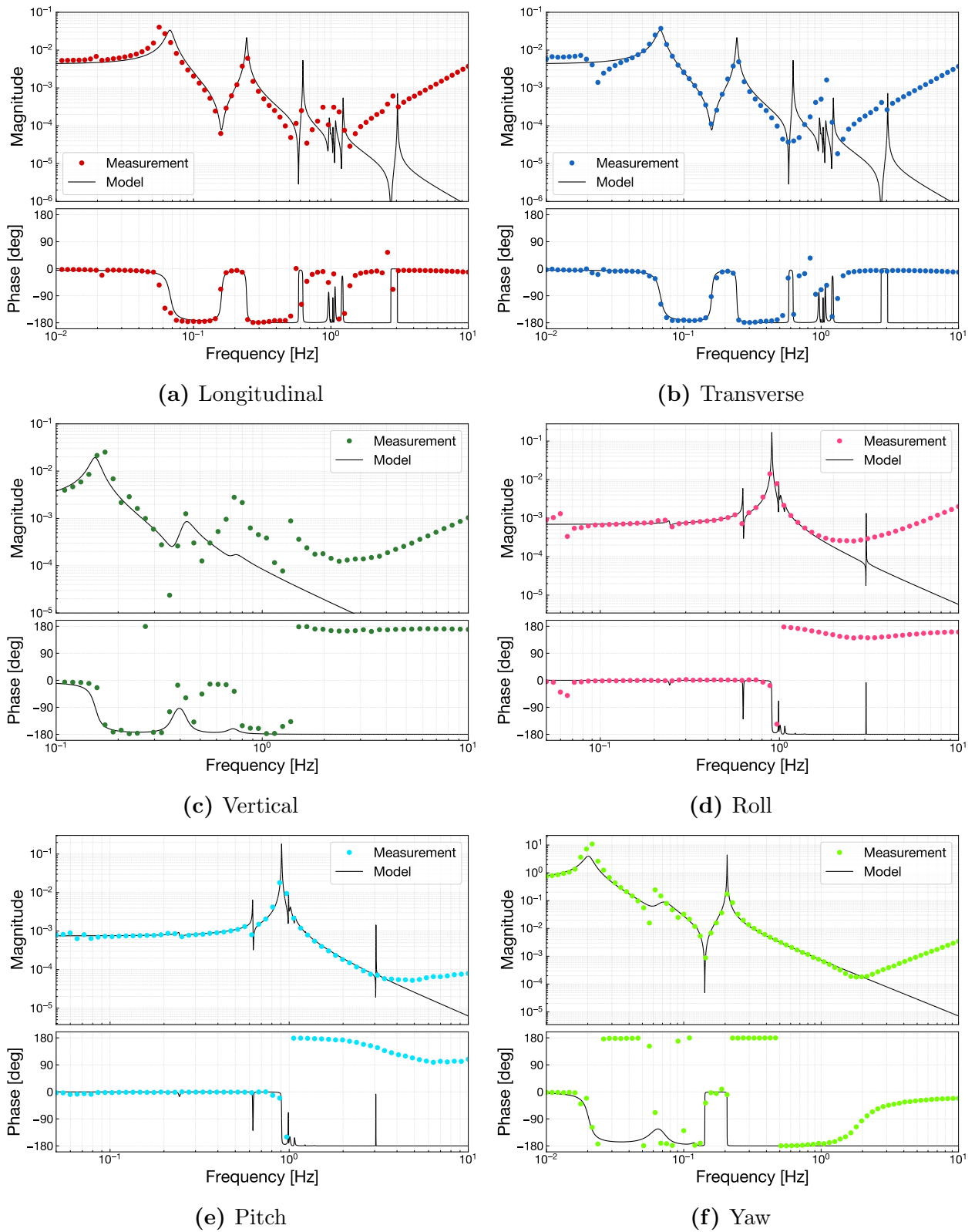
(a) Longitudinal

(b) Transverse

(c) Vertical

(d) Roll

(e) Pitch

(f) Yaw

Fig. 5.5. Diagonal transfer functions about the bottom filter. The measured data are plotted as colored curves comparing with results of the rigid-body model plotted as black curves.

5.2.2   Residual vibration in a stationary state

We measured residual motions of the stages in the installed Type-A suspension in a steady state. The amplitude spectral density of the residual motions in Cartesian DoFs are plotted in fig. 5.6, fig. 5.7, and fig. 5.8. Most of the peaks in the spectra correspond to the mechanical resonances of the suspension, while the inclined floors are indicative of the presence of background noises.
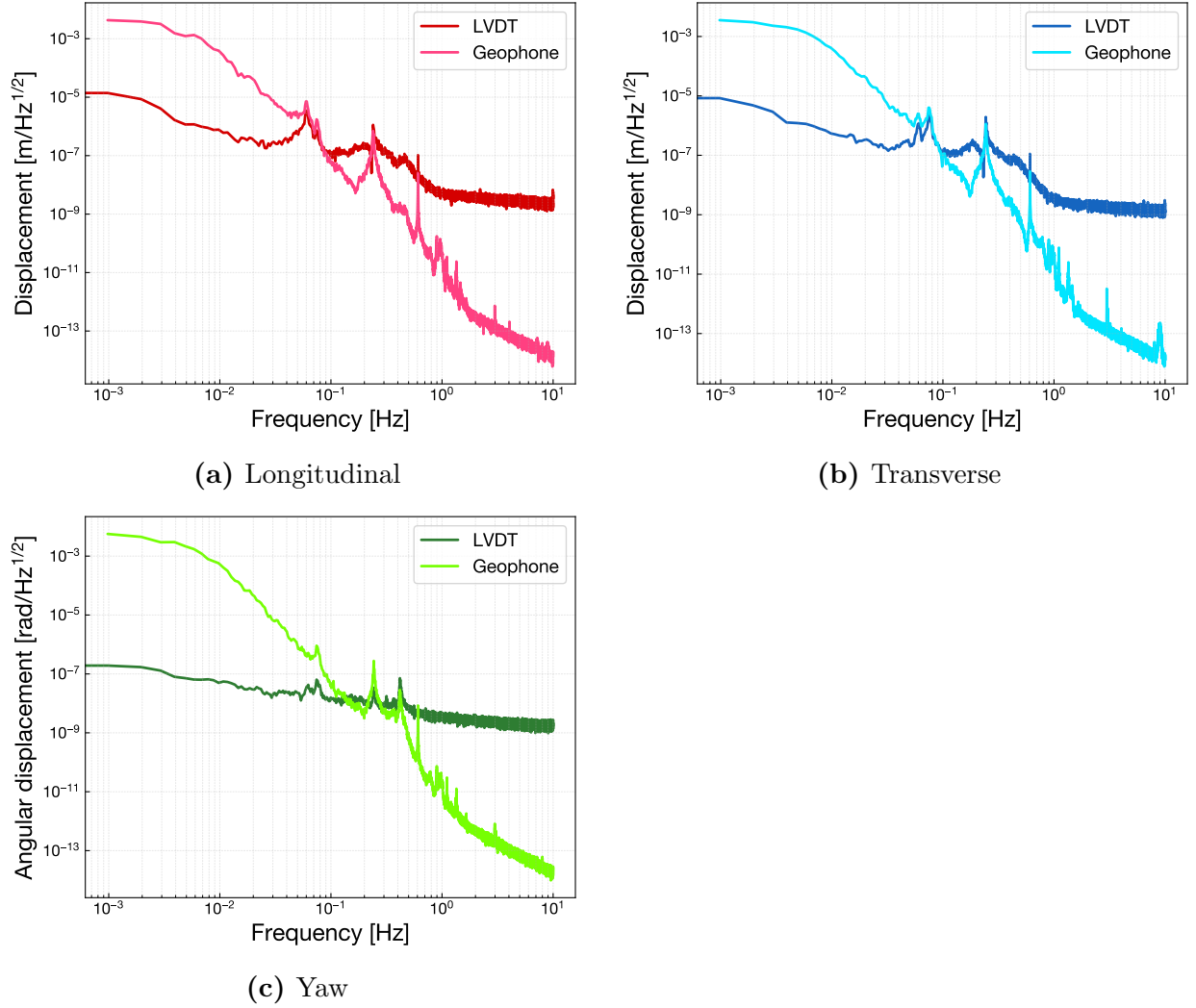

(a) Longitudinal

(b) Transverse

(c) Yaw

Fig. 5.6. Amplitude spectral density of the IP in a stationary state without any control.

IP pre-isolation stage

The residual motion of the IP stage is monitored with two kinds of sensors: LVDT and geophone sensors. The measured spectra in fig. 5.6 show that clear differences exist in the characteristics of these sensors. As the LVDT monitors displacement of the IP stage

with respect to the ground, its amplitude is dominated by a microseism in the range of 0.1–0.9 Hz, except for some excesses in the mechanical resonances, in the spectra of the translational DoFs. By contrast, the geophone is less sensitive to the motion of the ground because it measures velocity with respect to the inertial frame. Therefore, at the microseismic frequencies the geophone spectra have a floor level that is smaller than that of the LVDT by 1–2 orders of magnitude. To damp some high-Q eigenmodes independently of the microseismic disturbance, one should use the geophone signals, instead of the LVDT signals, for feedback control.

On the other hand, the LVDT exhibits superiority in position stabilization at lower frequencies below ~ 0.1 Hz. In terms of displacement, the inherent noise of the geophone is amplified as the frequency decreases owing to its frequency response. As the LVDT reads out displacement signals with a less frequency-dependent noise floor, it is more appropriate to use the LVDT to maintain the static position of the IP stage with respect to the reference frame.

GAS filter chain

The measurement results of the vertical residual motion in the GAS stage are shown in fig. 5.7. The first mode (0.18 Hz) and the second mode (0.46 Hz) appear as significant peaks; moreover the third mode peak is slightly visible at 0.77 Hz. However, the higher order modes, namely the 4th and 5th modes, cannot be observed in a stationary state. This indicates that the system of the Type-A GAS chain stores oscillatory energy in the higher order modes that is not large enough to be observed with the LVDT sensors. Note that the sensor noise in each GAS stage has a different floor level as the LVDT noise has a DC position dependency of the keystone.

Bottom filter

As the local sensors at the BF monitor the relative displacement of the BF body with respect to the ground, the residual motions of both the suspended stage and the ground itself can be observed. In fig. 5.8a, whereas the many resonant peaks are standing with high quality factors, a broad bump of the microseismic motion appears in the range of about 0.1–0.8 Hz for all the translational DoFs. If local control including this band is engaged, it will introduce seismic noise into the suspended BF and can be problematic.

One potential problem at the BF is the large cross couplings between the DoFs. In this test, the diagonalization of the sensing matrix and driving matrix had not been applied yet due to the limitations of the experiment period. As one of the important role of the BF LVDT is to damp the torsion mode of the single-wire suspension chain, a cross coupling from the translations in the microseismic band can cause unexpected excitations into the
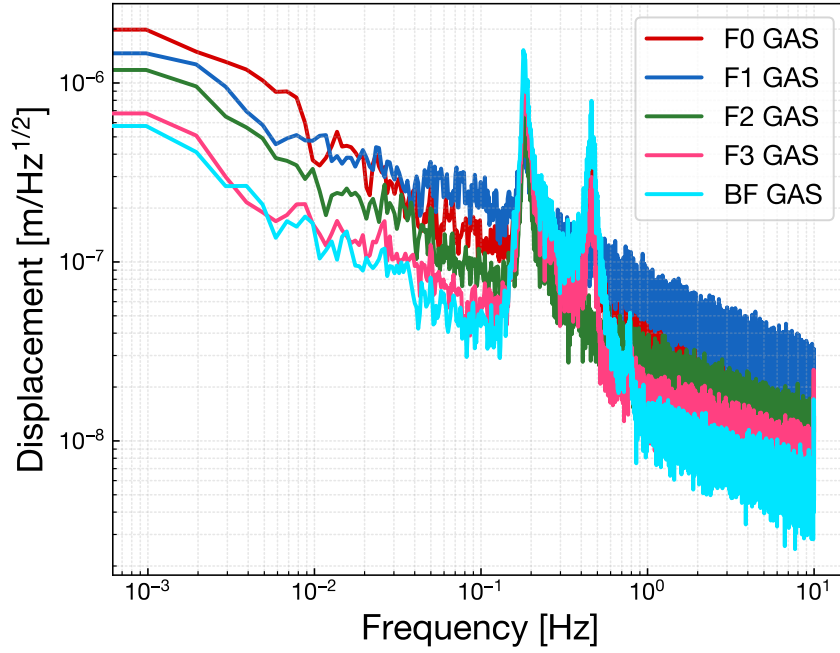
Fig. 5.7. Amplitude spectral density of the GAS LVDT in a stationary state without any control.

yaw control. Actually, some peaks of the yaw modes, located at 21 mHz and 63 mHz, are coupled to the translation DoFs and observed in their spectrum. Similarly, the spectrum in the rotational direction also shows some influence of coupling from the translations leading some peaks such as the ones at 73 mHz and 0.18 Hz. To confirm the small enough magnitude of DoF-couplings, further handling of sensing and driving matrix will be necessary.

Residual motion at dummy payload

During the performance test of the Type-A tower, we have additional sensors at the dummy payload. Two geophones, the same type as those mounted on the IP stage, are implemented on the DP for the horizontal and vertical motion sensing. The geophone is chosen as it can measure the residual motion of the attached object with respect to the inertial frame, independently of fluctuation of the reference frame such as the ground. However, owing to the limited capacity of the dummy payload, we have implemented the two translational DoFs, one horizontal and another one vertical, geophones, and no angular sensing is available.

The measured residual vertical motion of the DP is shown in fig. 5.9. For comparison, the spectrum calculated with the model and the measured seismic noise is also plotted. Note that, as this measurement was held in a stormy day, the magnitude of the seismic noise in this measurement is roughly as large as the Kamioka High Noise Model (KHNM), which is mentioned in section 3.1.1. Although the measured transfer functions of the GAS stages
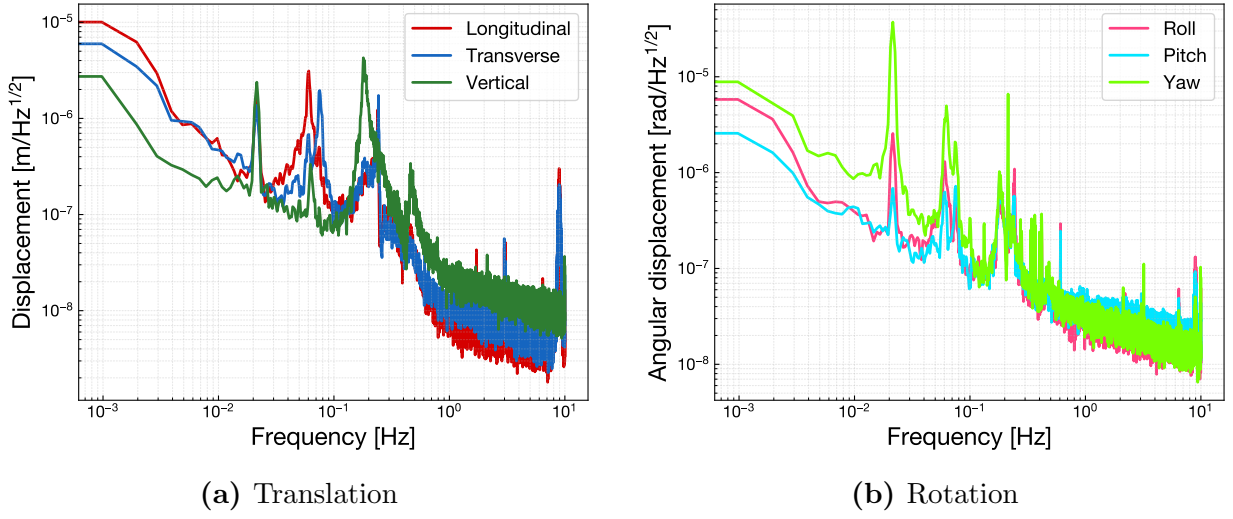
(a) Translation

(b) Rotation

Fig. 5.8. Amplitude spectral density of the BF in a stationary state without any control.

are not sufficiently consistent with the responses predicted in the model, as discussed in section 5.2.1, the spectra of the measurement and the model show good coincidence below 1 Hz except for the quality factors at the resonant peaks. This result is evidence that one can guarantee the total operationability of the vertical seismic attenuation for the constructed Type-A system and compensate for the small consistency in the results of the transfer function measurements. However, unmodeled structure above 1 Hz that looks like a series of small resonant peaks can be observed. This is a common feature also observable in the measured frequency responses and seems to originate from the tilt couplings of the GAS stages. As the geophone is not sensitive enough to detect the residual motions above 2 Hz, we cannot conclude that the impact of these cross couplings is acceptable even in the observational band starting from 10 Hz. That should be tested after integration into the full configuration of the Type-A suspension.

In a natural state under even the noisy seismic disturbance, the RMS residual motion of the DP is measured as 4.0 μm. Considering the requirement of the vertical RMS displacement is less than 100 μm, we can conclude that the resonant modes in the vertical direction will not amplify the residual motion of the payload more than the required level.

The measured residual motion of the DP in the horizontal direction is shown in fig. 5.10. Note that, due to the geometrical symmetry, the horizontal motions of the DP can be replaced by both the longitudinal and transverse motions. The spectrum of the measured residual motion of the DP has an unnaturally small magnitude compared to the model prediction due to malfunction. Therefore, evaluation with the DP geophone can misread the resulting residual motion.

An alternative measure of the residual motion is one measured with the BF LVDT. As the BF LVDT read the relative displacement between the BF and the ground, the measured
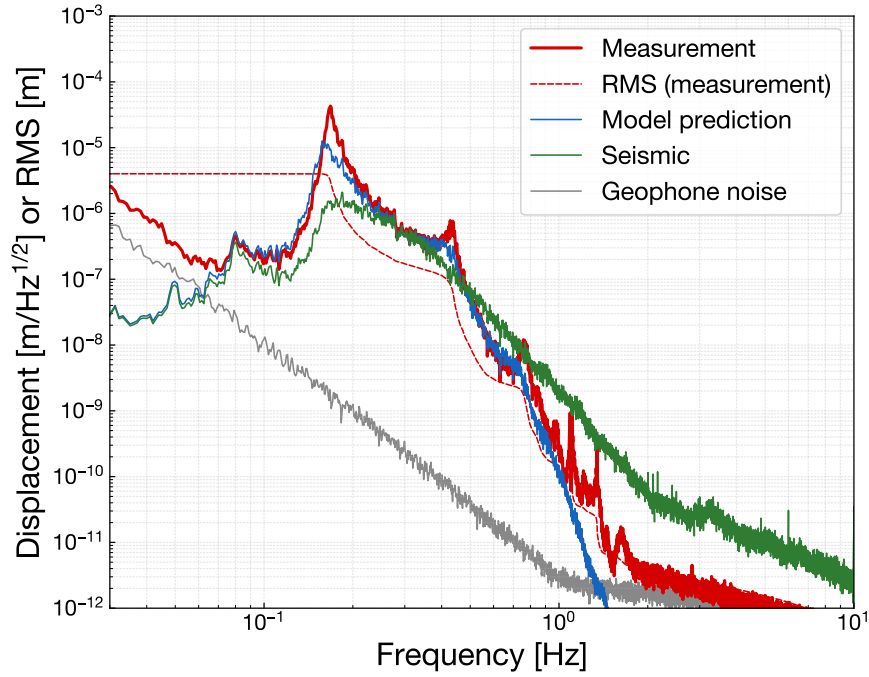
Fig. 5.9. Amplitude spectral density of the vertical motion of the DP in a stationary state measured by a geophone (*red*). The curve labeled as "model prediction" (*blue*) is calculated from the measured seismic spectrum (*green*) multiplied by the transfer function model from the ground to the DP.

spectrum is a sum of BF's motion and the seismic noise. Thus, the measured spectrum at the BF can offer the upper limit of the residual motion at the bottom stage of the Type-A tower. The result of the measurement at the BF is shown in fig. 5.11. Assuming that all the amplitude of displacement comes from the BF's residual motion, The RMS amplitudes are 1.1 μm in the longitudinal direction and 1.4 μm in the transverse direction. These values are sufficiently smaller than the requirement of the RMS residual motion in the longitudinal and transverse direction in the calm-down phase.

Another requirement in the horizontal direction is the longitudinal RMS velocity required for the smooth lock acquisition. Although the Type-A tower setup does not have the actual payload, it can give a reference value of an achievable RMS velocity for the whole center-of-mass motion of the suspended payload. However, as discussed above, the horizontal geophone attached on the DP is no longer useful for evaluating the residual motion of the DP. Thus, instead, the RMS residual velocity was evaluated with the spectrum measured at the BF, which is plotted in fig. 5.12. The RMS velocity is obtained as a cumulative integration from 3 Hz down to 0.03 Hz in order to take only the mechanical motion into account and not to include the sensor noise contribution at high frequency. Even assuming that the pure BF contributes to the resulting RMS velocity, the measured RMS velocity is 0.73 μm/s, which is much less than the requirement of 240 μm/s. Thus, although the horizontal geophone at the

DP could not give a meaningful result, it is indicated that the sufficiently small RMS velocity is achieved with the constructed Type-A tower instrument.
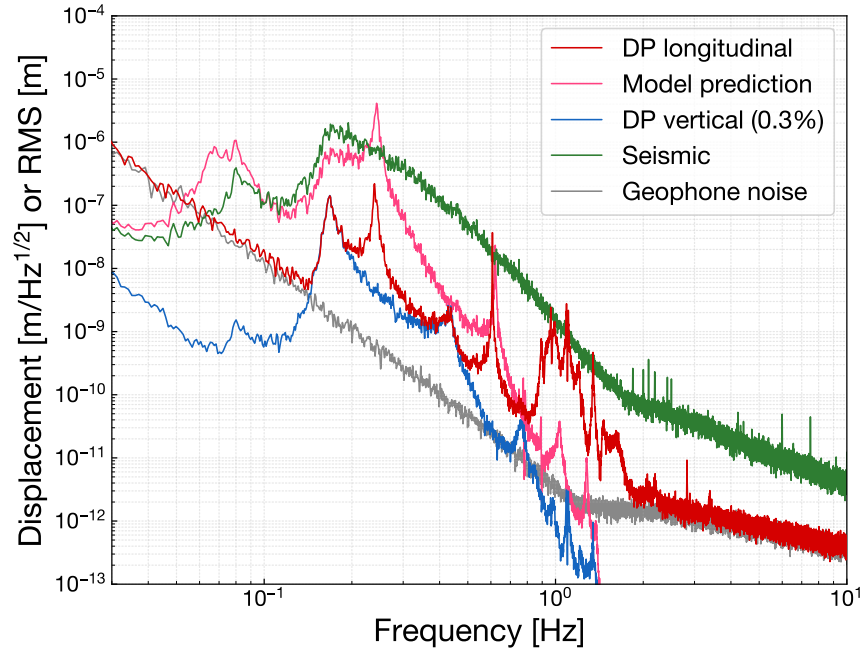
Fig. 5.10. Amplitude spectral density of the horizontal motion of the DP in a stationary state measured by a geophone (*red*). The curve labeled as "model prediction" (*pink*) is calculated from the measured seismic spectrum (*green*) multiplied by the transfer function model from the ground to the DP. To confirm the plausibility of the spectrum at the DP, the coupling from the DP's vertical motion (*blue*) is also plotted for comparison.
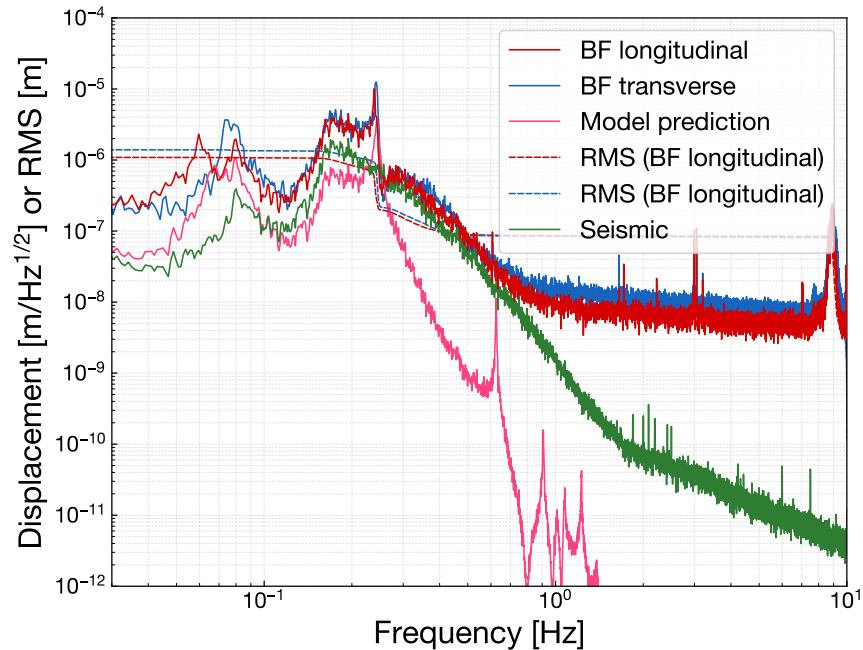

Fig. 5.11. Amplitude spectral density of the horizontal motion of the BF in a stationary state measured by BF LVDTs (*red* and *blue*). The curve labeled as "model prediction" (*pink*) is calculated from the measured seismic spectrum (*green*) multiplied by the transfer function model from the ground to the BF.
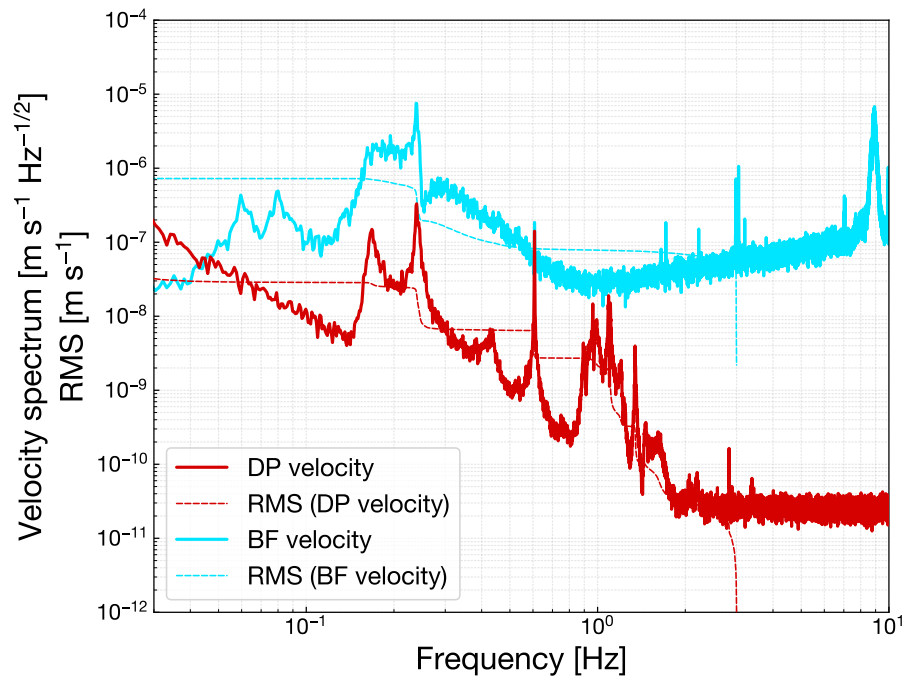
Fig. 5.12. Velocity spectral density of the longitudinal motion of the DP and BF in a stationary state. The RMS is integrated from 3 Hz down to the low frequencies in order to exclude the sensor noise contribution.

5.3   Torsion mode damping

The torsion mode of the Type-A suspension is one of the considerable DoF oscillation. As mentioned in the previous chapters, the Type-A suspension has long single-wire chain that can also behave as a torsion pendulum with a high quality factor. Nevertheless, the torsional motion of the suspended mirror leads misalignment of the interferometer that results in a large amount of beam spot fluctuation at the 3-kilometer distance. Therefore, we need to implement an appropriate damping function onto the oscillation in the yaw direction of the Type-A chain.

The setup of the Type-A tower, in the absence of a cryogenic payload, is still suitable for testing the torsion mode damping as the dynamics of the yaw motion are almost subject to the mechanical properties of the tower part, which accounts for a major fraction of the total wire length. In the two angular DoFs for the mirror alignment, namely pitch and yaw, the single-wire components with low torsional stiffness distributed over the entire chain contribute to the yaw motion, while the pitch motion is dominated by the multi-wire suspension design inside the cryogenic payload. A single-wire connection has small torsional stiffness, whereas it has less coupling in the tilt of the masses when the suspension points are close enough to their center of mass. On the other hand, a multi-wire connection with some horizontal offsets from their center of mass has a larger stiffness during pitching and yawing, causing a strong mechanical coupling between the connected masses. Thus, although pitching of the test mass is strongly coupled to the marionette, which is less affected by the tower stages, yawing will be substantially correlated to the torsion of the tower stages.

The only stage in the Type-A tower where we can apply the yaw control is the bottom filter. As described in section 3.4.1, the bottom filter is equipped with the sensor-actuator-integrated device BF LVDT for all six DoFs of the BF body with respect to the ground. Although the cryogenic payload in the full configuration has additional angular sensors such as optical levers and photo-reflective sensors, besides the sensors and actuators at the BF, no other sensors and actuators are available in the tower stages. The LVDT at the IP also does not play a role during the yawing of the suspended stages with single-wires. Thus, torsion mode damping here is related to the single-input-single-output (SISO) control problem at the BF.

In this study, torsion mode damping of the Type-A tower is performed in order to satisfy two types of requirements: $1/e$ decay time for the mechanical resonances and RMS residual motion in the frequency region above 10 mHz. The $1/e$ decay time is a requirement in the calm-down phase for quick recovery of operation of the interferometer when a large disturbance excites the instruments. The RMS residual motion is one in the lock-acquisition phase so that the control can be switched to another that uses more sensitive but smaller-ranged sensors and actuators.
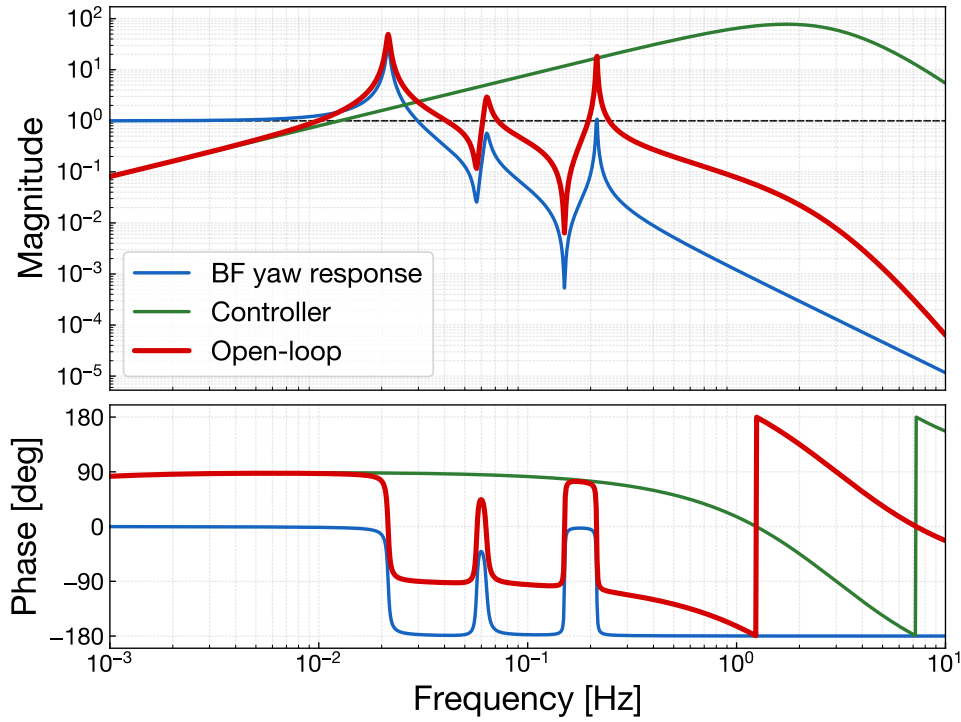
Fig. 5.13. The open-loop transfer function of the BF yaw damping control.

5.3.1 Controller design

The aim of damping control is to suppress the mechanical resonances in the yaw direction. As the lower resonant modes will often dominate the magnitude of RMS fluctuation, we focused on the three resonant modes from the lowest. This strategy is also natural as the lowest three resonances are visible in the measured frequency response of the yaw DoF at the BF.

The open-loop transfer function of the BF yaw damping control is shown in fig. 5.13. The frequency response of the BF yaw is constructed as a SISO model based on the measured transfer function in fig. 5.5f and then normalized at the DC. The modeled BF yaw response has three mechanical resonances with the mode frequencies of 21.5 mHz, 63.5 mHz, and 214 mHz that are identified in the spectrum in a stationary state. In fig. 5.13, the peak of the 2nd mode looks relatively small owing to its mode shape, indicating this mode has poor controllability and observability for the input/output point of the BF.

The controller of the damping servo has a 1st-order high-pass feature at and below 1 Hz and a 3rd-order low-pass feature above 3 Hz. The controller is designed so that the resulting open-loop transfer function has a gain of more than unity at and around the mechanical resonant peaks. The 1st-order high-pass characteristics at the peak frequencies guarantee the stability of the feedback loop, while the low-pass characteristics at the high frequencies reduce sensor noise reinjection through the sprious coupling in the BF LVDT. The bandwidth

of damping control extends up to the 3rd resonant mode, which is interpreted as a unity-gain frequency of 0.24 Hz. The stability of this control loop is parameterized as the minimum phase margin of 74.5° and the gain margin of more than 10.

5.3.2 Decay time measurement

To evaluate the damping performance required in the calm-down phase, the exponential decay time was measured for each resonant mode during yaw motion. The procedure is as follows; first the target mechanical resonance was excited by sending the monochromatic sinusoidal-wave injection using the virtual yaw actuator. After the resonance was sufficiently excited and the amplitude reached a steady state under excitation, we stopped the injection and monitored the time series of the decaying amplitude. The measured decay signal was fitted by a sine wave function with an exponential decay, which can be written as

$$f(t) = A\mathrm{e}^{-t/\tau_{\mathrm{e}}}\,\sin(2\pi f_0 t + \phi_0) + x_0\,, \tag{5.1}$$

where τ_{e} denotes the 1/e decay time when the amplitude decreases by 1/e from a given time, f_0 is the mode frequency, A is the initial amplitude, ϕ_0 is the initial phase, and x_0 is the DC offset. Sometimes it is difficult to excite a single higher-order mode alone owing to the softness of the fundamental mode, and resulting waveform becomes a superposition of some sinusoidal waves with different frequencies. In such a case, we assumed that the decay signal was a sum of two different decaying sine waves and fitted by a double-mode waveform written as

$$f(t) = A_1\mathrm{e}^{-t/\tau_{\mathrm{e}1}}\,\sin(2\pi f_1 t + \phi_1) + A_2\mathrm{e}^{-t/\tau_{\mathrm{e}2}}\,\sin(2\pi f_2 t + \phi_2) + x_0\,. \tag{5.2}$$

The measured decay signals of the yaw resonant modes are shown in fig. 5.14. As expected by intuition, in a natural state without damping control, the yaw modes have very long decay times of more than 100 s. Although, in the 1st mode and 3rd mode, the measured signals are clearly observed and sufficiently fitted to the theoretical expression, the undamped 2nd mode in fig. 5.14c seems less visible and buried in the 1st-mode signal owing to its poor observability at the BF. These yaw modes with their intrinsic damping will continue for a long time when they are kicked once and can be an issue disturbing the interferometer operation.

As we can see in the right panels of fig. 5.14, with the damping control engaged, every yaw mode looks significantly damped in a sufficiently short period of time. The fitting results of the decay time with/without damping control are summarized in table 5.2. It indicates that damping control at the BF can reduce the exponential decay time of the mechanical resonances in yaw motion and satisfy the requirement of less than 1 min. Although some mismatches between the measurement and fitting can be seen in the damped oscillation in fig. 5.14, the inaccuracy of the fitting does not seem to have an impact on the result of the decay time requirements.

Table 5.2. Fitted decay time of the yaw modes.

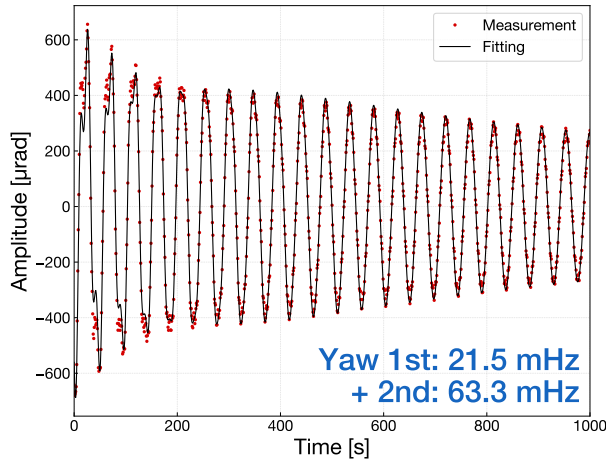| Mode	Undamped			Damped		
	f_0 [mHz]	τ_e [s]	Q-factor	f_0 [mHz]	τ_e [s]	Q-factor
#1	21.3	961.4 ± 4.6	64.9	19.3	24.8 ± 0.8	1.5
#2	63.5	158.6 ± 4.6	31.6	62.9	43.9 ± 0.5	8.7
#3	213.3	1155.5 ± 1.9	774.3	215.2	9.5 ± 0.1	6.4

5.3.3   Reduction of RMS residual motion

The amplitude spectral density of the BF yaw with and without damping control is measured. The result of the spectral measurement is shown in fig. 5.15. Although the RMS residual motion in a natural state is dominated by the yaw-mode peaks, these resonant peaks are successfully suppressed by damping control. When damping is turned on, the RMS is dominated by the remaining structure around 60–70 mHz, which seems to be the residual of the 2nd yaw peak and couplings from the 1st mode of the IP in the longitudinal and transverse directions. Suppose that only the sensor noise contributes to the spectrum below 0.01 Hz, the RMS residual motion in yaw is evaluated as 1530 nrad for the undamped state and 227 nrad for the damped state. This RMS level under the local damping control satisfies the requirement of less than 880 nrad for the lock-acquisition phase, indicating that it is sufficiently small to hand over angular control to the interferometer loop using the wave front sensor. Note that the higher accumulated RMS of the damped state above 0.2 Hz can be affected by the DC position dependency of the sensor noise floor.
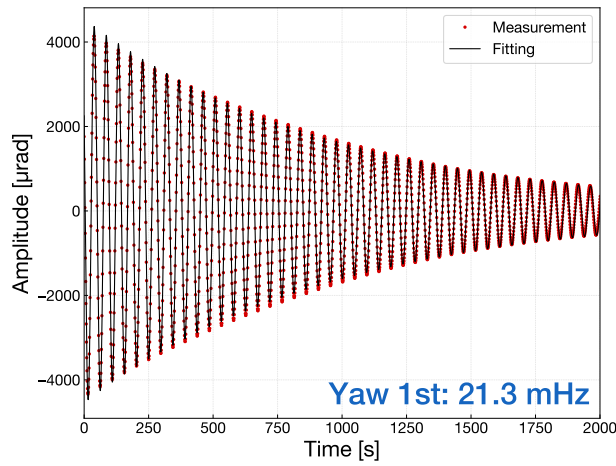
(a) 1st mode (undamped)
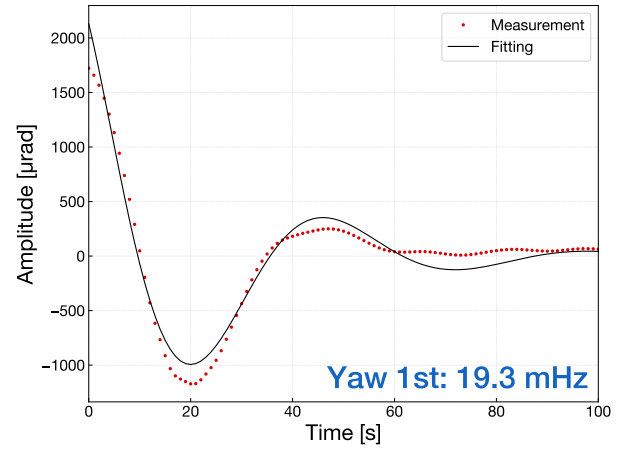
(b) 1st mode (damped)

(c) 2nd mode (undamped)
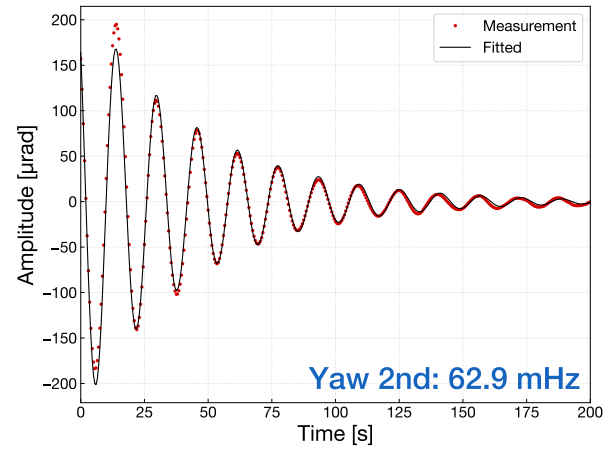
(d) 2nd mode (damped)
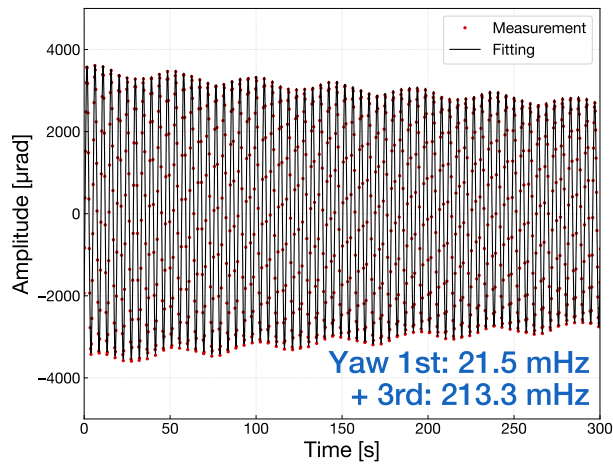
(e) 3rd mode (undamped)
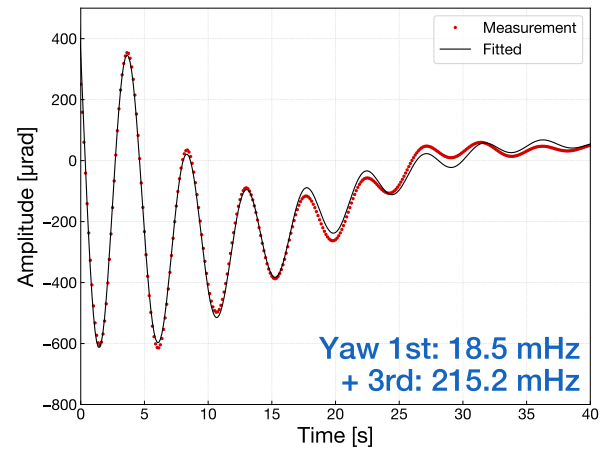
(f) 3rd mode (damped)

Fig. 5.14. Decay signals of the yaw modes at the BF. The *left* figures, **(a)**, **(c)**, and **(e)**, are the decay signals without control, while the *right* figures, **(b)**, **(d)**, and **(f)**, are ones with the damping loop closed. The fitted frequencies of the sine wave are also annotated in each figure.

Fig. 5.15. Comparison of the amplitude spectral density of the BF yaw with/without the damping control.

5.4   Modal damping for GAS vertical modes

We tested the modal damping mechanism in the vertical control of the Type-A tower. The vertical modes in the full configuration of the Type-A suspension can be divided into two groups, the GAS modes and the payload's internal mode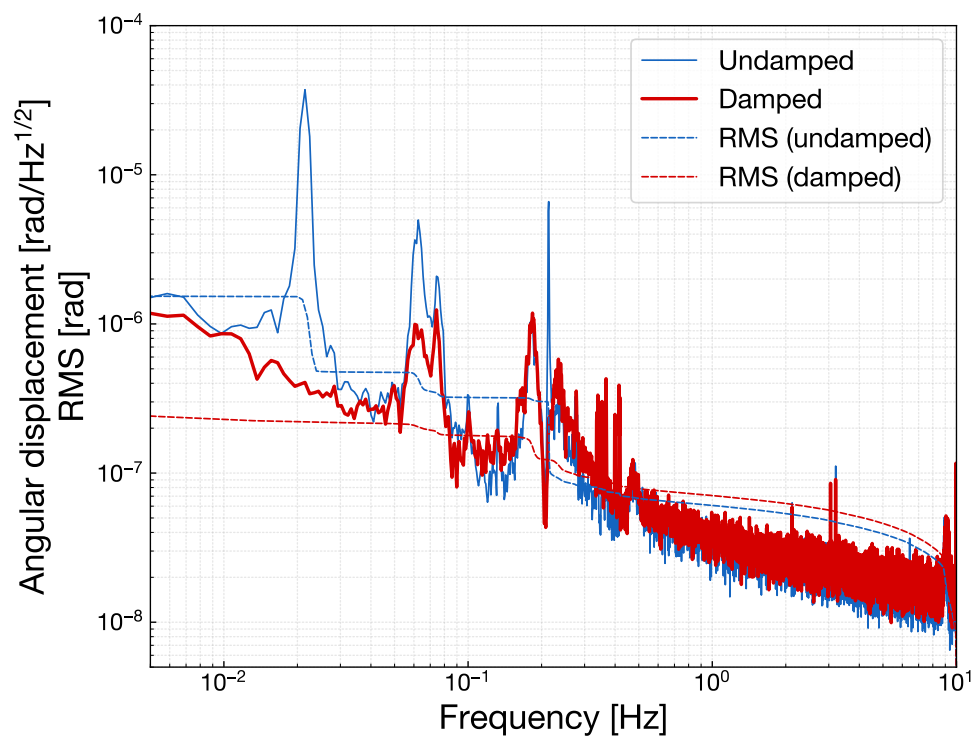s. The GAS modes have mode frequencies in the range of 0.1–1.5 Hz owing to the support with soft springs, while the payload's vertical modes are distributed above 4 Hz owing to the stiff-spring suspensions. As we only consider the lower order modes that often have a large impact on the RMS residual motion, the Type-A tower containing all the GAS stages is an adequate setup to demonstrate the lower-order vertical mode control.

The eigenmode matrix necessary to obtain the modal signals was generated by the vertical-DoF submodel extracted from the 3D rigid-body model of the Type-A tower, which is also used in the fig. 5.4 for comparison. As discussed in section 5.2, this model exhibits large deviations in the mode shape of the GAS vertical modes from the measured responses. Nevertheless, we used this imperfect model because it would be able to decouple the lowest-order modes at which frequencies the model prediction and the measurement result show reasonable consistency.

5.4.1   Diagonalization of the sensing and driving matrix

Even if we focus on only the lower order modes, one can predict that the nominal eigenmode matrix derived from the model is not accurate enough to be used in real-world systems. Therefore, we performed diagonalization onto the sensing and driving matrix of the modal sensors and actuators. The diagonalization aligns the mode shape included in the sensing and driving matrix with the one in an actual system.

Suppose that, in an ideal case, the modal displacement signals $\boldsymbol{\eta}$ and the GAS LVDT signals $\boldsymbol{V}_{\mathrm{LVDT}}$ are connected by the following relationship:

$$\boldsymbol{\eta}(t) = \boldsymbol{\Phi}^{-1} \boldsymbol{S} \, \boldsymbol{V}_{\mathrm{LVDT}}(t) \,, \tag{5.3}$$

where $\boldsymbol{\Phi}$ is the eigenmode matrix and $\boldsymbol{S}$ is the conversion matrix from the LVDT signals to the Cartesian displacement signals of the stages. Now the multiplied matrix $\boldsymbol{\Phi}^{-1}\boldsymbol{S}$ is called the *sensing matrix*. It converts the raw sensor signals into modal displacements. However, this is not the case in most systems in the real world, which have unwanted cross couplings in the DoFs, such as

$$\boldsymbol{\eta}(t) = \boldsymbol{C}_{\mathrm{s}}\boldsymbol{\Phi}^{-1} \boldsymbol{S} \, \boldsymbol{V}_{\mathrm{LVDT}}(t) \,, \tag{5.4}$$

where $\boldsymbol{C}_{\mathrm{s}}$ denotes the coupling matrix; ideally $\boldsymbol{C}_{\mathrm{s}} = \boldsymbol{I}$. Similarly, we can write the incomplete driving matrix for the modal actuators as

$$\boldsymbol{A}(t) = \boldsymbol{D}\boldsymbol{\Phi}\boldsymbol{C}_{\mathrm{d}}\boldsymbol{V}_{\eta}(t) \tag{5.5}$$

where $\boldsymbol{A}$ is a set of feedback signals sent to the real actuators and $\boldsymbol{D}$ is the conversion matrix from the Cartesian feedback signal to the GAS differential actuations. The coupling matrix $\boldsymbol{C}_{\mathrm{d}}$ affects, in this case, the right of the *driving matrix* $\boldsymbol{D\Phi}$.

Diagonalization is a procedure that allows the coupling matrices, $\boldsymbol{C}_{\mathrm{s}}$ and $\boldsymbol{C}_{\mathrm{d}}$ to become identity matrices $\boldsymbol{I}$. For this purpose, one should obtain the coupling matrices with some measurements and update the existing sensing or driving matrix by multiplying the inverse of the derived coupling matrices so that the non-diagonal elements of the coupling matrices are zero. In the case of the sensing matrix, the procedure is as follows:

1. Send a sinusoidal signal with a modal frequency and excite the suspension using the incomplete modal actuator.

2. As the system can store the total energy as a form of its natural vibration, all the modal signals at the excited modal frequency will be dominated by the contribution from the excited mode even by the incomplete modal actuator.

3. After the suspension reaches steady state under the excitation, measure the amplitude spectrum.

4. Calculate the coupling ratio of the non-diagonal modes to the excited diagonal mode from the transfer function at the frequency you excited.

5. Build a coupling matrix by normalizing every column so that the diagonal elements become unity.

6. Update the existing sensing matrix by multiplying the inverse of the derived coupling matrix from the left.

In the case of the driving matrix, the procedure is as follows:

1. Send a broadband Gaussian injection using the incomplete modal actuator and measure the transfer functions from the modal actuator to all the modal sensors.

2. Select a frequency that is sufficiently below all the modal frequencies and calculate the coupling ratio of the non-diagonal modes to the excited diagonal mode from the transfer functions.

3. Build a coupling matrix with normalizing every row so that the diagonal elements become unity.

4. Update the existing driving matrix by multiplying the inverse of the derived coupling matrix from the right.

By repeating the procedure several times, the coupling matrices become asymptotically close to identity matrices.

Strictly speaking, the diagonalization of the driving matrix should take the frequency dependence into account as the couplings in the actuator include the mechanical response of the system. Therefore, it is desirable replace the driving matrix with a SISO-filter-elemented matrix or a state-space model to implement a multi-input-multi-output (MIMO) operation. Nevertheless, a scalar-elemented driving matrix is chosen in this experiment owing to the difficulty of the implementation of frequency dependence. Thus, the driving matrix was diagonalized at a low frequency of 0.03 Hz, which is sufficiently below the modal frequencies where the phase of the frequency responses for every mode is aligned to zero.

5.4.2 Vibration in modal basis

After repeating the diagonalization procedure a few times, the transfer functions of the GAS vertical mode in the decoupled modal basis were measured, as shown in fig. 5.16. As predicted from the modeling accuracy, the modal transfer functions of the lowest two modes, namely 0.155 Hz and 0.421 Hz, can be approximated by the response of a single-DoF oscillation system, and hence the modal decomposition was successfully operated. Although the 3rd mode of 0.727 Hz seems to be decoupled just like the 1st and 2nd mode, its response has a non-trivial structure, with a parasitic resonance at 1.2 Hz. The response of the following 4th and 5th modes are no longer sufficiently decoupled to single-DoF systems owing to the inaccurate guess of the mode frequency and its shape. The DC gain of the modal responses correspond to the inverse of the modal mass in theory as the norms of the eigenvectors are normalized as unity for every mode. However, in a real system, the ratios of the DC gain are contaminated with the calibration errors of the sensors and the individual differences of the actuator efficiency. The uncertainty of the DC gain of the modal responses does not matter in the design of the damping controller as the overall loop gain can be obtained with the measured frequency response.

The modal spectrum of the GAS vertical modes in a stationary state is shown in fig. 5.17. For the 1st and 2nd modes, which are sufficiently decoupled, their peaks are significant, whereas the higher modes do not show any meaningful structure in their spectrum. This can also be explained as the inaccurate modal decomposition of the higher order modes. From this figure, it can be seen that the 1st mode has the largest amplitude in a stationary state, which is expected. Although the 3rd mode does not seem to be even a little decoupled in the frequency response, a considerable peak at the corresponding frequency in the spectrum is not apparent. It implies that, in a natural state, the higher order modes may store little energy in this vertical system.

The result in this experiment suggests that, even if the model includes a measurable
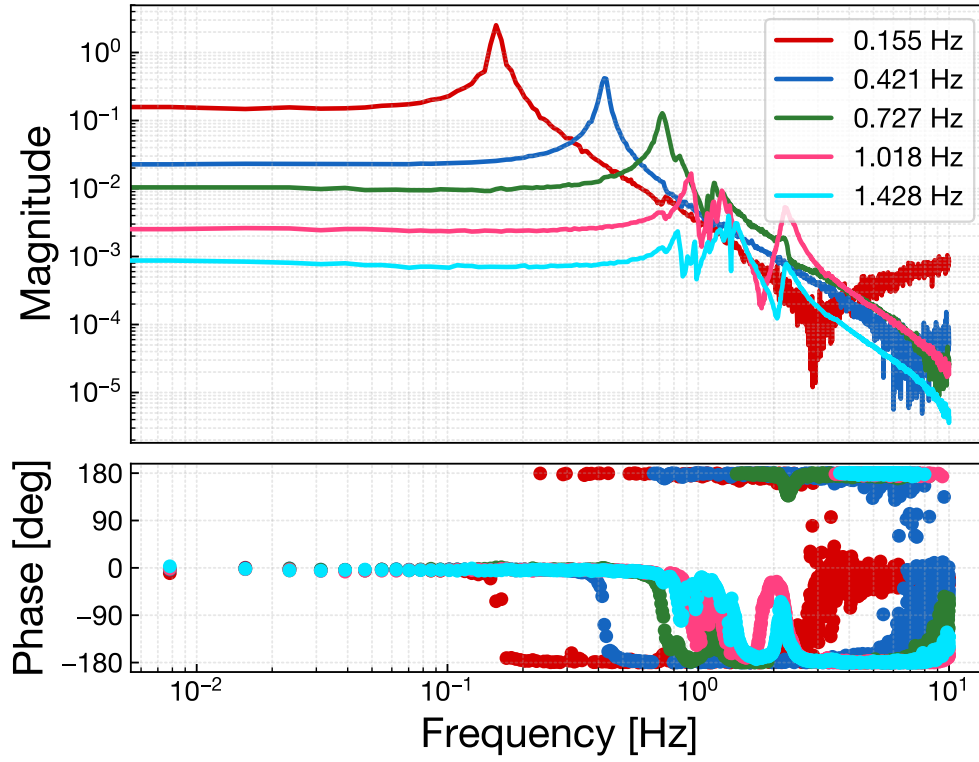
Fig. 5.16. Diagonal transfer functions in the modal coordinate for the GAS vertical modes.

amount of deviations from the real system, the modal decomposition can work on the lower order eigenmodes with the help of diagonalization of the sensing and driving matrices. In the control design of the suspension, we often focus on the lower-frequency mechanical resonances which have a large impact on the fluctuation of the suspended optics. Therefore, in the cases where the higher order modes are of less importance for the damping control, a model as inaccurate as that used in this experiment can achieve a sufficient modal decomposition.

5.4.3 Damping with modal controllers

We applied the modal damping scheme to the 1st and 2nd mode of the GAS chain, which are not only decoupled well with the diagonalized matrices but also need to be damped as they have large peaks in their natural states. The controllers of modal damping are the simple SISO filters engaged on the decoupled modal displacement signals. As simulated in section 4.4, the simplified system responses allowed us to easily design damping filters that are shown in fig. 5.18. The controller has one zero at the 0 Hz and several poles above 1 Hz, resulting in a feedback force that is proportional to the modal velocity at the resonant peak and that cuts off the high frequency signals. Initially, the gains of the control are set so that the peak in the open-loop gain overlaps that in the modal response to realize an almost critical damping. However, through a few times test of engaging the loop, it seemed
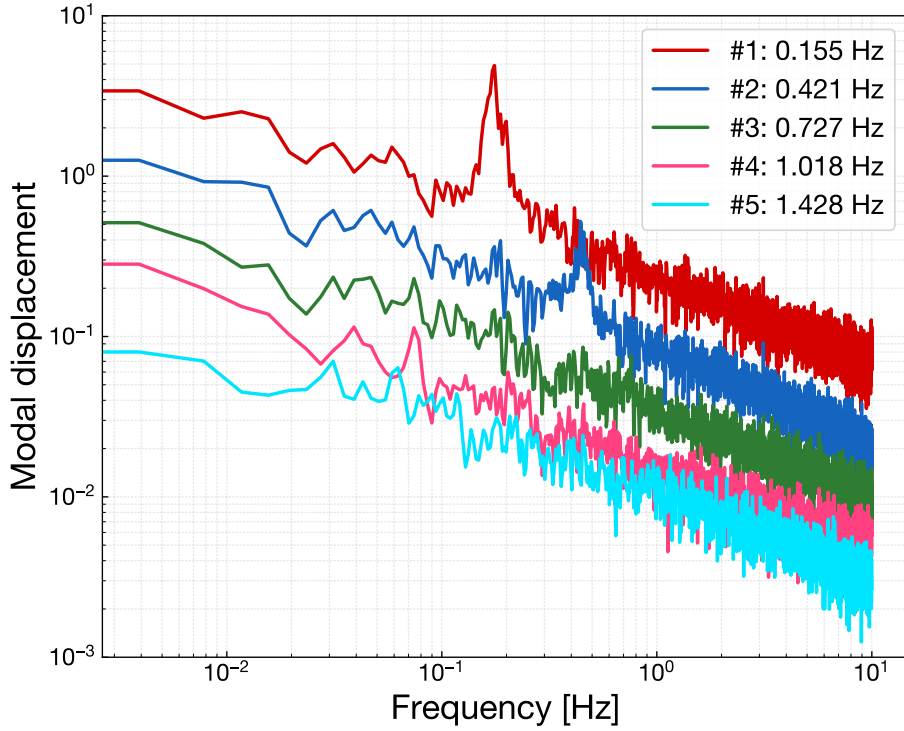
Fig. 5.17. Amplitude spectral density of the vertical motions of the Type-A tower in modal coordinates in a stationary state.

the initial gain leads to an overdamping condition and thus we adjusted the loop gain to be reduced to the plotted ones in fig. 5.18. Finally, the unity-gain frequencies are 0.22 Hz for the 1st modal loop and 0.49 Hz for the 2nd loop, while their corresponding phase margins are 63.3° and 32.8°, respectively.

The result of closing these modal loops can be seen as a spectrum in fig. 5.19. The peaks in a natural state are successfully supressed to a comparable level with the contribution of the sensor noise. However, instead, some peaks at around 1 Hz appeared in the spectrum of the higher order modes that cannot be seen in a stationary state, as shown in fig. 5.17. This indicates that the modal control for the lower order modes contaminated the state of the higher order modes that are not controlled. Incomplete modal decomposition may cause couplings between the different modes and thus introduce excess of vibration in an uncontrolled mode.

To evaluate the performance of modal damping, the spectra of the GAS stages and the DP with/without modal control for the 1st and 2nd vertical modes are shown in fig. 5.20. The peaks at 0.155 Hz and 0.421 Hz disappeared by the damping control in all the panels in fig. 5.20. Then, in fact, the resonant peaks of the higher order modes are excited in exchange for the suppression of the lower order modes' oscillation, that can be seen significantly in the spectrum of the F3 GAS. However, the RMS amplitudes are certainly suppressed because of
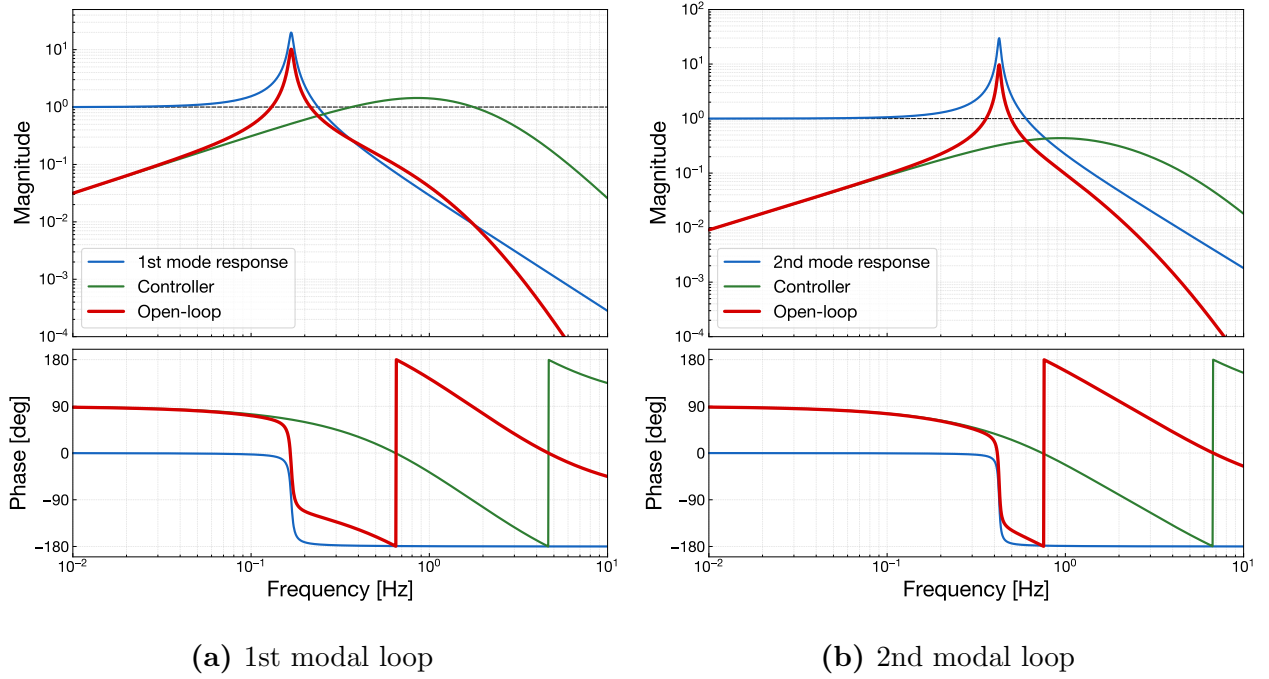
(a) 1st modal loop

(b) 2nd modal loop

Fig. 5.18. Open-loop transfer functions of the modal damping control for the GAS vertical modes.

the absence of the 1st and 2nd modes owing to the modal damping. The result of the RMS amplitude with the modal damping at the DP is 0.11 μm, whereas that without the control is 0.26 μm. Thus, the modal damping successfully reduced the RMS residual motion of the Type-A tower in the vertical direction.

Another side effect of the modal damping is sensor noise transmission at high frequencies. The spectrum of the DP above 0.6 Hz seems to be dominated by the sensor noise from the BF GAS LVDT because the spectrum shows proportionality of about f^{-2}, that indicates one stage mechanical isolation. As the modal control scheme in this test utilizes vertical actuators in all the GAS stages, the sensor noise is not filtered enough by the mechanical isolation even at the lowest stage. The sensor noise transmission due to modal control can be mitigated by using limited actuators in the upper stages which less affect the payload owing to the chain of mechanical filters.

There are still some points that were not tested in this experiment. One is confirmation of the decay time reduction. As predicted in section 4.4, the controller design of the modal damping should have an advantage of easily achieving almost critical damping. This attribute can be confirmed by comparing the exponential decay time between the stage-based control and the modal control. This measurement could not be performed in the limited period of the Type-A tower test. Moreover, the impact of sensor noise transmission can be optimized by weighting the use of actuators. One can make all the actuators participate in the modal
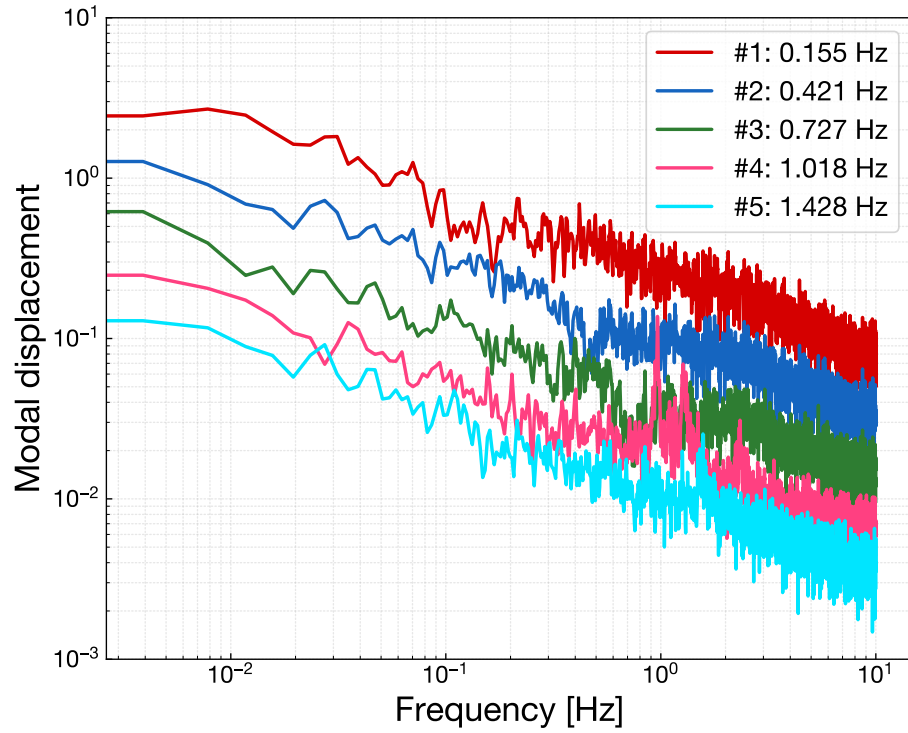
Fig. 5.19. Amplitude spectral density of the vertical motions of the Type-A tower in modal coordinate when modal control loops for the 1st and 2nd modes are closed.

damping to achieve maximum damping and also use a limited number of actuators to reduce noise contamination. Therefore, although the basic effectiveness of the modal damping control was validated, its application to the entire suspension control requires further experiments and verifications.

(a) F0 GAS

(b) F1 GAS

(c) F2 GAS

(d) F3 GAS
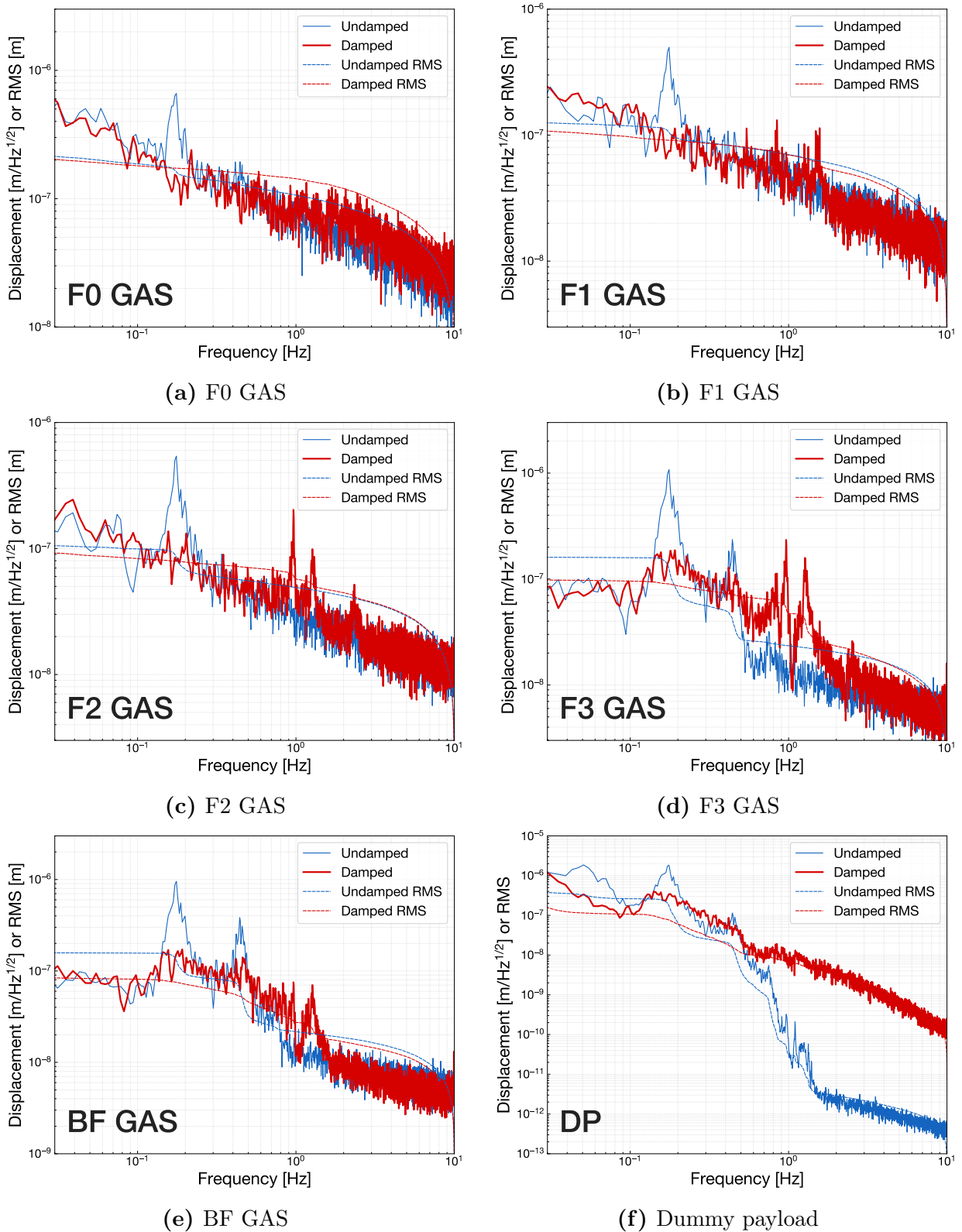
(e) BF GAS

(f) Dummy payload

Fig. 5.20. Amplitude spectral densities of the GAS stages and the DP. The red curves show the residual motions when modal damping for the 1st and 2nd vertical modes is engaged, that are compared with the blue curves representing those without damping control.

5.5   Vibration isolation ratio measurement

A measurement of the vibration isolation ratio of the Type-A suspension was performed in a test run of KAGRA. As the attenuation performance of the Type-A suspension nominally reaches $\sim 10^{-21}$ at 10 Hz, there is little hope that the vibration isolation performance can be measured directly owing to the poorer noise limitations of the local sensors. At the time of writing this thesis, KAGRA was undergoing upgrades in which fully-equipped apparatuses are installed and tested to achieve the baseline sensitivity.

The KAGRA test run was held in the configuration of simplified 3-km Michelson interferometer with no arm cavities nor recycling cavities, as illustrated in Fig. The two end mirrors were suspended with the Type-A suspension: one was at room temperature and the other was cooled down to a cryogenic temperature. Similarly, the optics in the center area were also suspended with their dedicated suspensions. The differential length of the Michelson interferometer was controlled by using the light reflected at the Faraday isolator. The signals of this reflected power were fed back to the TM and IM of the beam splitter (BS) with the crossover frequency of ~ 0.1 Hz and the overall unity gain frequency of ~ 50 Hz. For alignment control, the ETMY mirror was stabilized by local feedback with an optical lever, while the ETMX mirror was controlled with global feedback so that the reflected light from the ETMX follows that from the ETMY projected on the BS.

The strain sensitivity of the interferometer during the engineering run is shown in fig. 5.21. Through the noise study, we found that the sensitivity was limited by angular control noise below 50 Hz and by the dark noise of the photodiodes receiving the error signal for the Michelson interferometer length control. Further discussions about the interferometer sensitivity and stability can be found in [41].

The method used to obtain the vibration isolation ratio was a combination of direct transfer function measurements and an estimation with the tuned suspension model. We resolved the vibration isolation ratio into two factors: the transfer function from the ground to the top stage and that from the top stage to the mirror at the bottom. The first transmission factor was identified by measuring transfer functions from the force exerted on the IP stage to the displacement of the longitudinal sensors at the IP and the BF. The measured transfer functions, which are shown in fig. 5.22, were properly matched with the model predictions derived from the 3D rigid-body model of the full Type-A suspension. Owing to limited actuation power, the measurement to the BF got deviated at frequencies above 1.5 Hz. Nevertheless, we can see a great consistency between the measurement and the model even in the peak distribution over the frequencies, although a tiny offset of the peak frequency for some higher order modes can be recognized.

Based on the consistency between the characteristics of the real system and the model predictions, we assumed that the model could generate a confident estimation of the vibration
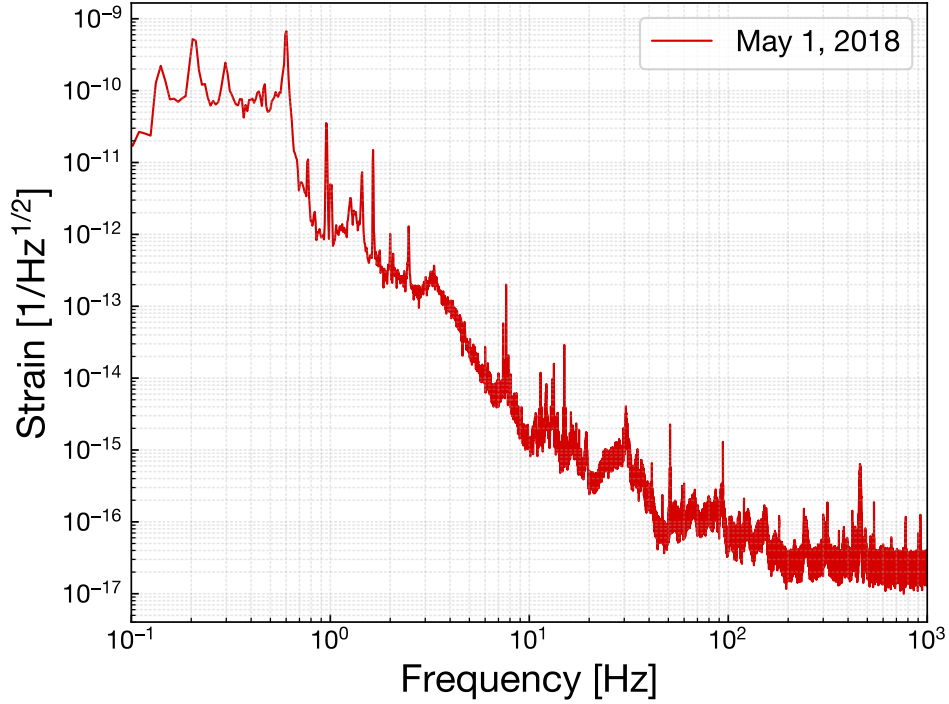
Fig. 5.21. Calibrated strain sensitivity of the KAGRA in the first engineering run.

isolation ratio for the installed Type-A suspension. Thus, as it is difficult to measure the transfer function from the seismic displacement to the IP stage, we derived it from the model with sufficient confidence, which is shown in fig. 5.23.

The vibration transmission from the IP stage to the test mass was measured by sending a monochromatic sinusoidal injection to the IP and then monitoring the error signal of the Michelson interferometer length control. The sampled frequency of the excitation is chosen so as not to excite the mechanical resonance of the Type-A suspension as a large disturbance may break the lock of the interferometer. Although the error signal of the Michelson interferometer can include the information about the other end mirror or the BS, the output is correlated with the excited IP displacement, which is confirmed by measuring the coherence of the local sensor of the IP and the interferometer output.

Finally, the vibration isolation ratio of the Type-A suspension was estimated by combining the derived model and the measured vibration transmission, which is shown in fig. 5.24. Despite the careful selection of the excitation frequency and amplitude, the extreme attenuation performance of the Type-A suspension did not allow us to measure the well-correlated transfer function above 1.8 Hz. In addition, the calibration procedure was guaranteed for frequencies as low as ~ 0.5 Hz owing to the response of the BS payload where the error signal of the Michelson interferometer was fed back. For these reasons, only the frequency points in the 0.8–1.7 Hz range could be measured with a coherence of more than 0.6.
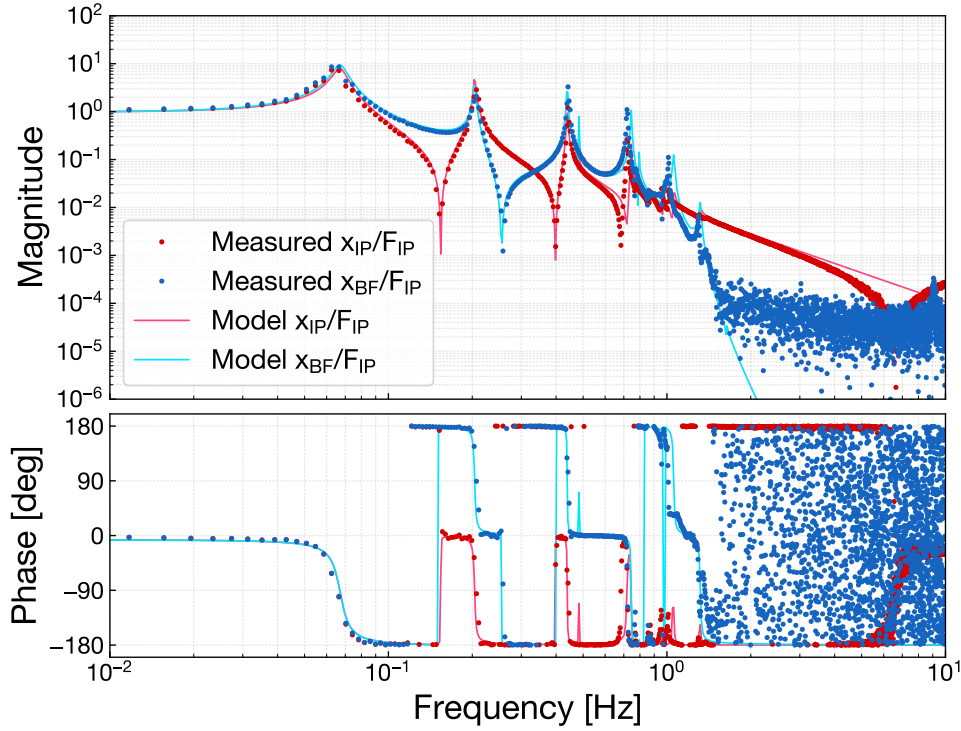
Fig. 5.22. Transfer functions of the full Type-A suspension from the force on the IP to the local sensor at the IP and BF in the longitudinal direction of the full Type-A suspension.

The total tendency of the vibration isolation ratio appeared as expected. However, although the measured transfer functions were sufficiently matched with the model in fig. 5.22, the vibration isolation ratio exhibited deviations from the model at the frequencies below 1.4 Hz in fig. 5.24. The zoomed in subfigure in fig. 5.24 shows that the maximum difference between the measurement and the model is at most an order of magnitude at 1.065 Hz. These discrepancies may be due to the inaccurate modeling of the cryogenic payload. The resonant peaks around 1 Hz will originate from the internal modes of the payload, such as the pure longitudinal modes and coupled pitch modes, which have resonances in this frequency region. Although characterization of the payload was beyond the scope of this study, an improvement in the model based on the transfer function measurements in the DoFs of the payload can resolve the observed mismatches. Another possible cause of the mismatch is the error in the calibration procedure of the Michelson interferometer. The calibration assumed a simple f^{-2}-response in the actuator including the BS response, whereas it is known that the BS has a resonant peak at 0.5 Hz in its longitudinal response. It can contribute to the deviation of the measured vibration isolation ratio from the model prediction at low frequencies.

The mismatches mentioned above notwithstanding, the model has a reasonable consistency with the real system of the Type-A suspension. Thus, by extrapolating the estimated
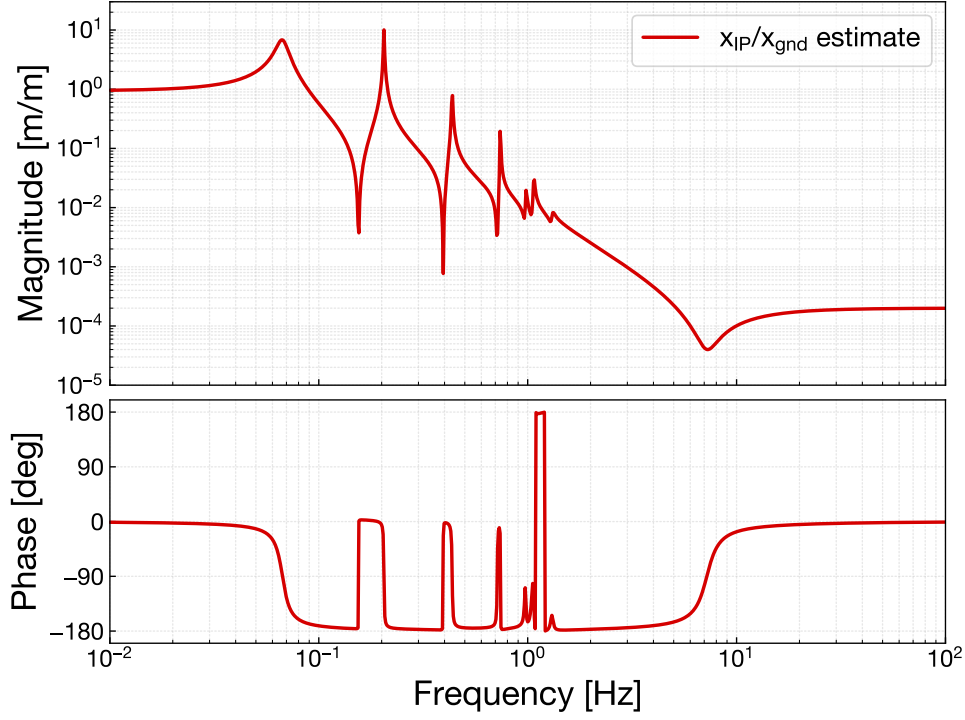
Fig. 5.23. Estimated vibration isolation ratio from the ground to the IP stage.

vibration isolation ratio to the high frequencies, we can obtain an indication of the vibration isolation performance of the constructed Type-A suspension. Taking the saturation effect of the IP into account, the seismic attenuation factor of the Type-A suspension at 10 Hz is estimated as 9×10^{-22} and is plotted as a blue curve in fig. 5.24. Assuming the seismic noise model of the KHNM is applicable, the requirement of the vibration isolation ratio corresponding to the required longitudinal displacement noise can be also derived. Comparing the estimated vibration isolation ratio to the requirement of 5×10^{-9} at 10 Hz, the Type-A suspension possesses sufficient capability to attenuate the seismic noise coupling in the pure longitudinal direction.

It would be seen that the Type-A suspension with the estimated performance is over engineered against the requirement. Although this attenuation performance in the longitudinal direction is the result of a number of stages that cascade from the top, this design aims to secure the vibration isolation in the vertical direction. The five stages of the GAS filter chain are a reasonable design for reducing the displacement noise through vertical-to-longitudinal coupling. Thus, it is necessary to confirm the vibration isolation performance in the vertical direction, which we put off as a subject of forthcoming tests.

In the future, the direct measurement of the in-band seismic attenuation performance using the interferometer with arm cavities will be explored. It can be argued that the measurement reported in this section goes no further than the in-band vibration isolation ratio

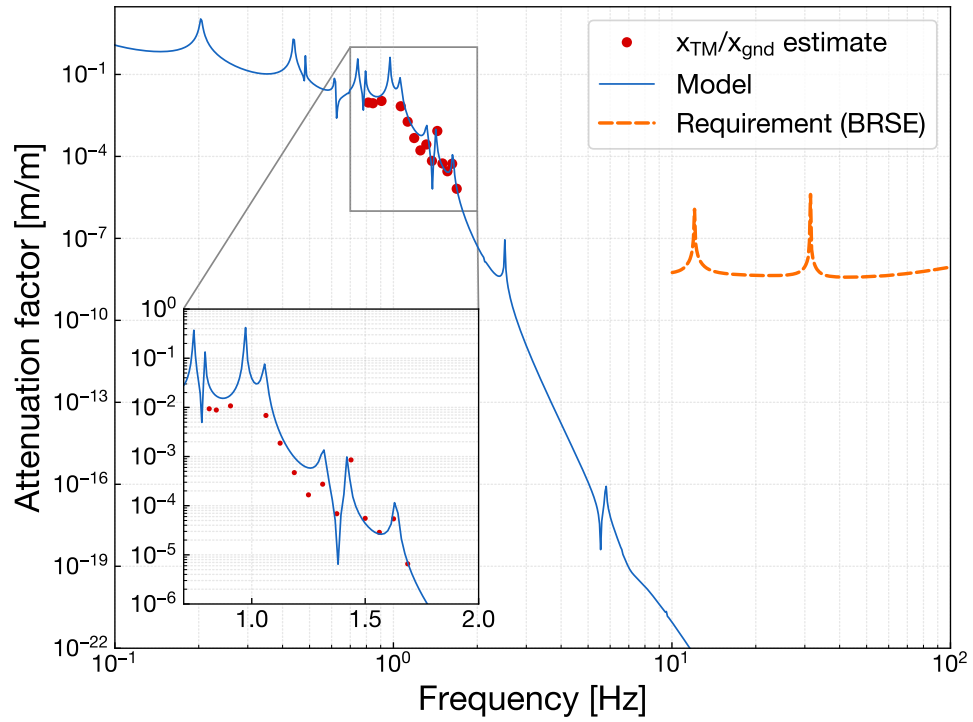**Fig. 5.24.** Estimated vibration isolation ratio from the ground to the mirror (TM).

with the model estimation as the measured data covers only a limited frequency region. It can be overcome by using the cavity-implemented interferometer with an outstanding sensitivity. In addition, unlike in this experiment, the performance should be tested with the payload in a cryogenic environment, which is the actual operational condition.

Chapter 6

Conclusion

In this study, we developed a Type-A suspension, a vibration isolation system for the test masses in KAGRA. We have constructed a so-called Type-A tower, which is the key part for vibration isolation. Through the experiments summarized below, we concluded that the installed Type-A tower can provide sufficient seismic attenuation and control performance in order to achieve the design sensitivity of the KAGRA interferometer. There is still a need to test the Type-A suspension after integration with the cryogenic payload. Through commissioning of the global system in many aspects, this study has contributed to making gravitational wave observation possible with KAGRA.

System characterization

The system characterization validated that the installed Type-A tower system basically has the designed dynamic characteristics that satisfy the requirements for gravitational wave observation. The frequency responses of the Type-A tower were measured and compared to the predictions of the nominal model. Although there is some amount of deviation, the obtained frequency responses can be regarded as acceptable to achieve the required vibration isolation performances except in the vertical direction. As for the vertical direction, the dynamics of the Type-A tower show discrepancies between the measurement results and the model predictions, particularly in the mode shapes of its higher order resonances. It is suspected that the higher order oscillatory behavior has stronger dependence on the divergence of the mechanical parameters from the nominal values. However, as the higher order modes have a smaller impact on the RMS residual motion and the measured mode frequencies are roughly distributed as expected, the discrepancies in the vertical mode dynamics seem to be within the permissible range. This tolerance is also plausible from the measured displacement spectrum at the dummy payload, which is suspended, instead of the actual cryogenic payload. One problem that still remains is the effect of couplings from non-straightforwardly-controllable degrees of freedom, such as a tilt of the middle GAS filter stages. The impact

of the couplings on the test mass or the interferometer should be confirmed after integration with the cryogenic payload.

Torsion mode damping

Torsion mode damping of the Type-A tower is tested. As a major fraction of the height of the Type-A suspension is accounted for a series of single suspension wires, the system behaves like a torsion pendulum with extremely low stiffness and a long duration of the torsional modes, which makes stabilizing the alignment of the mirror an issue. The Type-A tower is responsible for addressing this issue by providing a function of active damping control at the tower's bottom stage. The torsion mode damping test proves that the long exponential decay time of the resonances can be successfully reduced to less than 1 min by active feedback control. In addition, the in-loop sensor indicates that the RMS residual angular fluctuation in torsion is suppressed sufficiently to a level required to acquire arm cavity lock. Therefore, it is concluded that the Type-A tower has satisfactory torsion mode damping.

Implementation of modal damping

This study presented an advanced control scheme called modal damping. Modal damping processes feedback signals in a decoupled modal basis instead of a conventional Cartesian basis, allowing us to simplify the servo design optimization and to access efficient actuation for a coupled oscillatory system. The control test demonstrates feasibility of modal damping for the coupled vertical modes of the Type-A suspension. By deriving a conversion law between the Cartesian basis and the modal basis from the mathematical model, coupled signals of the vertical modes can be decomposed into those of each orthogonal eigenmode. Moreover, the result of the modal damping shows that the eigenmodes can be damped independently of other modes. Although the availability of modal controllers is validated only for the vertical modes in this test, one can expect to apply this technique to other stages having less-powerful actuators such as the cryogenic payload.

Measurement of vibration isolation ratio

The installed Type-A tower was integrated with the cryogenic payload and incorporated into the global system of the KAGRA interferometer. This thesis includes the measurement of the vibration isolation ratio from the ground to the test mass. During the first cryogenic test operation of the simplified 3-km Michelson interferometer, we measured the vibration transmissivity from the top stage to the error signals of the inteferometer output. Combining the measured result with a model prediction of the transmissibity from the ground to the top stage derived from the tuned mathematical model, the total vibration isolation ratio of the Type-A suspension was estimated as 9×10^{-22} for the pure longitudinal contribution at 10

Hz. Although the estimated result contains some amount of mismatch with respect to the nominal model prediction, the seismic attenuation performance of the real system seems to be a reasonable enough to achieve the design sensitivity of KAGRA.

Achievement of the requirements

Table 6.1 summarizes the achievement of requirements by the Type-A suspension. Here the measures evaluated in the performance test of the Type-A tower are only listed. Among the DoFs of interest, the setup of the Type-A tower cannot yield meaningful performance results in pitch direction as it strongly depends on the multi-wired suspension structure inside the cryogenic payload. In addition, the requirements in the observation phase have to be out of the scope in this experiments owing to similar reasons.

The requirements in the calm-down phase have been satisfied as far as the tower test can permit except for the 1/e modal decay time. Owing to the number of eigenmodes the Type-A suspension has and the limitation of the experimental period, the decay time measurement of only the lowest-order eigenmodes is completed. However, the eigenmodes measured in this experiment are the most important ones in terms of the interferometer operation. Although other principal eigenmodes are not evaluated in the measurement, the control simulation presented in chap. 4 predicted that they can be damped sufficiently to achieve a decay time less than 1 min. The RMS amplitudes required for the calm-down phase are successfully satisfied in the tower stages. Therefore, it is expected that the mirror in the cryogenic payload suspended from the constructed tower can achieve a reasonable magnitude.

The performances required in the lock-acquisition phase were measured and showed sufficiently small RMS values. Note that the ongoing commissioning of the KAGRA interferometer after these experiments has actually succeeded to lock the arm cavity using the installed Type-A suspension.

Table 6.1. Experimental results of the performance test of the Type-A tower. Only the meausred items that can be used to evaluate whether requirements have been met are listed.

Calm-down phase			
Item	Measurement	Requirement	Notes
1/e modal decay time	< 44 sec.	< 60 sec.	Yaw 1st–3rd modes
RMS displacement (L)	$< 1.1 \ \mu$m	$< 50 \ \mu$m	Measured at BF
RMS displacement (T)	$< 1.4 \ \mu$m	$< 100 \ \mu$m	Measured at BF
RMS displacement (V)	$< 0.11 \ \mu$m	$< 100 \ \mu$m	Measured at DP
RMS angle (Y)	$\sim 0.23 \ \mu$rad	$< 50 \ \mu$rad	In-loop evaluation at BF
Lock-acquisition phase			
Item	Measurement	Requirement	Notes
RMS velocity (L)	$< 0.73 \mu$m/s	$< 240 \ \mu$m/s	Measured at BF
RMS angle (Y)	$\sim 0.23 \ \mu$rad	$< 0.88 \ \mu$rad	In-loop evaluation at BF

Bibliography

[1] A. Einstein, *Sitzungsberichte der Königlich Preußischen Akademie der Wissenschaften (Berlin)*, **1**, pp. 688–696, (1916). "Näherungsweise Integration der Feldgleichungen der Gravitation", (cited on p. 13).

[2] A. Einstein, *Sitzungsberichte der Königlich Preußischen Akademie der Wissenschaften (Berlin)*, **1**, pp. 154–167, (1918). "Über Gravitationswellen", (cited on p. 13).

[3] B. P. Abbott et al., *Phys. Rev. Lett.* **116** (6), pp. 1–16, (2016). "Observation of gravitational waves from a binary black hole merger", (cited on p. 18).

[4] B. P. Abbott et al., *Astrophys. J.* **818** (2), p. L22, (2016). "Astrophysical implications of the binary black hole merger GW150914", (cited on p. 18).

[5] B. P. Abbott et al., *Phys. Rev. Lett.* **119**, p. 141101, (2017). "GW170814 : A three-detector observation of gravitational waves from a binary black hole coalescence", (cited on p. 19).

[6] B. P. Abbott et al., *Phys. Rev. Lett.* **119** (16), p. 161101, (2017). "GW170817: Observation of Gravitational Waves from a Binary Neutron Star Inspiral", (cited on p. 19).

[7] URL: https://www.gw-openscience.org/catalog/ (cited on p. 19).

[8] R. A. Hulse and J. H. Taylor, *Astrophys. J.* **195** (1), pp. L51–L53, (1975). "Discovery of a Pulsar in a Binary System", (cited on p. 19).

[9] J. Weber, *Phys. Rev. Lett.* **20** (23), pp. 1307–1308, (1968). "Gravitational-wave-detector events", (cited on p. 24).

[10] R. L. Forward, *Phys. Rev. D,* **17** (2), pp. 379–390, (1978). "Wideband laser-interferometer graviational-radiation experiment", (cited on p. 24).

[11] A. A. Michelson and E. W. Morley, *Am. J. Phys.* **33**, pp. 333–336, (1887). "On the relative motion of the earth and the luminiferous Æther", (cited on p. 24).

[12] J. Peterson, *techreport*, **Open-file Report-**, (1993). "Observations and modeling of seismic background noise", (cited on pp. 35, 36).

[13] LCGT Collaboration, *KAGRA Internal Document*, **JGW-T0400030**, (2009). "LCGT Design Document ver.3", (cited on p. 37).

[14] A. Takamori, *PhD thesis*, University of Tokyo, (2002). "Low frequency seismic isolation for gravitational wave detectors", (cited on p. 45).

[15] M. Blom, *PhD thesis*, Vrije Universiteit, (2015). "Seismic attenuation for Advanced Virgo Vibration isolation for the external injection bench", (cited on p. 45).

[16] A. Bertolini et al., *Nucl. Instrum. Methods Phys. Res. A*, **435** (3), pp. 475–483, (1999). "Seismic noise filters, vertical resonance frequency reduction with geometric anti-springs: A feasibility study", (cited on p. 48).

[17] G. Cella et al., *Nucl. Instrum. Methods Phys. Res. A*, **540** (2-3), pp. 502–519, (2005). "Monolithic geometric anti-spring blades", (cited on p. 48).

[18] A. Stochino et al., *Nucl. Instrum. Methods Phys. Res. A*, **580** (3), pp. 1559–1564, (2007). "Improvement of the seismic noise attenuation performance of the Monolithic Geometric Anti-Spring filters for gravitational wave interferometric detectors", (cited on p. 50).

[19] T. Sekiguchi, *PhD thesis*, University of Tokyo, (2016). "A Study of Low Frequency Vibration Isolation System for Large Scale Gravitational Wave Detectors", (cited on pp. 51).

[20] H. A. Sodano et al., *J. Vib. Acoust.* **128** (3), pp. 294–302, (2006). "Improved Concept and Model of Eddy Current Damper", (cited on p. 54).

[21] F. Matichard et al., *Class. Quantum Grav.* **32** (18), (2015). "Seismic isolation of Advanced LIGO: Review of strategy, instrumentation and performance", (cited on p. 56).

[22] Y. Aso et al., *Phys. Rev. D*, **88** (4), p. 043007, (2013). "Interferometer design of the KAGRA gravitational wave detector", (cited on p. 58).

[23] T. Akutsu et al., *Prog. Theor. Exp. Phys.* **2018** (1), pp. 1–23, (2018). "Construction of KAGRA: an underground gravitational-wave observatory", (cited on p. 59).

[24] T. Sekiguchi, *KAGRA Internal Document*, **JGW-T1402971**, (2014). "Seismic Spectrum in Kamioka Mine", (cited on p. 59).

[25] M. G. Beker, *PhD thesis*, Vrije Universiteit Amsterdam, (2013). "Low-frequency sensivity of next generation gravitational wave detectors", (cited on p. 59).

[26] ET Science Team. "Einstein gravitational wave Telescope Conceptual Design Study". (2011). URL: https://tds.virgo-gw.eu/?content=3%7B%5C&%7Dr=8709 (cited on p. 60).

[27] A. Nishizawa, *KAGRA Internal Document*, **JGW-T1706440**, (2017). "Water Newtonian noise for KAGRA", (cited on p. 61).

[28] E. D. Black, *Am. J. Phys.* **69** (1), pp. 79–87, (2001). "An introduction to Pound–Drever–Hall laser frequency stabilization", (cited on p. 71).

[29] A. J. Mullavey et al., *Optics Express,* **20** (1), p. 81, (2012). "Arm-length stabilisation for interferometric gravitational-wave detectors using frequency-doubled auxiliary lasers", (cited on p. 72).

[30] K. Izumi, *Master's Thesis*, University of Tokyo, (2009). "レーザー干渉計型重力波検出器のための Fabry-Perot 共振器の共振引き込み研究", (cited on p. 72).

[31] Y. Enomoto, Y. Michimura, and K. Izumi, *KAGRA Internal Document*, **JGW-T1808343**, (2018). "Definitions for the X arm commissioning", (cited on p. 72).

[32] Y. Obuchi, *KAGRA Internal Document*, **JGW-T1706280**, (2017). "Maraging-wire Structural Analysis Report Final Design", (cited on p. 82).

[33] H. Tariq et al., *Nucl. Instrum. Methods Phys. Res. A*, **489** (1-3), pp. 570–576, (2002). "The linear variable differential transformer (LVDT) position sensor for gravitational wave interferometer low-frequency controls", (cited on p. 87).

[34] C. Wang et al., *Nucl. Instrum. Methods Phys. Res. A*, **489** (1-3), pp. 563–569, (2002). "Constant force actuator for gravitational wave detector's seismic attenuation systems (SAS)", (cited on p. 90).

[35] Y. Michimura et al., *Class. Quantum Grav.* **34** (October), p. 225001, (2017). "Mirror actuation design for the interferometer control of the KAGRA gravitational wave telescope", (cited on p. 91).

[36] M. Barton, *LIGO Internal Document*, **LIGO-T020205**, (2014). "Models of the Advanced LIGO Suspensions in Mathematica", (cited on p. 93).

[37] T. Sekiguchi, *KAGRA Internal Document*, **JGW-T1503729**, (2015). "Suspension rigid-body modeling tool in Mathematica", (cited on p. 93).

[38] F. Acernese et al., *Astroparticle Physics*, **20** (6), pp. 617–628, (2004). "A local control system for the test masses of the Virgo gravitational wave detector", (cited on p. 96).

[39] L. Ruet, *PhD thesis*, Institut National des Sciences Appliques de Lyon, (2007). "Active Control and Sensor Noise Filtering Duality Application to Advanced LIGO Suspensions", (cited on p. 99).

[40] B. N. Shapiro, *PhD thesis*, Massachusetts Institute of Technology, (2012). "Adaptive Modal Damping for Advanced LIGO Suspensions", (cited on p. 99).

[41] T. Akutsu et al., (2019). "First cryogenic test operation of underground km-scale gravitational-wave observatory KAGRA", (cited on p. 138).